Controllable Hydrogel Adhesion through Mechanics of Contraction and Physics of Polymer Entanglement

Zhen Yang

Department of Mechanical Engineering
McGill University, Montreal

August 15, 2023

A thesis submitted to McGill University in partial fulfillment of the requirements of the degree of Doctor of Philosophy

Abstract

The interfacial bonding between materials is governed by a balance between the energy release rate and the adhesion energy. These two factors quantify the driving force for delamination and the adhesive capacity, respectively. In the realm of biological organisms, examples such as blood clots and cells exhibit a remarkable ability to manipulate both these variables when interacting with various substrates. Specifically, the active contraction of these organisms generates residual stress at the interface, leading to an intrinsic energy release rate that opposes adhesion. Furthermore, the presence of slip bonds—non-covalent protein-protein interactions at the organism-substrate interfaces—contributes to dynamic adhesion energy due to thermally-activated bond breaking mechanisms. This exceptional capability allows biological organisms to alternate between bonding and debonding states. Leveraging these extraordinary aspects of adhesion modulation presents a promising avenue to next generation soft adhesives with tunable adhesion properties.

A prime candidate for such innovation is hydrogel-based adhesives. These materials are known for their high water content, softness, compatibility with drugs and chemicals, and suitability for applications like tissue adhesives, wound dressings, and drug delivery systems. However, existing hydrogel adhesives are often limited by their static adhesion properties, wherein the adhesion remains fixed after application. While incorporating chemical modifications at the interface has been extensively explored to modulate adhesion, the outcomes can be compromised by uncontrolled chemical interactions across the interface and the ensuing complications concerning biocompatibility, posing significant hurdles for practical implementation.

To pave ways for innovative methodologies in modulating hydrogel adhesion across a broad spectrum, without the need for alterations in either bulk or interface chemistry, this thesis draws inspiration from the active contraction and dynamic adhesion observed in biological organisms. Both of these mechanisms can be seamlessly integrated into hydrogels themselves during the manufacturing stage, achieved through strategic selection of the hydrogel matrix functionality or design of the interfacial network topology. In the first approach,

the hydrogel matrix using a stimuli-responsive polymer network was made to harness their active contraction to induce an intrinsic energy release rate, leading to spontaneous adhesion modulation. This energy release rate effectively counterbalances adhesion energies within a comparable range, thereby reducing the external force required for delamination. However, when the adhesion energy significantly exceeds the intrinsic energy release rate, the impact of the active bulk contraction diminishes. In such scenarios, this thesis transitions to the second approach, wherein the adhesion energy was directly manipulated by designing the interfacial polymer network topology of the hydrogel adhesive. This manipulation gives rise to interfacial polymer entanglements with distinct topologies, each displaying programmable adhesion behaviors. This thesis further discusses the underlying physics governing these emergent programmable adhesion behaviors and leverage this understanding to craft hydrogel adhesives with predictive adhesion energy, controllable adhesion kinetics, and customizable spatial distributions. Moreover, these concepts are applied to the creation of soft devices endowed with unprecedented functionalities.

Abrégé

L'adhérence interfaciale entre les matériaux est régie par un équilibre entre le taux de libération d'énergie et l'énergie d'adhérence. Ces deux facteurs quantifient la force motrice du délaminage et la capacité d'adhésion, respectivement. Dans le domaine des organismes biologiques, des exemples tels que les caillots sanguins et les cellules présentent une capacité remarquable à manipuler ces deux variables lorsqu'ils interagissent avec divers substrats. Plus précisément, la contraction active de ces organismes génère des contraintes résiduelles à l'interface, conduisant à un taux intrinsèque de libération d'énergie qui s'oppose à l'adhérence. De plus, la présence de liaisons de glissement - des interactions protéine-protéine non covalentes aux interfaces organisme-substrat - contribue à l'énergie d'adhérence dynamique en raison de mécanismes de rupture de liaison activés thermiquement. Cette capacité exceptionnelle permet aux organismes biologiques d'alterner entre des états de liaison et de déliaison. Exploiter ces aspects extraordinaires de la modulation de l'adhérence présente une avenue prometteuse pour les adhésifs souples de nouvelle génération aux propriétés d'adhérence ajustables.

Un candidat de choix pour une telle innovation est représenté par les adhésifs à base d'hydrogel. Ces matériaux sont connus pour leur teneur élevée en eau, leur douceur, leur compatibilité avec les médicaments et les produits chimiques, ainsi que leur adaptabilité à des applications telles que les adhésifs tissulaires, les pansements et les systèmes de libération de médicaments. Cependant, les adhésifs à base d'hydrogel existants sont souvent limités par leurs propriétés d'adhérence statiques, où l'adhérence reste fixe après application. Bien que l'incorporation de modifications chimiques à l'interface ait été largement explorée pour moduler l'adhérence, les résultats peuvent être compromis par des interactions chimiques incontrôlées à travers l'interface et les complications subséquentes concernant la biocompatibilité, posant d'importants obstacles à une mise en œuvre pratique.

Pour ouvrir la voie à des méthodologies innovantes pour moduler l'adhérence des hydrogels sur un large spectre, sans nécessiter de modifications soit dans la chimie en vrac, soit dans celle de l'interface, cette thèse puise son inspiration dans la contraction active et l'adhérence dynamique observées dans les organismes biologiques. Ces deux mécanismes peuvent être

intégrés de manière transparente dans les hydrogels eux-mêmes lors de la phase de fabrication, en utilisant une sélection stratégique de la fonctionnalité de la matrice d'hydrogel ou la conception de la topologie du réseau interfacial. Dans la première approche, la matrice d'hydrogel utilisant un réseau polymère sensible aux stimuli a été conçue pour exploiter leur contraction active afin d'induire un taux intrinsèque de libération d'énergie, conduisant à une modulation d'adhérence spontanée. Ce taux de libération d'énergie équilibre efficacement les énergies d'adhérence dans une plage comparable, réduisant ainsi la force externe requise pour le délaminage. Cependant, lorsque l'énergie d'adhérence dépasse considérablement le taux intrinsèque de libération d'énergie, l'impact de la contraction active en vrac diminue. Dans de tels scénarios, cette thèse passe à la deuxième approche, où l'énergie d'adhérence était directement manipulée en concevant la topologie du réseau polymère interfacial de l'adhésif à base d'hydrogel. Cette manipulation donne naissance à des enchevêtrements polymères interfaciaux avec des topologies distinctes, chacune affichant des comportements d'adhérence programmables. Cette thèse discute en outre la physique sous-jacente régissant ces comportements d'adhérence programmables émergents et exploite cette compréhension pour créer des adhésifs à base d'hydrogel avec une énergie d'adhérence prédictive, une cinétique d'adhérence contrôlable et des distributions spatiales personnalisables. De plus, ces concepts sont appliqués à la création de dispositifs souples dotés de fonctionnalités sans précédent.

Acknowledgements

I am thankful to the numerous individuals who have provided assistance and support throughout my doctoral journey at McGill University, ultimately leading to the completion of this dissertation.

I am deeply grateful to my advisor, Prof. Jianyu Li, whose unwavering inspiration, patience, and guidance have played a pivotal role in shaping my research pursuits. His unique interdisciplinary problem-solving approach and constant encouragement to foster collaborations across diverse fields have significantly shaped the trajectory of this thesis. I must also express my appreciation to my co-advisor, Prof. Rong Long, for his consistent support and encouragement throughout my academic voyage. His profound insights into mechanics have greatly enhanced my comprehension and learning. I would also like to express my gratitude to Prof. Luc Mongeau, who generously provided access to his lab equipment, enabling me to conduct my research effectively.

I would like to extend my gratitude to all my collaborators who have been instrumental in the progression of this research. Among them, I must particularly acknowledge Xingwei Yang in Prof Rong Long's lab at CU boulder, whose unwavering commitment, intelligence, and eagerness to contribute have been invaluable assets throughout my PhD journey. Our consistent and fruitful collaboration, starting from day one, has been a guiding force in many of the essential projects undertaken during this program. To all the lab mates in Prof Jianyu Li's lab at McGill, Zhenwei Ma, Guangyu Bao, Shuaibing Jiang, Ran Huo, Xiang Ni, and many more, I am indebted to each of you for your collective contributions that have translated my ideas into reality.

I would like to extend my deepest gratitude to my family Minyue Pu, Yudong Yang, Guorong Pu, and Heying Ding, for their unwavering support throughout my academic journey. Their constant encouragement, both mentally and financially, has been instrumental in my pursuit of higher education. Their belief in my abilities and the sacrifices they have made have played a pivotal role in shaping my success.

I am also grateful for the members of my thesis committee, Prof. Damiano Pasini and

Prof. Jun Song, whose invaluable insights, feedback, and expertise have greatly enriched the quality of this work. Finally, I extend my gratitude to the funding agencies, FRQNT (Fonds de Recherche du Québec Nature et technologies) and MEDA (McGill Enigneering Doctoral Award), for their invaluable support and financial assistance throughout my research journey.

Contents

Abstract ii
Abrégé iv
Acknowledgements v
List of Figures xi
List of Tables xii

1 Introduction **2**
1.1 Background 3
1.2 Topological hydrogel adhesive 4
1.3 Controllable adhesive 5
1.4 Dissertation Scope 7
1.5 Publications 10
1.6 Contribution of authors 12

2 Literature review **17**
2.1 Strategies in designing controllable hydrogel adhesives 18
2.1.1 Adhesion energy 18
2.1.2 Adhesion kinetics 19
2.2 Controllable hydrogel adhesives through stimuli-responsiveness and engineered network topology 21
2.2.1 Mechanically active soft adhesives 21
2.2.2 Slip-bond-based adhesion in biological organisms and synthetic interfaces 23
2.2.3 Topology of polymer entanglement 25
2.3 Griffith criterion for fracture propagation 26
2.4 Fracture and adhesion testing specimens for soft materials 27
2.4.1 Peeling 27
2.4.2 Modified Lap-shear 28
2.4.3 Pure-shear 29

2.5 Interface delamination of soft active materials 30
2.6 Nomenclature 38

3 Stimulation regulates adhesion and mechanics of adhesive hydrogels 45
3.1 Introduction 46
3.2 Theoretical section 49
3.2.1 Free energy function 49
3.2.2 Determination of the Flory Interaction Parameter 50
3.3 Experimental section 51
3.3.1 Adhesion Energy Measurement 51
3.3.2 Free Swelling Test 51
3.3.3 Fracture Energy Measurement 51
3.3.4 Rheological Measurements 52
3.4 Results and Discussion 52
3.4.1 Modulating Adhesion via Stimulation. 52
3.4.2 Modulating Mechanical Properties via Stimulation. 55
3.4.3 Analytical Estimation of the Energy Release Rate G. 56
3.4.4 Characterization of Stimuli-Responsive Behavior. 56
3.4.5 FE Simulation of the Stimuli-Responsive Hydrogel Adhesive. 59
3.4.6 Numerical Estimation of the Energy Release Rate G. 60
3.4.7 Rational Design of the Bonding of a Stimuli Responsive Hydrogel Adhesive. 60
3.4.8 Applicability of Our Results. 62
3.5 Conclusion 63
3.6 Nomenclature 64

Preamble to Chapter 4 81

4 Programming hydrogel adhesion with engineered network topology 81
4.1 Abstract 82
4.2 Introduction 82
4.3 Results and Discussion 85
4.3.1 Structural characterization 86
4.3.2 Interfaical topological linkages to program rate-dependent adhesion energy 88
4.3.3 Programming adhesion kinetics 91

4.3.4 Universal applicability 94
4.3.5 Programming spatial adhesion 96
4.3.6 TEA-based devices 99
4.4 Conclusion 100
4.5 Nomenclature 102

5 Discussion and future work **135**
5.1 Applicability of the strategies 136
5.2 Biodegradability and repeatability of hydrogel adhesion 138
5.3 Loading rate to release hydrogel adhesives 139
5.4 future work 139

6 Concluding remarks **141**

7 Original contribution to knowledge **143**

List of Figures

1.1 Qualitative illustrations showing energy release rate, adhesion energy, and adhesion kinetics. . . . 6
1.2 Data adapted from [29] showing the scaling law $F \sim \sqrt{\frac{A}{C}}$ . . . 8

2.1 Mechanically active materials. . . . 22
2.2 Schematics showing slip bonds and their characteristics. . . . 24
2.3 Schematics of different polymer entanglement topologies. . . . 25
2.4 Schematic of peeling test. . . . 28
2.5 Schematic of the modified lap-shear test. . . . 29
2.6 Schematics of pure shear test. . . . 30
2.7 Schematics of a bi-material specimen with an initial crack subjected to combined loadings. . . . 32
2.8 An imaginary two-step process to estimate the residual stress S_r in a shrunken soft adhesive bonded to a substrate. . . . 34
2.9 Estimations of the intrinsic energy release rates for blood clot, alginate/PNIPAm hydrogels, and cells. . . . 37

3.1 Schematics of design and proposed responses of stimuli-responsive hydrogel adhesives adaptive to external stimulation. . . . 48
3.2 Adhesion and fracture energy measurements. . . . 54
3.3 Analytical estimation of the strain energy release rate G on the hydrogel-tissue interface. . . . 57
3.4 Rheological and swelling measurements. . . . 58
3.5 FE model of the stimuli-responsive hydrogel adhesive. . . . 61
3.S1 Fabrication of the model tissue and the application of the stimuli-responsive adhesive. . . . 71

3.S2 Images and contours of the stimuli-responsive adhesive adhered onto the model tissue substrate before and after stimulation. 72
3.S3 Time series images of the stimuli-responsive adhesive with 2%w/v reagents. . 73
3.S4 Stress-stretch curves of the stimuli-responsive adhesive before and after stimulation in pure shear tests. 74
3.S5 Hysteresis curves of the alginate/PNIPAm DC hydrogels 75
3.S6 Analytical and numerical estimations of the equilibrium swelling ratio J . . . 76
3.S7 FE model geometry and cohesive zone. 77
3.S8 FE model with mode independent cohesive zone. 77
3.S9 FE model with the Mode-I dominant cohesive zone. 78
3.S10 Intrinsic energy release rate G_{in} under temperature increase. 78

4.1 Engineered network topology and linkages for multifaceted programming of hydrogel adhesion. 85
4.2 Design and characterization of topology-engineered adhesive (TEA). 89
4.3 Programmable adhesion kinetics of TEA. 92
4.4 Universal applicability of the TEA strategy. 95
4.5 Spatial programming and soft devices enabled with TEA 98
4.S1 Mechanical characterization of TEA and regular gels 112
4.S2 Micro-indentation test 115
4.S3 Cryosectioning of TEA gels 116
4.S4 Additional information on the adhesion mediated by different linkages 126
4.S5 Calibration of the slip-linkage mediated adhesion 127
4.S6 Additional information on the characterization of the adhesion kinetics . . . 128
4.S7 Additional information on the selective adhesion in double network TEA gels 129
4.S9 GPC test. 130
4.S8 3D printed mold for creating soft actuator modules. 131

5.1 Post-stimulation adhesion energy versus initial adhesion energy 137
5.2 The effective range of G_c to achieve high adhesion switch ratio for strategies of the stimuli-responsiveness and engineering polymer network topology . . . 138

List of Tables

4.1 Types of topological linkages, their constituents (adhesive network, targeted substrate, and bridging polymer), and the associated data. 121

List of Acronyms

alginate/PAAm	alginate and Poly(acrylamide) double network hydrogel.
alginate/PNIPAm	chitosan and Poly(N-isopropylacrylamide) double network hydrogel.
chitosan/PAAm	chitosan and Poly(acrylamide) double network hydrogel.
DN	double network.
LCST	Lower critical solution temperature.
PAAm	Poly(acrylamide).
PDMS	Polydimethylsiloxane.
PEHMA	Poly(2-hydroxyethyl methacrylate).
PNIPAm	Poly(N-isopropylacrylamide).
PSAs	pressure sensitive adhesives.
SN	single network.
SR	Swtich ratio = high (on) adhesion energy/low (off) adhesion energy.
TEA	Topology-engineered adhesive.
topohesive	adhesive solution containing bridging polymers to establish toplogical entanglement at an interface.

Chapter 1

Introduction

1.1 Background

Adhesive plays significant roles in numerous fields. There are examples in our everyday lives such as pressure sensitive adhesives (PSAs), cyanoacrylate (i.e., super glue), and epoxy, which are often used to achieve strong adhesion between two surfaces. However, they exhibit several drawbacks due to the fact that their mechanical and adhesion properties are difficult to modulate after the placement. For instance, hard adhesives such as super glue form stiff layers at the interface once set, creating substantial mechanical mismatch with the substrate. They are therefore undesirable in some applications that interface with biological tissues [1, 2] as they may restrict tissue movement. Materials capable of mimicking the mechanics of biological tissues and adapting their mechanical and adhesion properties are crucial for developing the next-generation adhesives, particularly in the context of emerging applications such as human-machine interfaces, soft robotics, haptics, etc.

Compared to these dry and hard conventional adhesives, hydrogels contain a large amount of water (typically $> 90\%$), resulting in their intrinsic wetness and softness. Hydrogels are three-dimensional hydrophilic polymer networks swollen in water solvents. Inside a hydrogel, water can freely migrate through the polymer network and can accommodate various chemical reactions just like in liquid water. This feature allows the hydrogel to serve as drug carriers [3] and sensors [4]. Meanwhile, the polymer network is crosslinked by covalent or physical crosslinkers, which provide elasticity and make hydrogel just like a solid. The elastic moduli E of hydrogels made of flexible polymers [5] are primarily entropic, meaning that $E \propto k_B T$, where $k_B T$ is energy in temperature. In comparison, the moduli of hard materials such as glass, ceramics, and metals scale with Coulumb energy which is 14 electron-volt ($14ev > 500 k_B T$ under room temperature). The significantly lower energy level of hydrogels compared to hard materials contributes to their extreme softness, with Young's modulus (E) typically ranging from $\sim$1 Pa to $\sim$10 MPa. This wide range of elasticity allows hydrogels to closely match the mechanical properties of many biological tissues [6]. Consequently, they find extensive applicability in human body and biological interfaces, including applications such as contact lenses [7] and tissue engineering [8].

In recent years, significant advancements have been achieved in the realm of tough hydrogel adhesion on various substrates. This type of adhesive achieving adhesion energy exceeding 1000 Jm^{-2} is dependent on an intrinsic adhesion energy (typically around 10 Jm^{-2}) arising from interfacial bonding, and substantial energy dissipation within the bulk material. The adhesion capabilities between hydrogels and tissue surfaces now rival those observed in biological organisms, such as the adhesion between cartilage and bone [9, 10]. The robust adhesion between hydrogel adhesives and tissues can create strong sealing and

offer great capability of mecahnical load transmitting, rendering them suitable for various applications, such as serving as tissue adhesives to transmit physiological loadings [11], acting as homeostatic adhesives to halt bleeding [9, 12, 13], and functioning as strain-programmable wound patches to accelerate wound healing [8, 14]. While these breakthroughs have opened up numerous opportunities in biomedical applications, with emerging and current applications spanning soft robotics, haptic interfaces, and medical devices, there is a growing demand for adhesion that not only possesses strength but also offers controllability, enabling effortless detachment and subsequent reuse, as well as the ability to establish adhesion during specific, well-defined time windows. In this context, controllability encompasses adhesion magnitude (adhesion energy or strength), adhesion kinetics (how quickly adhesion establishes), as well as spatial distribution (where the adhesion takes place). These aspects have become critical considerations in tailoring hydrogel adhesives to suit specific application requirements. An illustrative example of this demand is evident in wound patches, where secure adhesion to tissue substrates during the healing process is paramount. However, once tissue regeneration is undergoing, it becomes necessary for the adhesion to weaken, allowing for gentle removal to mitigate the risk of harm to the healed and delicate tissue. As another example, an adhesive with programmable adhesion kinetics can significantly enhance usability, surgical precision, enabling surgeons to accurately apply the adhesive to delicate areas of the tissue.

The development of smart soft adhesives capable of programmable or adaptive adhesion properties represents a cutting-edge research area that holds tremendous potential. While significant progress has been achieved [15, 16, 17, 18], several challenges persist in several scenarios. This chapter begins by reviewing the state-of-the-art techniques employed to establish robust hydrogel adhesion to diverse materials, and introducing the emerging concept of controllable adhesives. We then outline the objective of this dissertation.

1.2 Topological hydrogel adhesive

The adhesion of hydrogel is often quantified by adhesion energy G_c, which measures how much energy is needed to open the interface by a unit area. Hydrogels have intrinsically low adhesion energy to various substrates due to their high water content. A hydrogel polymer network contributes little to the adhesion with the substrate without interfacial bonding. The water molecules contained in the polymer network have low cohesive energy, thereby showing poor ability to transmit the load from the interface to the bulk. Therefore, hydrogels adhere to substrates mainly relying on the thermodynamic work of adhesion and is estimated to be on the order of 0.1 Jm^{-2} on different substrates [19]. To improve hydrogel adhesion, Yang

et al. [20], proposed a technique by applying a third species of polymers, called bridging polymers, to the interface to form topological entanglements between a hydrogel and a permeable substrate. Specifically, the bridging polymers can diffuse into both sides of the interface and be triggered to crosslink into a network through various types of intermolecular bonds [20, 21]. The crosslinked bridging network is topologically entangled with the two pre-existing networks. To break the interface, one of the polymer networks must rupture, which will relax a substantial amount of elastic energy to enhance hydrogel adhesion. This technique is often called "topological adhesion" and has led to strong adhesion between hydrogels (> 100 Jm^{-2}) and between hydrogels and tissue surfaces of different kinds. If the hydrogels are energy dissipative, the interfacial bridging polymer can elicit hysteresis in the bulk hydrogel to further amplify adhesion energy (> 1000 Jm^{-2}) [20].

Topological adhesion exhibits great versatility due to its potential integration into various interfacial bonding topologies for different substrates such as tissues, elastomers, glass, and metals. As a notable example, Li et al. [9] utilized EDC/NHS chemistry to form covalent bonds between the primary amine groups on the bridging polymers and the carboxylic acid groups on tissue surfaces. Meanwhile, the bridging polymers can diffuse into the hydrogel network and form topological interpenetration. Such a interfacial bonding structure leads to tough hydrogel adhesion > 1000 Jm^{-2} on porcine skin, and > 100 Jm^{-2} on porcine kidney and liver. In a similar fashion, Yang et al. [22] used bridging polymers to achieve strong adhesion between hydrogel and elastomers with no complementary function groups. The bridging polymers form covalent bonds with non-permeable elastomers while diffusing into the hydrogel matrix to form entanglement. Therefore, the robustness and versatility of the topological adhesion of hydrogels have enabled numerous applications in medicine, such as tissue adhesives [9], wound dressing [8], and wearable electronics [22]. Other techniques to strongly adhere hydrogels to substrates include directly anchoring hydrogel network onto substrates through covalent or non-covalent bonding [10, 17, 23].

1.3 Controllable adhesive

As an emerging class of adhesives, controllable adhesives are capable of modulating their mechanical properties and bonding states [15]. Fundamentally, the bonding state of an interface is dictated by fracture mechanics: the interface delamination is governed the competition between energy release rate G (the driving force for delamination) and adhesion energy G_c (the capacity to bond the interface). G is a mechanical property, depending on the loading conditions and geometry of the specimen. In contrast, G_c is a material property

which predominantly depends on the interfacial chemistry (Fig 1.1A) in a non-dessipative system. In a dissipative system, G_c can depend on the bulk dissipation, which is closely linked to the loading conditions [24]. The adhesion delamination happens when $G \geq G_c$.

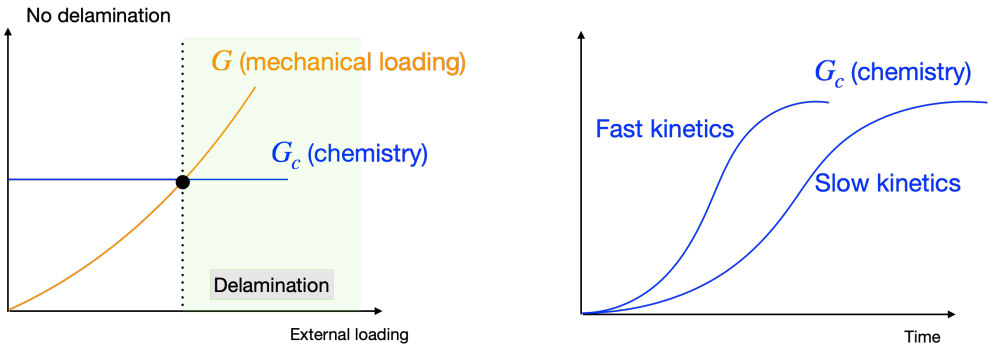

Fig. 1.1: (A) Qualitative figure showing how energy release rate G and adhesion energy G_c change with external loading in a non-dissipative system. (B) Qualitative figure showing the adhesion energy establishment with time.

To realize switching between "on" and "off" of the bonding state, it becomes necessary to perturb the equality $G = G_c$. To achieve this, inspirations can be drawn from the rich diversity of our nature, where various organisms demonstrate remarkable adaptability in their adhesive properties, including geckos, snails, and certain cells [25, 26, 27, 28]. These bio-inspirations indicate key design metrics that can be exploited to perturb the equality to alter the bonding state. In particular, Michael Bartlett and coworkers proposed a scaling relation [15, 29]:

$$F \sim \sqrt{\frac{A}{C}}\sqrt{G_c} \tag{1.1}$$

where F is the de-bonding force, A the contact area, C the system compliance, and G_c the adhesion energy. This scaling law demonstrates that the switching of a soft adhesive can be easily achieved by modulating critical factors including the contact area, system compliance, or adhesion energy [15], and has successfully described a variety of controllable adhesives ranging from biological adhesives such as Gecko's feet to synthetic adhesives such as the 3M command strip (Fig 1.2). To quantify the ability to switch adhesion, Andrew Croll and coworkers introduced the concept of the switch ratio (SR) which is calculated as the ratio of high (on) adhesion to low (off) adhesion [15]. In this thesis, we adhere to this convention. Given that hydrogel adhesives are typically characterized by their adhesion energy, we define SR as:

$$SR \equiv \frac{\text{high adhesion energy}}{\text{reference adhesion energy}} \text{ or } \frac{\text{reference adhesion energy}}{\text{low adhesion energy}} \tag{1.2}$$

where the reference adhesion energy is the initial adhesion energy without employing any switch mechanisms; the high and low adhesion energies are achieved by employing adhesion switch-on and switch-off mechanisms for controllable hydrogel adhesives, respectively.

Several notable synthetic controllable adhesive utilize compliance as the key parameter to alter the bonding state. One example is Geckskin, composed of Polydimethylsiloxane (PDMS) with embedded stiff inclusions, achieves unprecedented adhesion strength under zero-degree peeling due to its low compliance [29]. The same adhesive can be easily peeled off by increasing the peeling angle owing to the variable compliance under different loading conditions [29]. In another example, a Poly(2-hydroxyethyl methacrylate) (PHEMA) hydrogel can easily conform to rough substrates while in its wet state. Upon dehydration, the hydrogel "locks" in place with the substrate due to its reduced compliance, resulting in enhanced adhesion strength. Subsequently, the hydrogel can be easily detached via re-swelling to increase the compliance [26], resulting in the adhesion switch off.

An additional consideration in designing controlable adhesive is adhesion kinetics – how rapidly adhesion establishes over time (Fig 1.1 B). In this thesis, adhesion kinetics is quantified by the half time $t_{1/2}$ when the adhesion energy reaches half of its equailibrium value. In the case of covalent bond-based adhesion, the kinetics primarily hinge on the speed of interfacial bond formation. Fine-tuning adhesion kinetics can be achieved by carefully selecting reactants with the desired reaction kinetics at the interface. In contrast, adhesion based on physical bonds (e.g., hydrogen bonds) forms instantaneously upon contact, thus providing limited capability for modulating adhesion kinetics. Other physical strategies, such as polymer entanglement, rely on the reaction-diffusion of interfacial bridging polymers. Notably, Steck and coworkers have demonstrated that the kinetics of topological adhesion in hydrogels can be effectively tuned by adjusting the interfacial solution thickness [30].

1.4 Dissertation Scope

While the design metrics discussed above have successfully been exploited to guide the development of numerous controllable soft adhesives, achieving precise and reliable control of hydrogel adhesives is still challenging in many cases. This dissertation aims to develop controllable hydrogel adhesives by harnessing inherent adhesion control mechanisms, thus circumventing the complications arising from approaches involving chemical reactions and the like. Main objectives were listed as follows:

1. Comprehensively analyzing how hydrogel adhesion is influenced by stimuli, with a specific focus on temperature. This particular stimulus has the capability to initiate

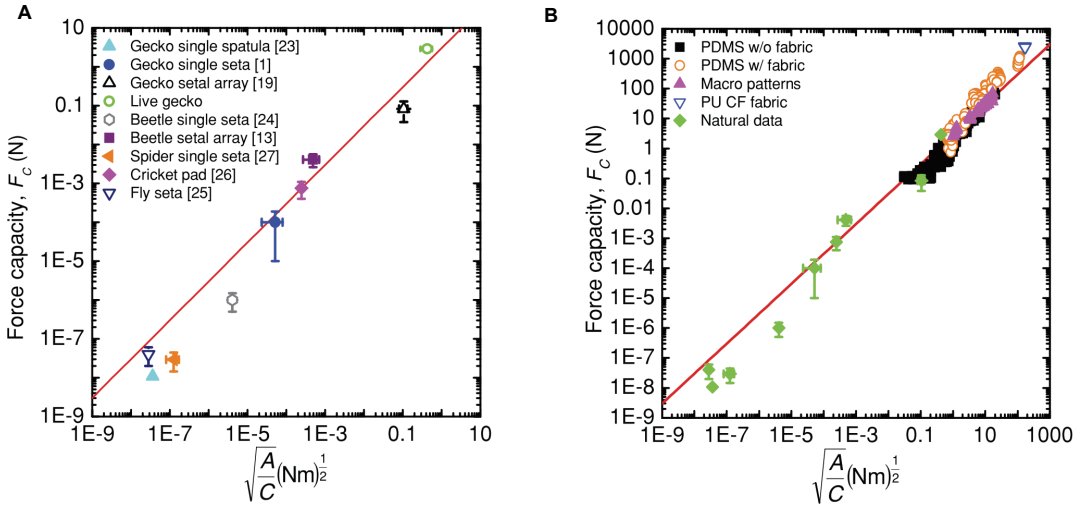

Fig. 1.2: Data adapted from [29], showing the scaling of force F to the ratio $\sqrt{\frac{A}{C}}$ for (A) biological adhesives and (B) synthetic elastomeric adhesives.

significant bulk deformation within the hydrogel, resulting in consequential changes in its bulk mechanics. These alterations in mechanical properties could potentially have a substantial impact on the bonding state of hydrogel adhesion, but this particular aspect has not been systematically explored thus far. Gaining a thorough understanding of these interactions could provide valuable insights for designing controllable hydrogel adhesives which utilize the bulk properties to alter the interfacial properties.

2. Investigating the relationship between hydrogel adhesion and the interfacial polymer entanglement of different topologies. This aspect represents a knowledge gap in the hydrogel adhesion field. This investigation will encompass a thorough exploration of how adhesion energy, kinetics, and spatial distribution are influenced by the specific characteristics of polymer entanglement at the interface. This understanding will play a pivotal role in advancing the development of hydrogel interfaces that possess programmable and controllable adhesion behaviors.

3. Designing and fabricating soft devices featuring programmable hydrogel interfaces. These devices are intended to achieve unprecedented functionalities, leveraging the capabilities of the hydrogel interface to modulate adhesion properties.

This dissertation is structured as follows.

- In Chapter 2, we review existing strategies used to modulate hydrogel adhesion, along with their associated complexities. Our attention then turns to the identification and

elucidation of key challenges tied to the integration of adhesion-controlling mechanisms into hydrogel adhesives. To overcome the limitations of current adhesion modulation methods, we propose innovative approaches that harness the mechanics of contraction and the physics of polymer entanglement. In the second half of Chapter 2, we aim at introducing the mechanics basis of the thesis. We will cover the basics of fracture and adhesion mechanics of soft materials, as well as various testing specimens and their interpretations. Additionally, we will introduce an analytical model to investigate the modulation of adhesion through the bulk contraction of soft active materials, which will be employed in Chapter 3.

- In Chapter 3, we study the adhesion modulated by the bulk contraction of soft materials using a stimuli-responsive hydrogel as a model system. We will investigate the spontaneously manifested intrinsic energy release rate and the variable bulk mechanics caused by stimulation and ascertain their roles in modulating the bonding state of the stimuli-responsive hydrogel adhesive. Relevant Journal: [J1].

- In Chapter 4, we take a different approach by developing a hydrogel adhesive with designed surface network topology to program multifaceted hydrogel adhesion. We ascertain the physics at play in the emergence of the programmable adhesion behaviors, including the kinetic bond breaking process and polymer diffusion. With the understanding, we develop novel soft devices with programmable adhesion interfaces to achieve unrepresented functionalities. Relevant Journal: [P1].

- In Chapter 5, we delve into the correlation between the two methods introduced in Chapters 3 and 4. Additionally, we present our concluding remarks and provide recommendations for future research directions.

Regarding the methodology, our investigation commences with mechanical experiments aimed at comprehensively characterizing the fracture and adhesion properties of hydrogels. This will be complemented by the implementation of analytical and numerical models, facilitating quantitative comparisons with the experimental data. Furthermore, we will showcase the feasibility of our controllable hydrogel adhesive through proof-of-concept demonstrations.

1.5 Publications

Preprint

[P1] Zhen Yang, Guangyu Bao, Ran Huo, Shuaibing Jiang, Xingwei Yang, Xiang Ni, Luc Mongeau, Rong Long, and Jianyu Li. Programming hydrogel adhesion with engineered polymer network topology. arXiv preprint arXiv:2303.16262, 2023.

Journal Papers

[J1] Zhen Yang*, Xingwei Yang*, Rong Long, and Jianyu Li. Stimulation modulates adhesion and mechanics of hydrogel adhesives. Langmuir, 37(23):7097–7106, 2021.
* These authors contribute equally

[J2] Xiang Ni*, Zhen Yang*, and Jianyu Li. Scaling behavior of fracture properties of tough adhesive hydrogels. ACS Macro Letters, 10(2):180–185, 2021.
* These authors contribute equally

[J3] Zhen Yang, Zhenwei Ma, Shiyu Liu, and Jianyu Li. Tissue adhesion with tough hydrogels: Experiments and modeling. Mechanics of Materials, 157:103800, 2021.

[J4] Guangyu Bao, Qiman Gao, Massimo Cau, Nabil Ali-Mohamad, Mitchell Strong, Shuaibing Jiang, Zhen Yang, Amin Valiei, Zhenwei Ma, Marco Amabili, et al. Liquid-infused microstructured bioadhesives halt non-compressible hemorrhage. Nature Communications, 13(1):5035, 2022.

[J5] Zhenwei Ma, Claire Bourquard, Qiman Gao, Shuaibing Jiang, Tristan De Iure-Grimmel, Ran Huo, Xuan Li, Zixin He, Zhen Yang, Galen Yang, et al. Controlled tough bioadhesion mediated by ultrasound. Science, 377(6607):751–755, 2022.

[J6] Zhenwei Ma, Zhen Yang, Qiman Gao, Guangyu Bao, Amin Valiei, Fan Yang, Ran Huo, Chen Wang, Guolong Song, Dongling Ma, et al. Bioinspired tough gel sheath for robust and versatile surface functionalization. Science Advances, 7(15):eabc3012, 2021.

[J7] Ran Huo, Guangyu Bao, Zixin He, Xuan Li, Zhenwei Ma, Zhen Yang, Roozbeh Moakhar, Shuaibing Jiang, Christopher Chung-Tze-Cheong, Alexander Nottegar, et al.

Tough transient ionic junctions printed with ionic microgels. Advanced Functional Materials, page 2213677, 2023.

[J8] Xuan Li, Yin Liu, Li Li, Ran Huo, Farshid Ghezelbash, Zhenwei Ma, Guangyu Bao, Shiyu Liu, Zhen Yang, Michael H Weber, et al. Tissue-mimetic hybrid bioadhesives for intervertebral disc repair. Materials Horizons, 10(5):1705–1718, 2023.

1.6 Contribution of authors

This manuscript-based thesis consists of one paper publication [J1] and one pre-print [P1]. The information of the papers and the author contributions are listed below.

J1. Stimulation regulates adhesion and mechanics of adhesive hydrogels

Zhen Yang[1,*], Xingwei Yang[2,*], Rong Long[2,◇], Jianyu Li[1,3,◇].

[1] Department of Mechanical Engineering, McGill University, Montreal, QC H3A 0C3, Canada

[2] Department of Mechanical Engineering, University of Colorado Boulder, Boulder, CO 80309, USA

[3] Department of Biomedical Engineering, McGill University, Montreal, QC H3A 0C3, Canada

[*] These authors contribute equally

[◇] Corresponding authors

Author contributions:

ZY designed and performed mechanical experiments to characterize the adhesion and fracture of stimuli-responsive hydrogels. He also performed experiments to characterize the thermodynamic swelling behavior of the hydrogel, and developed analytical model to estimate the intrinsic energy release rate. XY participate in the design of the mechanical and swelling experiments, as well as the development of the analytical model to estimate intrinsic energy release rate. XY developed a user-defined constitutive model and implement it in finite element modeling to simulate the bulk contraction of stimuli responsive hydrogels. ZY and XY both prepared figures. RL supervised the project, provided technical advice, analyzed the simulation and discussed the mechanisms. JL conceived idea, supervised the project, provided technical advice, analyzed the simulation and discussed the mechanisms. All authors contributed to the writing of the manuscripts.

P1. Programming hydrogel adhesion with engineered polymer network topology

Zhen Yang[1], Guangyu Bao[1], Shuaibing Jiang[1], Xingwei Yang[2], Ran Huo[1], Xiang Ni[1], Luc Mongeau[1,3], Rong Long[2], Jianyu Li[1,3,◇]

[1] Department of Mechanical Engineering, McGill University, Montreal, QC H3A 0C3, Canada

[2] Department of Mechanical Engineering, University of Colorado Boulder, Boulder, CO 80309, USA

[3] Department of Biomedical Engineering, McGill University, Montreal, QC H3A 0C3, Canada

♢ Corresponding authors

Author contributions:

ZY conceived idea, fabricated the hydrogels with dangling chains, designed and performed the adhesion energy and kinetics experiments, and analyzed the data by deriving the kinetic bond breaking model. ZY also performed uniaxial tensile test and micro-indentation test with Hertz contact mechanics to ascertain the size of the dangling chains. ZY further performed polymer diffusion experiments using florescent labeled chitosan, and prepared cyrosectioning samples for SEM imaging. Additionally, ZY fabricated the selective would patch, microfludic patch, re-configurable soft robotics. ZY prepared figures, wrote and revised manuscripts. GB prepared the florescent labeled chitosan polymers for the diffusion test. GB also helped with the synthesis of tough hydrogel with dangling chains. RH helped with hydrogel synthesis, carried out the adhesion of tough hydrogel with dangling chains on tissue surfaces, and designed the CAD model for fabricating soft robotics. SJ performed SEM imaging and the drug release experiment. XY helped derive the kinetic bond-breaking model and performed finite element simulation to complement the micro-indentation test data. XN measured adhesion energies of tough gels fabricated on different gelling molds. LM provide support for material characterization such as confocal imaging. RL provided technical advice, analyzed the results, proofread and revised the manuscript. JL supervised the project, provided technical advice, analyzed and discussed the results, proofread and revised manuscript.

Bibliography

[1] Monique Donkerwolcke, Franz Burny, and Dominique Muster. Tissues and bone adhesives—historical aspects. *Biomaterials*, 19(16):1461–1466, 1998.

[2] Vanessa Jones, Joseph E Grey, and Keith G Harding. Wound dressings. *BMJ*, 332(7544):777–780, 2006.

[3] Jianyu Li and David J Mooney. Designing hydrogels for controlled drug delivery. *Nature Reviews Materials*, 1(12):1–17, 2016.

[4] Andreas Richter, Georgi Paschew, Stephan Klatt, Jens Lienig, Karl-Friedrich Arndt, and Hans-Jürgen P Adler. Review on hydrogel-based ph sensors and microsensors. *Sensors*, 8(1):561–581, 2008.

[5] Michael Rubinsten. *Polymer Physics*. Oxford University Press, 2003. ISBN: 978-0198520597.

[6] Xinyue Liu, Ji Liu, Shaoting Lin, and Xuanhe Zhao. Hydrogel machines. *Materials Today*, 36:102–124, 2020.

[7] Fiona Stapleton, Serina Stretton, Eric Papas, Cheryl Skotnitsky, and Deborah F Sweeney. Silicone hydrogel contact lenses and the ocular surface. *The ocular surface*, 4(1):24–43, 2006.

[8] Serena Blacklow, Jianyu Li, Benjamin R Freedman, Mahdi Zeidi, Chen Chen, and David J Mooney. Bioinspired mechanically active adhesive dressings to accelerate wound closure. *Science Advances*, 5(7):eaaw3963, 2019.

[9] Jianyu Li, Adam D Celiz, Jiawei Yang, Quansan Yang, Isaac Wamala, William Whyte, Bo Ri Seo, Nikolay Vasilyev, Joost J Vlassak, and Mooney David J Suo, Zhigang. Tough adhesives for diverse wet surfaces. *Science*, 357(6349):378–381, 2017.

[10] Hyunwoo Yuk, Teng Zhang, Shaoting Lin, German Alberto Parada, and Xuanhe Zhao. Tough bonding of hydrogels to diverse non-porous surfaces. *Nature Materials*, 15(2):190–196, 2016.

[11] Benjamin R Freedman, Andreas Kuttler, Nicolau Beckmann, Sungmin Nam, Daniel Kent, Michael Schuleit, Farshad Ramazani, Nathalie Accart, Anna Rock, Jianyu Li, et al. Enhanced tendon healing by a tough hydrogel with an adhesive side and high drug-loading capacity. *Nature Biomedical Engineering*, 6(10):1167–1179, 2022.

[12] Guangyu Bao, Qiman Gao, Massimo Cau, Nabil Ali-Mohamad, Mitchell Strong, Shuaibing Jiang, Zhen Yang, Amin Valiei, Zhenwei Ma, Marco Amabili, et al. Liquid-infused microstructured bioadhesives halt non-compressible hemorrhage. *Nature Communications*, 13(1):5035, 2022.

[13] Hyunwoo Yuk, Jingjing Wu, Tiffany L Sarrafian, Xinyu Mao, Claudia E Varela, Ellen T Roche, Leigh G Griffiths, Christoph S Nabzdyk, and Xuanhe Zhao. Rapid and coagulation-independent haemostatic sealing by a paste inspired by barnacle glue. *Nature Biomedical Engineering*, 5(10):1131–1142, 2021.

[14] Georgios Theocharidis, Hyunwoo Yuk, Heejung Roh, Liu Wang, Ikram Mezghani, Jingjing Wu, Antonios Kafanas, Mauricio Contreras, Brandon Sumpio, Zhuqing Li, et al. A strain-programmed patch for the healing of diabetic wounds. *Nature Biomedical Engineering*, 6(10):1118–1133, 2022.

[15] Andrew B Croll, Nasibeh Hosseini, and Michael D Bartlett. Switchable adhesives for multifunctional interfaces. *Advanced Materials Technologies*, 4(8):1900193, 2019.

[16] Yang Gao, Kangling Wu, and Zhigang Suo. Photodetachable adhesion. *Advanced Materials*, 31(6):1806948, 2019.

[17] Xiaoyu Chen, Hyunwoo Yuk, Jingjing Wu, Christoph S Nabzdyk, and Xuanhe Zhao. Instant tough bioadhesive with triggerable benign detachment. *Proceedings of the National Academy of Sciences*, 117(27):15497–15503, 2020.

[18] Zhenwei Ma, Guangyu Bao, and Jianyu Li. Multifaceted design and emerging applications of tissue adhesives. *Advanced Materials*, 33(24):2007663, 2021.

[19] Jiawei Yang, Ruobing Bai, Baohong Chen, and Zhigang Suo. Hydrogel adhesion: a supramolecular synergy of chemistry, topology, and mechanics. *Advanced Functional Materials*, 30(2):1901693, 2020.

[20] Jiawei Yang, Ruobing Bai, and Zhigang Suo. Topological adhesion of wet materials. *Advanced Materials*, 30(25):1800671, 2018.

[21] Jason Steck, Jiawei Yang, and Zhigang Suo. Covalent topological adhesion. *ACS Macro Letters*, 8(6):754–758, 2019.

[22] Jiawei Yang, Ruobing Bai, Jianyu Li, Canhui Yang, Xi Yao, Qihan Liu, Joost J Vlassak, David J Mooney, and Zhigang Suo. Design molecular topology for wet–dry adhesion. *ACS Applied Materials & Interfaces*, 11(27):24802–24811, 2019.

[23] Hyunwoo Yuk, Claudia E Varela, Christoph S Nabzdyk, Xinyu Mao, Robert F Padera, Ellen T Roche, and Xuanhe Zhao. Dry double-sided tape for adhesion of wet tissues and devices. *Nature*, 575(7781):169–174, 2019.

[24] Yuan Qi, Julien Caillard, and Rong Long. Fracture toughness of soft materials with rate-independent hysteresis. *Journal of the Mechanics and Physics of Solids*, 118:341–364, 2018.

[25] Kellar Autumn, Yiching A Liang, S Tonia Hsieh, Wolfgang Zesch, Wai Pang Chan, Thomas W Kenny, Ronald Fearing, and Robert J Full. Adhesive force of a single gecko foot-hair. *Nature*, 405(6787):681–685, 2000.

[26] Hyesung Cho, Gaoxiang Wu, Jason Christopher Jolly, Nicole Fortoul, Zhenping He, Yuchong Gao, Anand Jagota, and Shu Yang. Intrinsically reversible superglues via shape adaptation inspired by snail epiphragm. *Proceedings of the National Academy of Sciences*, 116(28):13774–13779, 2019.

[27] Sabyasachi Rakshit, Yunxiang Zhang, Kristine Manibog, Omer Shafraz, and Sanjeevi Sivasankar. Ideal, catch, and slip bonds in cadherin adhesion. *Proceedings of the National Academy of Sciences*, 109(46):18815–18820, 2012.

[28] Valeri Barsegov and Devarajan Thirumalai. Dynamics of unbinding of cell adhesion molecules: transition from catch to slip bonds. *Proceedings of the National Academy of Sciences*, 102(6):1835–1839, 2005.

[29] Michael D Bartlett, Andrew B Croll, Daniel R King, Beth M Paret, Duncan J Irschick, and Alfred J Crosby. Looking beyond fibrillar features to scale gecko-like adhesion. *Advanced Materials*, 24(8):1078–1083, 2012.

[30] Jason Steck, Junsoo Kim, Jiawei Yang, Sammy Hassan, and Zhigang Suo. Topological adhesion. i. rapid and strong topohesives. *Extreme Mechanics Letters*, 39:100803, 2020.

Chapter 2

Literature review

2.1 Strategies in designing controllable hydrogel adhesives

Designing controllable hydrogel adhesives represents a challenging and cutting-edge research frontier. Specifically for hydrogel adhesives that interface with biological tissues, the incorporation of the controlled adhesion mechanisms requires careful consideration of mechanical properties, biocompatibility, surface interactions, and environmental conditions. For example, due to the much lower elastic moduli of hydrogels than the hard and elastomeric materials [1], and the wet ambient environment when interfacing with biological tissues, hydrogel adhesives may be difficult to be modulated through the design metrics indicated in Eqn. 1.1 in section 1.3:

1. One of the challenges lies in the change of compliance C. Hydrogels have intrinsically high compliance. Switching hydrogel adhesion by reducing compliance demands stiff inclusions, which can significantly increase the resistance to in-plane deformation, rendering the adhesive unable to conform to out-of-plane surfaces, particularly curved surfaces like many biological tissues. This constraint is dictated by Gauss' *Theorema Egregium*, a fundamental geometric principle [2].

2. The dehydration-induced mechanical interlocking in the hydrogel adhesive, as demonstrated by Cho et al. [3], may prove ineffective on wet and soft substrates like biological tissues. This is due to the presence of abundant ambient solvent that can hinder the hydrogel's de-swelling process.

3. The extreme softness of hydrogels allows them to undergo significant deformation, resulting in low shape-fidelity. This characteristic presents a challenge in switching hydrogel adhesion by precisely adjusting the contact area (A) of the hydrogel adhesives.

Consequently, recent studies concentrated on switching the adhesion energy of hydrogels Γ_a by using chemical reactions [4, 5, 6] or external apparatus triggers [7]. In the below, we focus on the existing approaches to modulate hydrogel adhesion in two aspects: adhesion energy and adhesion kinetics, and the ensuing complications.

2.1.1 Adhesion energy

To modulate the adhesion energy of hydrogel, various approaches have been proposed. Covalent-bond-based adhesion is generally strong and has high activation energy for bond breaking, the modulation of adhesion energy thus requires using specific chemistry to dissociate

the chemical bond at the interface. Chen et al. [5] applied detachment solution to a hydrogel adhesive, which diffuses through the hydrogel thickness to cleave the crosslinkers of the interfacial covalent bond. On the other hand, physical interactions such as polymer entanglement and hydrogen bond offer more flexibility to modulate adhesion energy. Yang et al.[4] demonstrated that the interfacial polymer entanglement can be dissociated by changing the pH near the interface, resulting in reduced adhesion energy.

For applications involving interactions with living tissues or biological systems, the materials used in controllable adhesives and the triggers to switch adhesion properties should ideally be non-toxic, biocompatible, and non-irritating to prevent harm to tissue substrates. However, the examples mentioned above often involve the diffusion of chemical species into the interface, which might not be ideal for biological tissues. Moreover, uncontrolled diffusion of chemical agents can complicate the process, especially with larger hydrogel dimensions. To avoid chemical diffusion, Gao et al. [6] employed photochemistry and UV light to trigger the dissociation of polymer entanglement for on-demand detachment. However, this method involves Fe^{3+} ions and UV irradiation, raising potential biocompatibility concerns.

A notable recent work by Ma et al. [7] utilized ultrasound to generate acoustic energy for the active anchoring of bridging polymers into the surface of porcine skin, replacing the need for chemical reactions. In cases where the bridging polymers are thermally responsive, such as gelatin, reapplying ultrasound at the interface can disrupt the bridging network to reduce adhesion. This chemistry-free approach to achieving strong bioadhesion opens up promising avenues for next-generation bioadhesives. However, ultrasound might not be feasible in situations involving temperature-sensitive substrates.

2.1.2 Adhesion kinetics

Before introducing the methods for modulating adhesion kinetics, we first go over the physics that governs the kinetics of topological hydrogel adhesion. When the bridging polymers diffuse into the hydrogel and substrate, they are simultaneously crosslinked into a network *in-situ*. The total kinetics encompasses the diffusion and the gelation processes of the bridging polymer. If covalent bonds are to be formed between bridging polymers and substrate, the total kinetics also involves the kinetics of chemical bond formation. Here, we limit our attention to a relatively simple case which only involves diffusion and gelation kinetics of the bridging polymers to reduce the number of parameters and to easily identify the physics at play.

Then let's consider an example when bridging polymers diffuse into two permeable hydrogels and crosslinked into a network. Since topological adhesion can be superfacial, it

implies that the bridging polymers only need to diffuse by one mesh size of the hydrogel to form entanglements sufficient to create strong adhesion. As a result, in topological adhesion the diffusion process takes negligible time and the total adhesion kinetics is dictated by the gelation kinetics of the bridging polymers [8].

The gelation process of bridging polymers involves a diffusion-reaction mechanism. Typically prepared as an aqueous solution, chitosan is a commonly employed bridging polymer with a pKa of 6.5. When applied to a hydrogel interface, protons from the chitosan solution rapidly diffuse away, leading to an increase in pH and subsequent deprotonation of the polymer chains. The deprotonated chitosan polymers then tend to form both inter- and intramolecular hydrogen bonds, culminating in the development of a network structure. Thus, the gelation of bridging polymers essentially relies on the diffusion of gelling agents, with protons serving this role in the case of chitosan. While a detailed investigation into the intricate reaction-diffusion process is complex, a simplified scaling analysis can provide insight into the time scale linked with the gelation process.

In this context, the thickness of the solution containing bridging polymers, denoted as h_{sol}, serves as a critical diffusion length scale. As such, the total kinetic time associated with adhesion follows an approximate relationship of $t \sim h_{\text{sol}}^2/D_{\text{gel}}$, where D_{gel} stands for the diffusion coefficient of the gelling agents.

Steck et al. [8] demonstrated in laboratory settings that the kinetics of hydrogel adhesion can be finely tuned by incorporating a nylon mesh immersed in a solution of bridging polymers. This mesh functions to define the thickness of the interfacial solution, denoted as h_{sol}. Their findings indicated a direct correlation between the kinetic time and the increased thickness of the nylon mesh, closely following the relation $t \sim h_{\text{sol}}^2/D_{\text{gel}}$. This suggests that the kinetics of topological adhesion can be deliberately programmed by altering the cast solution's thickness, h_{sol}. However, the precise control of h_{sol} in practical scenarios can be challenging, given its dependence on multiple operational parameters, including applied pressure at the interface, the wettability and viscosity of the bridging polymer solution, and more. This variability in operational conditions contributes to the uncertainty in hydrogel adhesion kinetics in real-world applications, partially accounting for the notable discrepancies reported in previous studies [4, 9] prior to the work of Steck et al. [8] ($t_{1/2}$ is reported in a wide range from $\sim$ 10s to $\sim$ 10 hours).

2.2 Controllable hydrogel adhesives through stimuli-responsiveness and engineered network topology

In this dissertation, we will explore different methods to control hydrogel adhesion: the stimuli responsiveness and the topology of the interfacial polymer entanglement. The former produces a spontaneous energy release rate and variable bulk mechanics which can be exploited to modulate bonding state, while the latter enables direct modulation of the adhesion energy. Different from the conventional approaches, these mechanisms can be directly embodied as part of hydrogels themselves, similar to other material properties such as elasticity. They would enable unprecedented adhesion behaviors of hydrogel adhesives. In this section, we will review the key concepts of these two mechanisms, and discuss some examples from nature that have inspired the development of this thesis.

2.2.1 Mechanically active soft adhesives

Compared to the conventional adhesive materials which are largely mechanically passive, many biological and soft matters are mechanically active. Examples include blood clots and biological cells. Blood clots, biopolymer networks that form during vascular injury, exhibit active mechanical behaviors [10]. When bleeding happens, platelets protrude filopodia to bind the fibrin network. Actomyosin-based contraction of individual platelet then leads to the macroscopic volume shrinkage of the blood clot [11, 12], resulting in increased modulus (Fig 2.1A). The active mechanics of blood clot has strong implications on hemostasis and thrombosis [13, 14].

Similarly, cells are known to change their volume and mechanical properties in responding to the change in osmotic pressure or stiffness of the tissue micro-environments, showing increased moduli with decreasing cell volume[15] (Fig 2.1B). They also actively contract the soft extracellular matrix (ECM) to realize numerous cellular behaviors such as cell migration, differentiation, proliferation, etc [16].

Similar to biological cells and blood clots, hydrogels can easily undergo large deformation and change their volumes. For instance, hydrogels swell in θ or good solutions [18]. The extent of swelling is dictated by the interplay between osmosis and elasticity [19]. For non-ionic hydrogels like polyacrylamide (PAAM), the osmosis is contributed by the mixing of polymers and solvents (e.g., water) Π_{mix}, and the elasticity is contributed by the stretching of the crosslinked polymer network Π_{el}. The thermodynamic mixing drives the solvent to diffuse into the polymer network, while the elasticity prevents the network from swelling. The osmosis

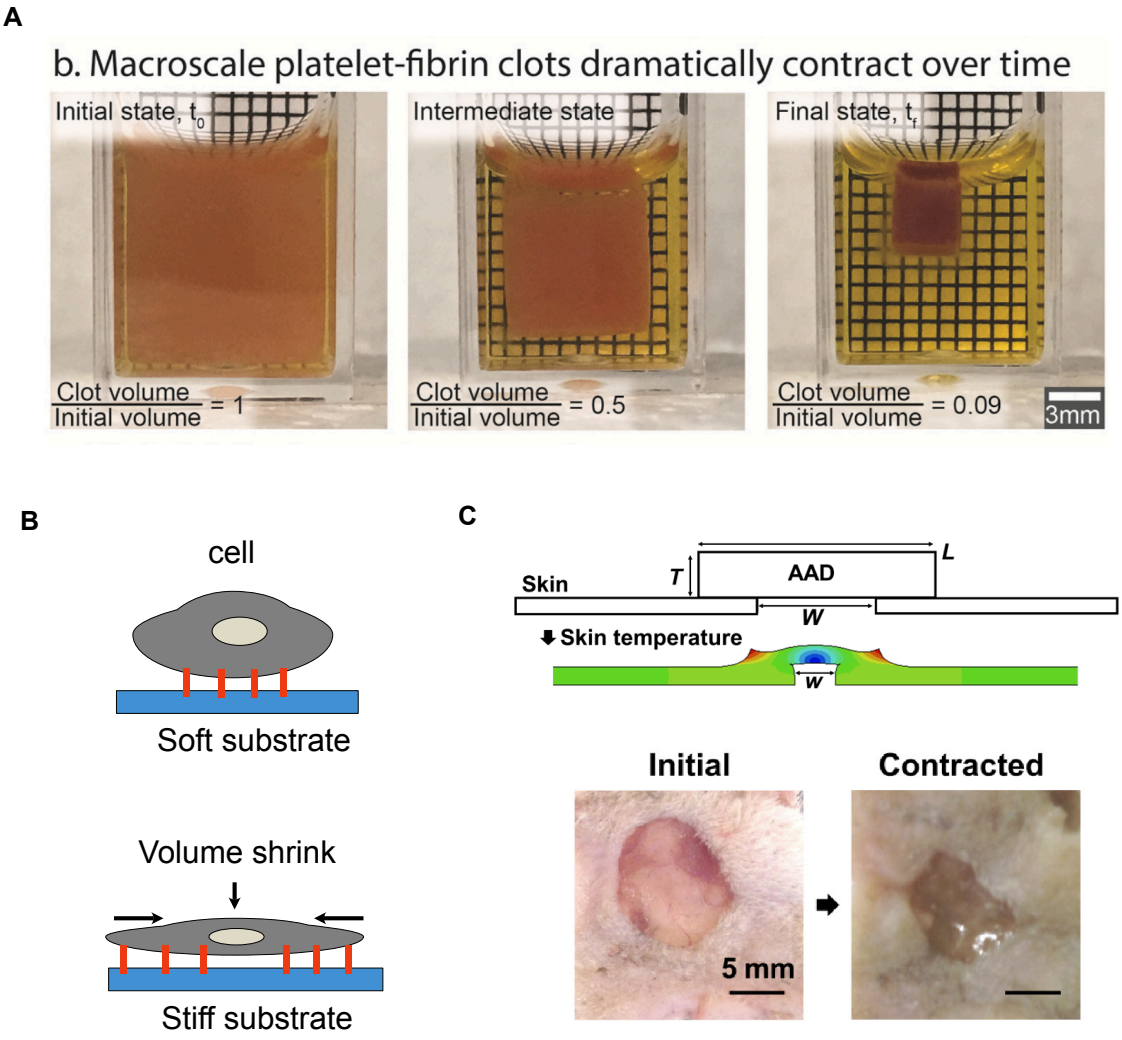

Fig. 2.1: Mechanically active materials. (A) A blood clot contracts upon the activation of platelets (adapted from [12]). (B) A cell spreads out and contracts volume when sensing a stiff substrate. (C) A bio-inspired active wound dress contracts the underlying wounded tissue in responding to skin temperature (adapted from [17]).

and elastic pressures balance at equilibrium [18]. A wide variety of applications in hydrogel actuators manifested [20, 21, 22, 23] based on the osmosis principle.

The deformation or volume change of hydrogels can also be triggered by external stimuli, and this class of hydrogels is referred to as stimuli-responsive hydrogels. Their polymer chains or networks can be regulated by chemical (ion concentration, pH, proteins) [24, 25] or physical (temperature, light electrical or magnetic fields) [26, 27] cues to undergo configurational transitions (e.g., polymer chains change from random coil to collapsed globule states or networks change from swollen to shrunk states). Such changes at the molecular level leads to the variation in the volume and mechanical properties on the macroscopic scale. One

classic example of stimuli-responsive hydrogels is poly(N-isopropylacrylamide) (PNIPAm) [28], whose volume reduces when its temperature is increased above the lower critical solution temperature (LCST). Fundamentally, the thermo-responsiveness of PNIPAm is related to a discontinuity in the solubility of the polymer network in the aqueous solution above LCST. The abrupt change in the solubility is accompanied by a drastic conformational transformation: the polymer network undergoes an abrupt collapse and the water molecules are squeezed out from the polymer network, causing phase separation and drastic volume shrinkage. PNIPAm has been extensively used in temperature sensors and actuators because the temperature is a broadly accessible stimulus [29, 30]. In the biomedical field, Blacklow et al.[17] recently reported a tough wound dressing adhesive composed of alginate/PNIPAm double network hydrogel. The adhesion at the hydrogel-tissue interface is achieved through a species of bridging polymer chitosan. One end of the bridging polymer is chemically anchored on the tissue surface while the other end is in topological entanglement with the hydrogel network to enable robust adhesion. The resulting adhesive spontaneously contracts in response to the body temperature ($\sim 37°C$), and the strong interfacial adhesion transmits the contractile force to the tissue to accelerate wound closure (Fig 2.1C).

The active mechanics of the stimuli-responsive hydrogel provides a solution to modulate adhesion energy without using chemistry to dissociate the interfacial bonds. In principle, the active contraction of a hydrogel adhesive can raise residual stress at the interface, contributing to an energy release rate for interfacial delamination, which is hereafter referred to as the intrinsic energy release rate G. Distinct from the conventional energy release rate provided by external loadings, G manifests spontaneously when the contraction of the hydrogel is triggered by stimuli. Presumably, G can be exploited to partially or entirely offset the adhesion energy Γ_a at a hydrogel-substrate interface, such that the apparent adhesion energy can be reduced. Therefore, the hydrogel adhesion can be effectively tuned by varying G (triggered by stimuli) or Γ_a (prescribed by interfacial chemistry). This approach relies solely on the mechanics of the hydrogel matrix, thus eliminating the issues raised due to the use of chemistry. To effectively exploit the intrinsic energy release rate, a quantitative tool is desired to study the relation between G and hydrogel contraction, as detailed in section 2.5.

2.2.2 Slip-bond-based adhesion in biological organisms and synthetic interfaces

The second inspiration of this thesis is the slip bond largely observed in the adhesion of biological organisms. Biological cells have been found to utilize slip bonds for migration and

other physiological processes [31, 32]. These bonds are based on non-covalent protein-protein interactions and exhibit shorter life time and dynamic adhesion strength under higher applied forces (Fig 2.2A), allowing cells to easily switch between bonding and motile states under different physiological environments [33].

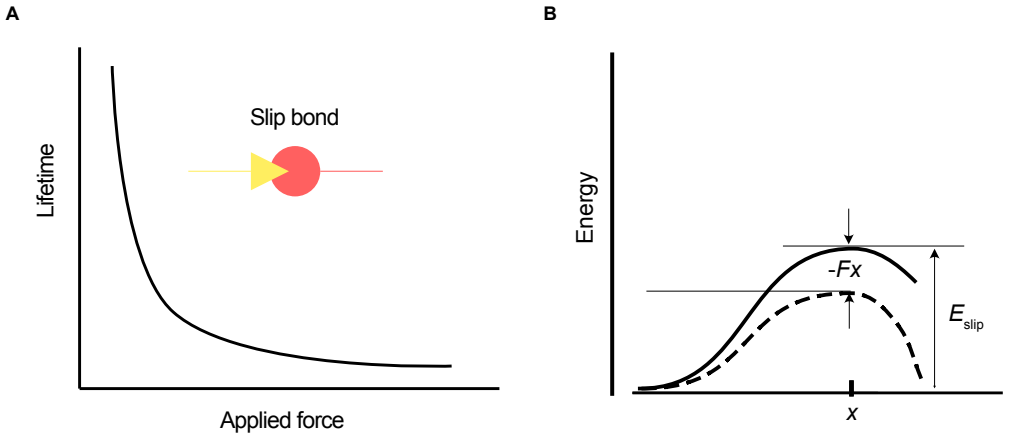

Fig. 2.2: (A) Schematic showing the lift time of a slip bond versus the applied tensile force. (B) Schematic showing that the energy landscape of a slip bond along a reaction coordinate. As a first-order approximation, the activation energy of slip bond dissociation E_{slip} is decreased by Fx, where F is the applied force and x is the extension.

Such bond behavior was first mathematically described by Bell [34], wherein the slip bond dissociation was treated as a first-order chemical reaction (Fig 2.2B). The applied force reduces the activation energy for bond dissociation, thereby increasing the probability of bond rupture. This phenomenon is often called "thermally-activate" or "kinetic" bonding breaking process, and results in intrinsically rate-dependent bond strength observed in the adhesion at the elastomer interfaces [35], structure adhesive interfaces [36], and other bonds [37]. A notable feature of the kinetic bond breaking-based adhesion is that the rate-dependent adhesion is only confined at the interface thus can be decoupled from the rate-dependent bulk dissipation. Consequently, the incorporation of the kinetic bond breaking-based adhesion in soft adhesive interfaces may enable tunable adhesion with a high bulk resilience, which is crucial in soft robotics for efficient energy storage and release [38]. However, such adhesion behavior has rarely been reported in hydrogel adhesion systems. This could be partially attributed to the high stiffness of interfacial bonds, including covalent bonds and polymer entanglements, minimizing the rate-dependent effect of bond rupture kinetics (detailed later). New interfacial bonding strategies of hydrogels are demanded to mimic the slip bonds in biological systems and to facilitate the development of controllable adhesives.

2.2.3 Topology of polymer entanglement

In this thesis, we propose an interfacial bonding strategy to mimic slip bonds by designing the interfacial polymer entanglement topology. Polymer entanglement has been extensively studied and shown strong impacts on the viscoelasticity of polymer melts [39], and elastic moduli [40, 41] and fracture [42, 43] of polymer networks. Polymer entanglement forms when two polymer chains interact with each other. In principle, if the two entangled polymer chains are respectively crosslinked into networks, the entangled chains can not disentangle even in a sufficiently long time scale (Fig. 2.3A). This topology of polymer entanglement is hereafter referred to as a "stitch" topology and the polymer entanglement is called a "stitch linkage". To rupture the stitch linkage, one of the polymer chains must rupture, releasing the elastic energy stored in each bond of the chain prior to rupture due to the Lake-Thomas effect [44]. The stiffness of the stitch linkage before rupture is also expected to be relatively high due to the full extension of the entangled chains beyond their entropic elasticity (Fig. 2.3C). In contrast, if in an entanglement one of the entangled chains is not completely crosslinked into the network, i.e., a dangling chain, the entanglement can easily disentangle in a time scale longer than the relaxation time of chain slippage, and no polymer chains are needed to rupture during the process (Fig. 2.3B). This topology of polymer entanglement is hereafter referred to as a "slip" topology and the polymer entanglement is called a "slip linkage".

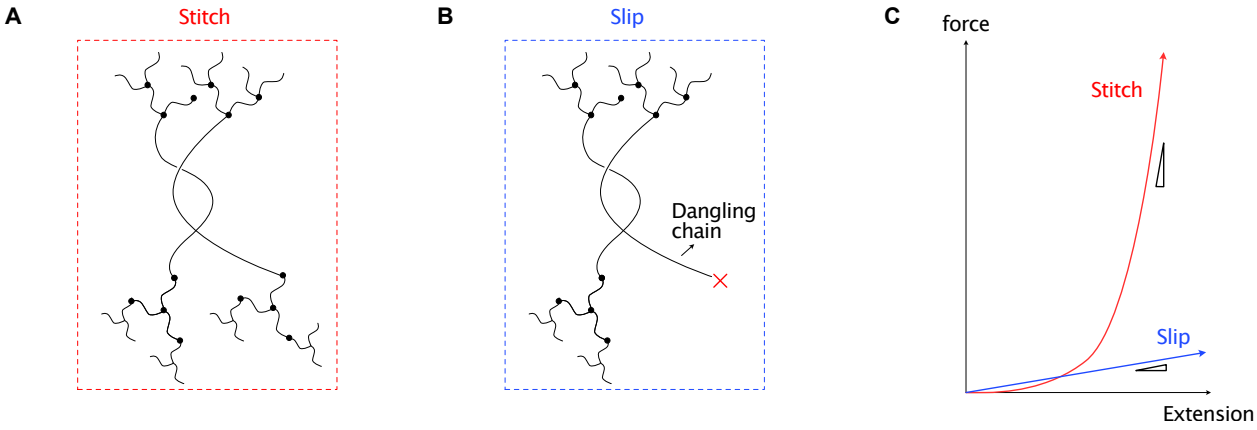

Fig. 2.3: Schematics of different polymer entanglement topologies. (A) stitch linkage. (B) slip linkage. (C) Qualitative illustration of the force-extension curves of stitch and slip linkages

Importantly, since the dissociation of slip linkage demands no bond rupture, the polymer chains are expected to remain entropic with low stiffness during slippage, a condition at which the slip-bond-based adhesion is expected to manifest (Fig. 2.3(C)). Additionally, if the entangled polymer chains are polar, they may form intramolecular bonds such as hydrogen bonds within the slip linkage. During the chain slippage, the hydrogel bonds can

break and re-form, resulting in finite activation energy for disentanglement to enable strong adhesion. The two mechanisms together are expected to result in strong and rate-dependent hydrogel adhesion that mimics the slip bonds in biology. Furthermore, gaining insight into the association kinetics of polymer entanglement could facilitate the development of hydrogel adhesives with controllable adhesion kinetics. The spatial arrangement of polymer entanglement may also enable controlled spatially heterogeneous adhesion energy. Therefore, designing the polymer entanglement topology at a hydrogel interface holds a great potential to program the multifaceted hydrogel adhesion, as detailed in Chapter 4.

In the rest part of the chapter, we aim at introducing the basis of experimental mechanics of soft materials that this thesis is rooted on. Key concepts of fracture mechanics and the interpretation of various fracture and adhesion testing specimens will be reviewed in detail. We will also provide an analytical model which will be used to study the active contraction-driven delamination of the soft active materials in chapter 3.

2.3 Griffith criterion for fracture propagation

Consider a deformable body containing a crack subjected to external loadings. Griffith utilized the first law of thermodynamics to cracks to define a critical condition for the crack to propagate in steady state:

$$\frac{dU_T}{dA} = \frac{d\Pi}{dA} + \frac{dU_S}{dA} = 0, \tag{2.1}$$

where U_T is the total energy, Π is the potential energy of the elastic body, U_S is the surface energy, dA is an incremental of the crack surface growth. Eqn.(2.1) also implies that during a quasi-static differential crack growth dA, the decrease in the total potential energy of the body overcomes the energy required to create new surfaces.

$$-\frac{d\Pi}{dA} = \frac{dU_S}{dA}. \tag{2.2}$$

The left hand side of Eqn. 2.2 is defined as the applied energy release rate G, while the right hand side can be written as the fracture energy of the body G_c:

$$\begin{aligned} G &= -\frac{d\Pi}{dA} = \frac{d\left(W - U_E\right)}{dA}, \\ G_c &= \frac{dU_s}{dA} \end{aligned} \tag{2.3}$$

where W is the external work input to the loaded body, U_E is the internal elastic energy.

Combining Eqn. 2.3 and Eqn. 2.2, we can write the common form of the Griffith criterion for non-dissipative system: $G = G_c$, or

$$dA \cdot G_c = dW - dU_E \tag{2.4}$$

The Griffith criterion states that when the applied energy release rate G (or equivalently the change of the potential energy with an incremental crack growth $d\Pi/dA$) reaches a critical value G_c, the crack propagation starts. G_c is commonly considered as a material property in non-disispative systems. In highly dissipative system, G_c may depend on loading and geometrical conditions of the fracture test. This approach is widely used to understand both bulk and interfacial fractures in different testing specimen such as peeling, shearing, etc, to correlate the measured data to the critical value G_c.

2.4 Fracture and adhesion testing specimens for soft materials

2.4.1 Peeling

Based on the Griffith's approach to study fracture in the deformable body, we next review the fracture analysis of several fracture/adhesion testing specimens including peeling, lap-shear, and pure shear tests, which are used throughout the thesis.

For analyzing the peeling test, it is convenient to construct the total energy:

$$U_T = U_S + U_P + U_E \tag{2.5}$$

where U_T, U_S, U_E are defined in section 2.3, and U_P is the potential energy associated with external loadings. Applying Griffith approach Eqn. 2.1 to analyze a steady-state peeling process yields:

$$\frac{dU_T}{dA} = \frac{dU_S}{dA} + \frac{dU_P}{dA} + \frac{dU_E}{dA} = 0 \tag{2.6}$$

Rearranging Eqn. 2.6 leads to

$$G_c = -(\frac{dU_P}{dA} + \frac{dU_E}{dA}) \tag{2.7}$$

Eqn. 2.7 is identical to Eqn. 2.4 with $U_P = -W$. Here, G_c is interpreted as the adhesion energy of the interfacial crack between adherends subjected to the peeling test. For convenience, we attached a flexible and inextensible backing to the adhesive to be peeled, so that there is no

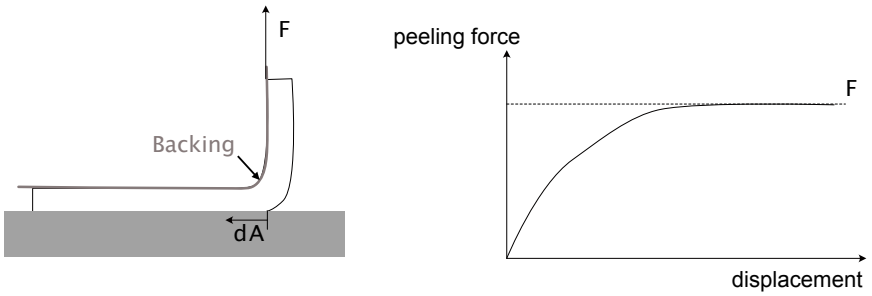

Fig. 2.4: (left) Schematic of peeling test. (right) Typical force-displacement curve of peeling test with steady-state peeling force F.

extension in the peeled part of the material. The peeling process thus becomes translational-invariant with no variation in the strain energy during the interfacial crack propagation, $dU_E/dA = 0$. For 90° and 180° peeling tests, $U_p = -FA/w$ and $-2FA/w$, respectively, where w is the width of the adhesive, and F is the steady-state peeling force. Taken together, we obtain the peeling force-adhesion energy relation:

$$\begin{aligned} G_c &= \frac{F}{w} \text{ for } 90^\circ \text{ peeling,} \\ G_c &= \frac{2F}{w} \text{ for } 180^\circ \text{ peeling} \end{aligned} \tag{2.8}$$

2.4.2 Modified Lap-shear

Similarly, we use Griffith's approach to analyze lap-shear test in Fig. 2.5. During the process, a crack on the interface grows by dA at the expenses of the bonded region of $dA' = -dA$. The materials in the debond and bonded regions are under shear strains γ_c' and γ_c, respectively, so that the strain energy densities in the debonded and bonded regions can be written as $\Phi(\gamma_c')$ and $\Phi(\gamma_c)$. We attached a inextensible and flexible backing film to the hydrogels, such that the potential energy of the force in both bonding and debonded regions are $-F \cdot q \cdot A/(A' + A)$ and $-F \cdot q \cdot A'/(A' + A)$, where q is the applied displacement between the loading ends. The potential energy of the debonded and bonded regions can be written as $A\left(\Phi(\gamma_c)h - F \cdot q/(A' + A)\right)$ and $A'\left(\Phi(\gamma_c')h - F \cdot q/(A' + A)\right)$, respectively. We attached a flexible and inextensive backing film to the hydrogel, such that the displacement q is independent of the crack area A. We further assume that the material is full unloaded in the debonded region so that $\gamma_c' = 0$ and $\Phi(\gamma_c') = 0$. These conditions lead to the following expression of G_c in lap-shear test:

$$G_c = \Phi(\gamma_c)h \tag{2.9}$$

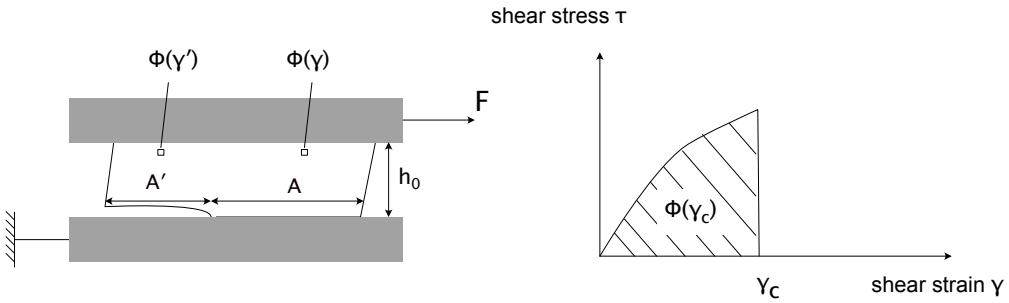

Fig. 2.5: (left) Schematic of the modified lap-shear test for measuring the adhesion energy between hydrogel and substrate. (right) Typical shear stress-shear strain curve. The strain energy density in the bonded region is calculated as $\Phi(\gamma_c) = \int_0^{\gamma_c} \tau d\gamma$.

The geometrical interpretation of $\Phi(\gamma_c)$ is the area under the shear stress-strain curve from $\gamma = 0$ to γ_c corresponding to the onset of crack propagation (Fig.2.5). In experiments, γ_c is often taken to be the critical strain when the shear stress reaches maximum. Note that the form of the potential energy of the sample implies that the debonded and bonded regions are under homogeneous deformation. Near the crack front, the deformation is inhomogeneous, but the size of the inhomogeneous field is small compared to the overall sample size. During the crack propagation, the inhomogeneous field follows translational invariance, thus its information does not enter the expression of the adhesion energy (Eqn. 2.9).

2.4.3 Pure-shear

Finally, we use Griffith's approach to analyze pure-shear test which is extensively used to characterize the fracture energy of hydrogels [45, 46, 47]. During a typical pure-shear test, the materials in the debond and bonded regions are under stretches λ' and λ, respectively, so that the strain energy densities in the debond and bonded regions can be written as $\Phi(\lambda')$ and $\Phi(\lambda)$, respectively (Fig. 2.6 (A)). The potential energy of the force applied to the whole sample is $-F \cdot q$. The elastic energy of the debond and bond regions are $\Phi(\lambda')A'h_0$ and $\Phi(\lambda)Ah_0$, respectively. The total energy for the debond and bond regions are $A'\left(\Phi(\lambda')h_0 - F \cdot q/A'\right)$ and $A\left(\Phi(\lambda)h - F \cdot q/A\right)$, respectively.

If the crack starts steady-state propagation at a critical stretch λ_c, Eqn. 2.4 holds. Since the material in the debonded region is fully unloaded $\lambda_c' = 0$ and $\Phi(\lambda_c') = 0$. In addition, the applied displacement is independent of the crack growth A. Thus, the final expression of G_c for the pure shear test is given by:

$$G_c = \Phi(\lambda_c)h_0 \tag{2.10}$$

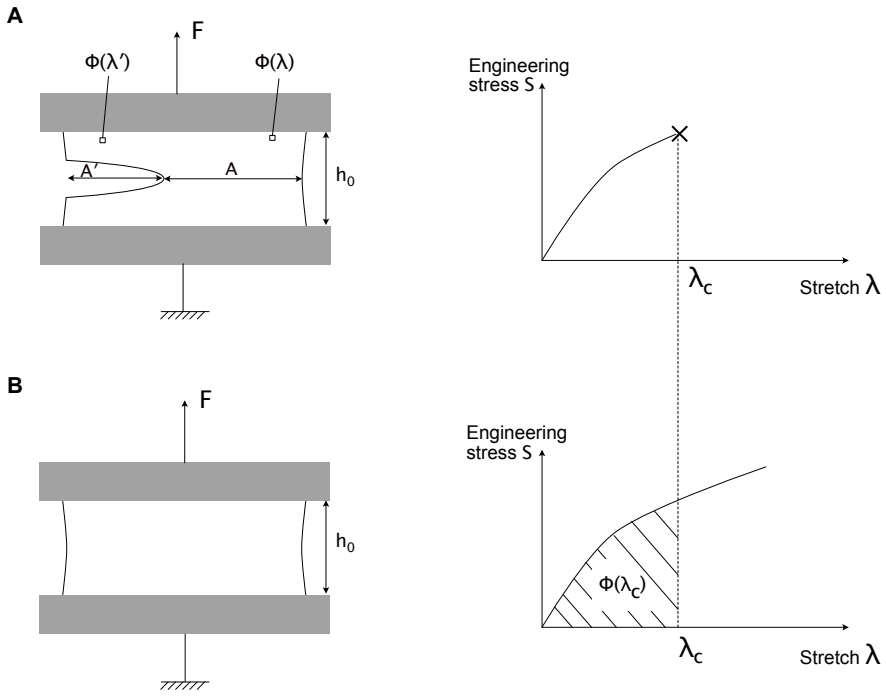

Fig. 2.6: (left) Schematics of pure shear test for measuring fracture energy of soft materials. (right) Representative stress-stretch curves from the pure shear test. (A) A notched sample is stretched to a critical stretch λ_c when the crack starts propagation. (B) An unnotched sample is stretched to λ_c. The strain energy density is calculated as $\Phi(\lambda_c) = \int_1^{\lambda_c} S(\lambda) d\lambda$.

To obtain $\Phi(\lambda_c)$, a separate sample without a notch is loaded to λ_c. $\Phi(\lambda_c)$ can be estimated as the area under the stress-stretch curves $\Phi(\lambda_c) = \int_1^{\lambda_c} S d\lambda$ for the unnotched sample (Fig 2.6B).

2.5 Interface delamination of soft active materials

Compared to the conventional hard materials which are largely "mechanically passive", some soft and biological materials such as cells, blood clots, and stimuli-responsive hydrogels exhibit "active mechanics" in responding to stimuli, as discussed in detail in section 2.2.1. For example, stimuli-responsive hydrogels like PNIPAm shrink their volume when temperature is raised above their LCST [28]. A monolayer of epithelial cells contact the substrate during collective migration [48]. For a soft active material that is initially adhered to a substrate with a prescribed adhesion energy G_c, its volume shrinkage is confined in the plane parallel to the interface, thus causing residual strain and stress to develop in the material. Consequently, the interface with an initial crack can develop intrinsic energy release rate G without external loadings, lowering the adhesion energy to $G_c - G$. To delaminate this pre-strained interface,

the applied strain energy release rate G_{ap} supplied by external loadings becomes lower than the adhesion energy:

$$G_{\text{ap}} = G_c - G \tag{2.11}$$

The right hand side of Eqn. 2.11 is the apparent adhesion energy. The total energy release rate can be written as the sum of the intrinsic and applied parts: $G_{\text{tot}} = G + G_{\text{ap}}$.

Eqn. 2.11 dictates that if $G > G_c$, the soft active material may delaminate without external loading. Such delamination phenomena were often observed in the semiconductor industry, wherein the thin metal or ceramic films bonded to rigid substrates delaminate when subjected to thermal mismatch [49, 50], but is less explored in soft active material systems. If $G < G_c$, the apparent adhesion energy becomes lower than the intrinsic adhesion energy; if $G \ll G_c$, the intrinsic energy release rate has negligible effect on the interface delamination. It is therefore critical to quantify G for general types of soft active materials adhered to an substrate. In this section, we provide an analytical model to estimate G based on the mixed-mode fracture mechanic proposed by Suo and Hutchinson [49].

The framework of the mixed-mode fracture considers a problem illustrated in Fig. 2.7 [49]. Two materials with different mechanical properties (E: Young's modulus, ν: Poisson's ratio) are bonded to each other with an initial interfacial crack. The composite is subjected to combined loadings P_i and M_i where $i = 1, 2, 3$. Here, P is the force per unit length and M is the moment per unit length. Mechanical equilibrium asks the following to hold:

$$\begin{aligned} &P_1 - P_2 - P_3 = 0, \\ &M_1 - M_2 + P_1\left(\frac{h_1}{2} + h_2 - \delta\right) + P_2\left(\delta - \frac{h_2}{2} - M_3\right) \end{aligned} \tag{2.12}$$

Since the interfacial crack lies between materials 1 and 2 are mediated by the in-plane stress σ_{12} and σ_{22}, the superposition of a globally imposed stress σ_{11} in Fig. 2.7b would not alter the stress field near the crack tip in Fig. 2.7a. Thus, the crack tip field in Fig. 2.7a is equivalent to that in Fig. 2.7c with a reduced number of equivalent loadings P_e, M_e, and M_e*, which are related to P_i and M_i through [49]:

$$\begin{aligned} P_e &= P_1 - C_1 P_3 - C_2 \frac{M_3}{h_1} \\ M_e &= M_1 - C_3 M_3 \\ M_e* &= M_e + \frac{P_e\,(h_1 + h_2)}{2} \end{aligned} \tag{2.13}$$

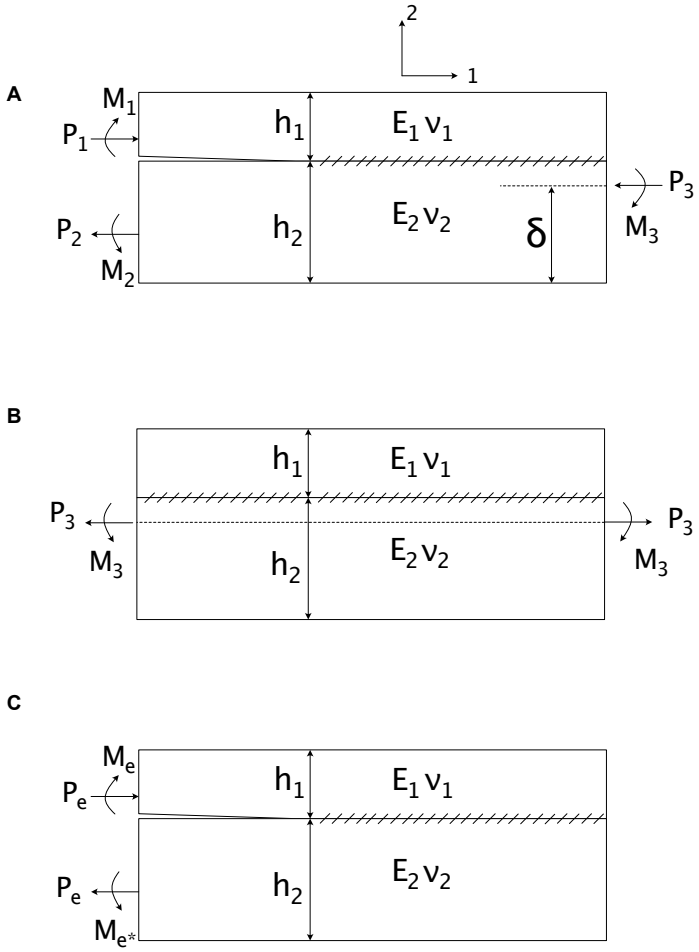

Fig. 2.7: (A) Schematics of a bi-material specimen with an initial crack subjected to combined loadings P_i and M_i. (B) a bi-material specimen with no interfacial cracks subjected to loadings P_3 and M_3, such that only σ_{11} is expected in the specimen. (C) Superposed loadings in (A) and (B).

where the expressions of C_1, C_2, and C_3 can be found in Appendix.

The strain energy release rate G for the interfacial crack can be expressed in terms of equilvalent loadings P_e and M_e, and can be computed by comparing the total energies in the bonded and debonded regions [49]:

$$G = \frac{1}{8\mu}\left[\frac{P_e^2}{Ah_1} + \frac{M_e^2}{Ih_1^3} + 2\frac{P_e M_e}{\sqrt{AI}h_1^2}\sin\gamma\right] \tag{2.14}$$

with the geometrical factors given by:

$$\begin{aligned} \frac{1}{A} &= 1 + \Sigma(4\eta + 6\eta^2 + 3\eta^3) \\ \Sigma &= \frac{1+\alpha}{1-\alpha} \\ \frac{1}{I} &= 12(1+\eta^3) \\ \frac{\sin\gamma}{\sqrt{AI}} &= 6\eta^2(1+\eta) \end{aligned} \tag{2.15}$$

where $\eta = h_1/h_2$. α is the Dundurs parameter[51]:

$$\alpha = \frac{\mu_1/\mu_2(4-4\nu_2) - (4-4\nu_1)}{\mu_1/\mu_2(4-4\nu_2) + (4-4\nu_1)}$$

The essential idea to estimate G due to the shrinkage of a soft material is that we relate the stress state in the soft active material contracting on a substrate to that of an undeformed soft material but subjected to residual stress. Fig. 2.8 illustrates the problem of interest, where a soft material (denoted as material 1) shrinks its volume and bonded to a substrate (denote as material 2). We simplify the problem to 2-dimensional by assuming plane strain condition. The two materials are assumed to be isotropic and elastic with incompressibility indicating that $\nu_1 = \nu_2 = 0.5$. The soft material thus has a shear modulus $\mu_1 = E_1/3$, and initial thickness h_1, while the substrate has a shear modulus $\mu_2 = E_2/3$ an initial thickness h_2. We assume $h_1 = h_2$ for simplification. We further simply our problem by assuming the substrate to be rigid so that $\mu_1 \ll \mu_2$. The simplifications lead to $\eta = 1$, $\alpha = -1$, and $\Sigma = 0$ in Eqn. 2.5.

Upon the volume shrinkage of the soft material, it develops a residual stress S_r (nominal stress with respect to the undeformed configuration). The problem is realized through an imaginary two-step process: (1) the soft material is allowed to freely contract without any constraints, so its interfacial area is reduced (Fig. 2.8A). (2) The shrunken soft material is subjected to a bi-axial residual stress S_r so that its interfacial area is recovered, and then

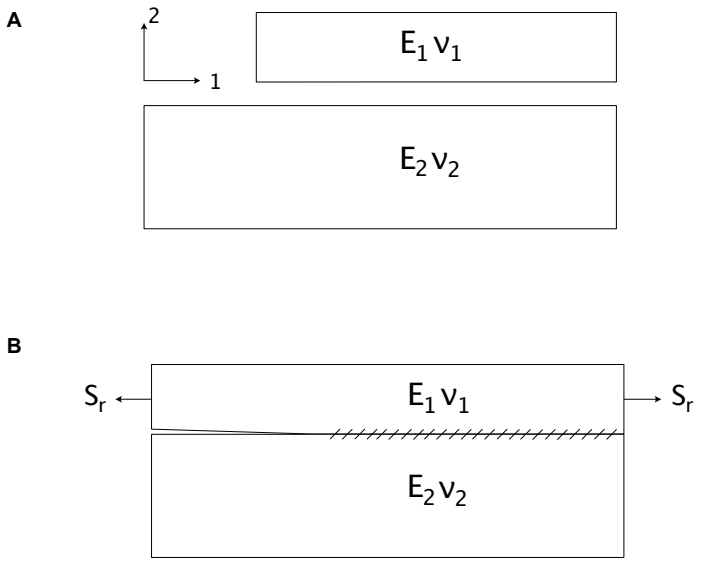

Fig. 2.8: An imaginary two-step process to estimate the residual stress S_r in a shrunken soft adhesive bonded to a substrate. (A) the adhesive is allowed to freely shrink without be constrained by the substrate. (B) the adhesive is subjected to stress that is equal to S_r to be stretched to the same interfacial area as the substrate, and then bonded to the substrate. (Note that S_r is nominal stress with respect to the undeformed configuration).

bonded to the substrate (Fig. 2.8B). Comparing Fig. 2.8B and 2.7A, we can write out the general loadings P_i and M_i in terms of the residual stress S_r:

$$\begin{aligned} P_1 &= -P_3 = S_r h_1 \\ M_1 &= M_2 = 0 \\ M_3 &= S_r h_1 \left(h_2 - \delta + \frac{h_1}{2} \right) \end{aligned} \tag{2.16}$$

The corresponding equivalent loadings P_e, M_e and M_e* can be written as:

$$\begin{aligned} P_e &= S_r h_1 \\ M_e &= 0 \\ M_e* &= S_r h_1^2 \end{aligned} \tag{2.17}$$

Substituting Eqn. (2.17) into Eqn. (2.14) yields the expression of G:

$$G = \frac{S_r^2 h}{8\mu} \tag{2.18}$$

The following task is to estimate the residual stress S_r in the soft adhesive. To do this, we

apply the imaginary two-step process illustrated in Fig. (2.8). The soft active material has an initial volume of V_0. In the first step, it shrinks its volume freely to the intermediate state with a new volume V_1. In the second step, the shrunken material is bi-axially stretched by λ in the plane parallel to the interface and fitted onto the substrate such that $\lambda = (V_0/V_1)^{1/3}$. During step 2, the volume of the soft active material is assumed to be preserved. The deformation gradient in step 2 reads

$$\mathbf{F} = \begin{bmatrix} \lambda & 0 & 0 \\ 0 & \lambda & 0 \\ 0 & 0 & 1/\lambda^2 \end{bmatrix} \tag{2.19}$$

We describe the mechanical behavior of the soft material by the Neo-Hookean model with shear modulus μ. The true stress in the material is given by:

$$\begin{aligned} \sigma &= \mu \left(\mathbf{F}\mathbf{F}^{\mathbf{T}} - \mathbf{I} \right) + p\mathbf{I} \\ &= \left[\mu(\lambda^2 - 1) + p \right] \mathbf{e_1} \otimes \mathbf{e_1} \\ &+ \left[\mu(\lambda^2 - 1) + p \right] \mathbf{e_2} \otimes \mathbf{e_2} \\ &+ \left[\mu(1/\lambda^4 - 1) + p \right] \mathbf{e_3} \otimes \mathbf{e_3}, \end{aligned} \tag{2.20}$$

where $\mathbf{e_i}$ $(i = 1, 2, 3)$ are the unit normal vectors. The hydrostatic pressure p can be calculated using the assumption that the material is stress free in direction 2: $\mu\,(1/\lambda^4 - 1) + p = 0$. Taken together, the true stress component in the bi-axial directions is given by:

$$\sigma_r = \mu \left(\lambda^2 - \frac{1}{\lambda^4} \right) \tag{2.21}$$

The nominal stress is related to the true stress by $S_r\lambda = \sigma_r$:

$$S_r = \mu \left(\lambda - \frac{1}{\lambda^5} \right) \tag{2.22}$$

Substituting Eqn. 2.22 into Eqn. 4.14 leads to

$$\begin{aligned} G &= \frac{Eh}{24} \Lambda \left(\bar{V} \right) \\ \text{with } \Lambda \left(\bar{V} \right) &= \left(\bar{V}^{1/3} - \bar{V}^{-5/3} \right)^2, \end{aligned} \tag{2.23}$$

where $\bar{V} = V_0/V_1$ is the relative volume shrinkage when the material is free of constraints

and $0 < \bar{V} \leq 1$. $\Lambda(\bar{V})$ measures the extent of the material's shrinkage when it is under the constraint of the interfacial adhesion. Fig. 2.9A plots the function $\Lambda(\bar{V})$ for blood clot (including platelet rich plasma (PRP) and whole blood [10, 12]), cells [15], and alginate/PNIPAm hydrogels [17, 47] based on their volume shrinkage reported in the literature. Their elastic moduli and characteristic sizes are plotted in Fig. 2.9B. It is important to note that we use the moduli of the cell cytoplasm, measured by microrheology, to represent their effective moduli due to the complex structures of cells [15]. For blood clots and alginate/PNIPAm hydrogels, their elastic moduli are measured by bulk measurement such as uniaxial tensile test or bulk rheology. With these properties, Eqn. 2.23 allows us to estimate the intrinsic driving forces for delamination for the three soft active materials (Fig. 2.9C).

Interestingly, G for cells are on the order of 10^{-5} Jm^{-2} predominantly due to their small sizes and low cytoplasmic moduli. Blood clot and alginate/PNIPAm wound dressing have similar values of G on the order of $1 \sim 10$ Jm^{-2}. It is important to note that the adhesion energy of blood clots are also on a similar level as G (based on unpublished data from our group). The results suggest that the contraction of blood clots can potentially impair their adhesion to tissues, which deserves a separate study. Other active materials with larger moduli than hydrogels such as liquid crystal elastomers [53] may exhibit G exceeding 10 Jm^{-2}, but their mechanical behaviors are often anisotropic due to the structure of the network. Such anisotropic contraction may lead to different G along different contraction directions, leading to different crack propagation paths. The current framework, which is tailored to active materials with isotropic volume shrinkage, is limited in its ability to accurately predict G for materials with such pronounced anisotropy. As a part of future research endeavors, extending the existing model to account for anisotropic deformations could hold promising potential, for example, by utilizing anisotropic consititutive models [54].

Finally, it is important to note that the adopted frame work [49] in driving Eqn. 2.23 is based on the linear elastic and small deformation assumptions, thereby Eqn. 2.23 only serves to provide a first-order approximation.

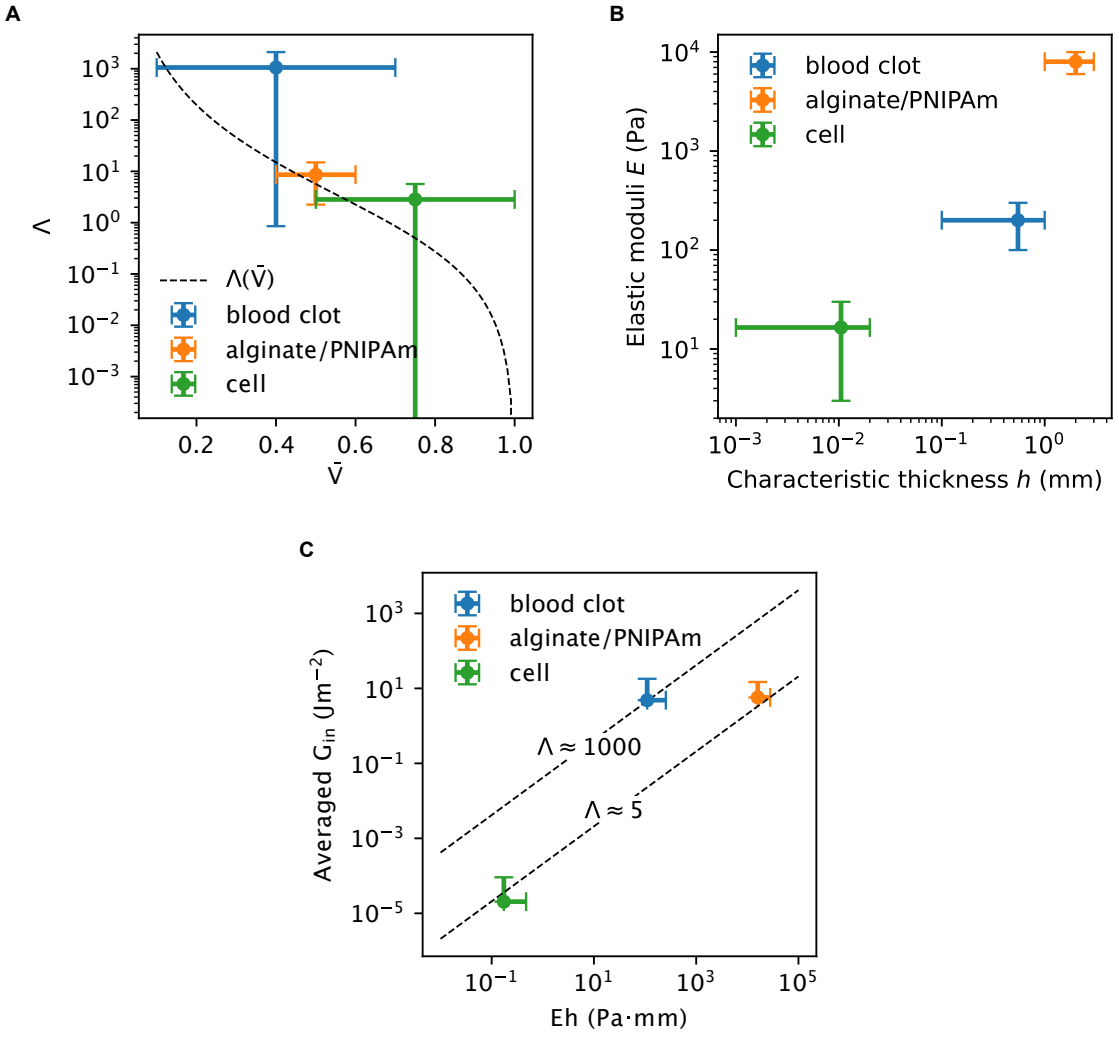

Fig. 2.9: (A) Function $\Lambda(\bar{V})$ versus volume shrinkage of blood clot [10, 12, 52], alginate/PNIPAm [17, 47], and cells [15]. (B) Their respective elastic moduli E and the characteristic length h. (C) Averaged intrinsic energy release rate for delamination G versus the ratio Eh. The top and bottom black dash lines correspond to $\Lambda \approx 1000$ and 5, respectively.

2.6 Nomenclature

G: intrinsic energy release rate

G_{ap}: applied energy release rate

G_{tot}: total energy release rate

G_c: adhesion energy

Γ: fracture energy

μ: shear modulus

E: elastic modulus

S_r: nominal residual stress

σ_r: true residual stress

P_i (i = 1,2,3): force per length

M_i (i = 1,2,3): moment per length

P_e and M_e: effective force per length and moment per length

Φ: strain energy density

$\bar{V}$: volume shrinkage

Bibliography

[1] Xinyue Liu, Ji Liu, Shaoting Lin, and Xuanhe Zhao. Hydrogel machines. *Materials Today*, 36:102–124, 2020.

[2] Emmanuel Siéfert, Etienne Reyssat, José Bico, and Benoît Roman. Bio-inspired pneumatic shape-morphing elastomers. *Nature Materials*, 18(1):24–28, 2019.

[3] Hyesung Cho, Gaoxiang Wu, Jason Christopher Jolly, Nicole Fortoul, Zhenping He, Yuchong Gao, Anand Jagota, and Shu Yang. Intrinsically reversible superglues via shape adaptation inspired by snail epiphragm. *Proceedings of the National Academy of Sciences*, 116(28):13774–13779, 2019.

[4] Jiawei Yang, Ruobing Bai, and Zhigang Suo. Topological adhesion of wet materials. *Advanced Materials*, 30(25):1800671, 2018.

[5] Xiaoyu Chen, Hyunwoo Yuk, Jingjing Wu, Christoph S Nabzdyk, and Xuanhe Zhao. Instant tough bioadhesive with triggerable benign detachment. *Proceedings of the National Academy of Sciences*, 117(27):15497–15503, 2020.

[6] Yang Gao, Kangling Wu, and Zhigang Suo. Photodetachable adhesion. *Advanced Materials*, 31(6):1806948, 2019.

[7] Zhenwei Ma, Claire Bourquard, Qiman Gao, Shuaibing Jiang, Tristan De Iure-Grimmel, Ran Huo, Xuan Li, Zixin He, Zhen Yang, Galen Yang, et al. Controlled tough bioadhesion mediated by ultrasound. *Science*, 377(6607):751–755, 2022.

[8] Jason Steck, Junsoo Kim, Jiawei Yang, Sammy Hassan, and Zhigang Suo. Topological adhesion. i. rapid and strong topohesives. *Extreme Mechanics Letters*, 39:100803, 2020.

[9] Jianyu Li, Adam D Celiz, Jiawei Yang, Quansan Yang, Isaac Wamala, William Whyte, Bo Ri Seo, Nikolay Vasilyev, Joost J Vlassak, and Mooney David J Suo, Zhigang. Tough adhesives for diverse wet surfaces. *Science*, 357(6349):378–381, 2017.

[10] Valerie Tutwiler, Hailong Wang, Rustem I Litvinov, John W Weisel, and Vivek B Shenoy. Interplay of platelet contractility and elasticity of fibrin/erythrocytes in blood clot retraction. *Biophysical Journal*, 112(4):714–723, 2017.

[11] Oleg V Kim, Rustem I Litvinov, Mark S Alber, and John W Weisel. Quantitative structural mechanobiology of platelet-driven blood clot contraction. *Nature Communications*, 8(1):1274, 2017.

[12] Yueyi Sun, David R Myers, Svetoslav V Nikolov, Oluwamayokun Oshinowo, John Baek, Samuel M Bowie, Tamara P Lambert, Eric Woods, Yumiko Sakurai, Wilbur A Lam, et al. Platelet heterogeneity enhances blood clot volumetric contraction: An example of asynchrono-mechanical amplification. *Biomaterials*, 274:120828, 2021.

[13] Karen YT Chan, Alyssa SM Yong, Xu Wang, Kristyn M Ringgold, Alexander E St. John, James R Baylis, Nathan J White, and Christian J Kastrup. The adhesion of clots in wounds contributes to hemostasis and can be enhanced by coagulation factor xiii. *Scientific Reports*, 10(1):20116, 2020.

[14] Shuaibing Jiang, Shiyu Liu, Sum Lau, and Jianyu Li. Hemostatic biomaterials to halt non-compressible hemorrhage. *Journal of Materials Chemistry B*, 10(37):7239–7259, 2022.

[15] Ming Guo, Adrian F Pegoraro, Angelo Mao, Enhua H Zhou, Praveen R Arany, Yulong Han, Dylan T Burnette, Mikkel H Jensen, Karen E Kasza, Jeffrey R Moore, et al. Cell volume change through water efflux impacts cell stiffness and stem cell fate. *Proceedings of the National Academy of Sciences*, 114(41):E8618–E8627, 2017.

[16] Yu Long Han, Pierre Ronceray, Guoqiang Xu, Andrea Malandrino, Roger D Kamm, Martin Lenz, Chase P Broedersz, and Ming Guo. Cell contraction induces long-ranged stress stiffening in the extracellular matrix. *Proceedings of the National Academy of Sciences*, 115(16):4075–4080, 2018.

[17] Serena Blacklow, Jianyu Li, Benjamin R Freedman, Mahdi Zeidi, Chen Chen, and David J Mooney. Bioinspired mechanically active adhesive dressings to accelerate wound closure. *Science Advances*, 5(7):eaaw3963, 2019.

[18] Michael Rubinsten. *Polymer Physics*. Oxford University Press, 2003. ISBN: 978-0198520597.

[19] Paul J Flory. *Principles of polymer chemistry*. Cornell university press, 1953. ISBN: 9780801401343.

[20] Youn Soo Kim, Mingjie Liu, Yasuhiro Ishida, Yasuo Ebina, Minoru Osada, Takayoshi Sasaki, Takaaki Hikima, Masaki Takata, and Takuzo Aida. Thermoresponsive actuation enabled by permittivity switching in an electrostatically anisotropic hydrogel. *Nature Materials*, 14(10):1002–1007, 2015.

[21] Hyunwoo Yuk, Shaoting Lin, Chu Ma, Mahdi Takaffoli, Nicolas X Fang, and Xuanhe Zhao. Hydraulic hydrogel actuators and robots optically and sonically camouflaged in water. *Nature Communications*, 8(1):14230, 2017.

[22] Eddie Wang, Malav S Desai, and Seung-Wuk Lee. Light-controlled graphene-elastin composite hydrogel actuators. *Nano letters*, 13(6):2826–2830, 2013.

[23] Chinatsu Azuma, Kazunori Yasuda, Yoshie Tanabe, Hiroko Taniguro, Fuminori Kanaya, Atsushi Nakayama, Yong Mei Chen, Jian Ping Gong, and Yoshihito Osada. Biodegradation of high-toughness double network hydrogels as potential materials for artificial cartilage. *Journal of Biomedical Materials Research Part A: An Official Journal of The Society for Biomaterials, The Japanese Society for Biomaterials, and The Australian Society for Biomaterials and the Korean Society for Biomaterials*, 81(2):373–380, 2007.

[24] Ankita Shastri, Lynn M McGregor, Ya Liu, Valerie Harris, Hanqing Nan, Maritza Mujica, Yolanda Vasquez, Amitabh Bhattacharya, Yongting Ma, Michael Aizenberg, et al. An aptamer-functionalized chemomechanically modulated biomolecule catch-and-release system. *Nature chemistry*, 7(5):447–454, 2015.

[25] Takashi Miyata, Noriko Asami, and Tadashi Uragami. A reversibly antigen-responsive hydrogel. *Nature*, 399(6738):766–769, 1999.

[26] Daehoon Han, Cindy Farino, Chen Yang, Tracy Scott, Daniel Browe, Wonjoon Choi, Joseph W Freeman, and Howon Lee. Soft robotic manipulation and locomotion with a 3d printed electroactive hydrogel. *ACS Applied Materials & Interfaces*, 10(21):17512–17518, 2018.

[27] Liang Dong, Abhishek K Agarwal, David J Beebe, and Hongrui Jiang. Adaptive liquid microlenses activated by stimuli-responsive hydrogels. *Nature*, 442(7102):551–554, 2006.

[28] Howard G Schild. Poly (n-isopropylacrylamide): experiment, theory and application. *Progress in polymer science*, 17(2):163–249, 1992.

[29] Ryo Yoshida, Katsumi Uchida, Yuzo Kaneko, Kiyotaka Sakai, Akihiko Kikuchi, Yasuhisa Sakurai, and Teruo Okano. Comb-type grafted hydrogels with rapid deswelling response to temperature changes. *Nature*, 374(6519):240–242, 1995.

[30] Ximin He, Michael Aizenberg, Olga Kuksenok, Lauren D Zarzar, Ankita Shastri, Anna C Balazs, and Joanna Aizenberg. Synthetic homeostatic materials with chemo-mechano-chemical self-regulation. *Nature*, 487(7406):214–218, 2012.

[31] Sabyasachi Rakshit, Yunxiang Zhang, Kristine Manibog, Omer Shafraz, and Sanjeevi Sivasankar. Ideal, catch, and slip bonds in cadherin adhesion. *Proceedings of the National Academy of Sciences*, 109(46):18815–18820, 2012.

[32] Valeri Barsegov and Devarajan Thirumalai. Dynamics of unbinding of cell adhesion molecules: transition from catch to slip bonds. *Proceedings of the National Academy of Sciences*, 102(6):1835–1839, 2005.

[33] Rodger P McEver and Cheng Zhu. Rolling cell adhesion. *Annual review of cell and developmental biology*, 26:363–396, 2010.

[34] George I Bell. Models for the specific adhesion of cells to cells: a theoretical framework for adhesion mediated by reversible bonds between cell surface molecules. *Science*, 200(4342):618–627, 1978.

[35] Manoj K Chaudhury. Rate-dependent fracture at adhesive interface. *The Journal of Physical Chemistry B*, 103(31):6562–6566, 1999.

[36] Tianhao Yang, Kenneth M Liechti, and Rui Huang. A multiscale cohesive zone model for rate-dependent fracture of interfaces. *Journal of the Mechanics and Physics of Solids*, 145:104142, 2020.

[37] Ilya V Pobelov, Kasper Primdal Lauritzen, Koji Yoshida, Anders Jensen, Gábor Mészáros, Karsten W Jacobsen, Mikkel Strange, Thomas Wandlowski, and Gemma C Solomon. Dynamic breaking of a single gold bond. *Nature Communications*, 8(1):15931, 2017.

[38] Cameron A Aubin, Benjamin Gorissen, Edoardo Milana, Philip R Buskohl, Nathan Lazarus, Geoffrey A Slipher, Christoph Keplinger, Josh Bongard, Fumiya Iida, Jennifer A Lewis, et al. Towards enduring autonomous robots via embodied energy. *Nature*, 602(7897):393–402, 2022.

[39] Pierre-Giles De Gennes. Reptation of a polymer chain in the presence of fixed obstacles. *The Journal of Chemical Physics*, 55(2):572–579, 1971.

[40] Samuel Frederick Edwards. Statistical mechanics with topological constraints: I. *Proceedings of the Physical Society*, 91(3):513, 1967.

[41] Michael Rubinstein and Sergei Panyukov. Elasticity of polymer networks. *Macromolecules*, 35(17):6670–6686, 2002.

[42] Junsoo Kim, Guogao Zhang, Meixuanzi Shi, and Zhigang Suo. Fracture, fatigue, and friction of polymers in which entanglements greatly outnumber cross-links. *Science*, 374(6564):212–216, 2021.

[43] Chenghai Li, Zhijian Wang, Yang Wang, Qiguang He, Rong Long, and Shengqiang Cai. Effects of network structures on the fracture of hydrogel. *Extreme Mechanics Letters*, 49:101495, 2021.

[44] Graham J Lake and Allen G Thomas. The Strength of Highly Elastic Materials. *Proceedings of the Royal Society of London Series A*, 300(1460):108–119, August 1967.

[45] Teng Zhang, Shaoting Lin, Hyunwoo Yuk, and Xuanhe Zhao. Predicting fracture energies and crack-tip fields of soft tough materials. *Extreme Mechanics Letters*, 4:1–8, 2015.

[46] Jeong-Yun Sun, Xuanhe Zhao, Widusha RK Illeperuma, Ovijit Chaudhuri, Kyu Hwan Oh, David J Mooney, Joost J Vlassak, and Zhigang Suo. Highly stretchable and tough hydrogels. *Nature*, 489(7414):133–136, 2012.

[47] Zhen Yang, Xingwei Yang, Rong Long, and Jianyu Li. Stimulation modulates adhesion and mechanics of hydrogel adhesives. *Langmuir*, 37(23):7097–7106, 2021.

[48] Dhananjay T Tambe, C Corey Hardin, Thomas E Angelini, Kavitha Rajendran, Chan Young Park, Xavier Serra-Picamal, Enhua H Zhou, Muhammad H Zaman, James P Butler, David A Weitz, et al. Collective cell guidance by cooperative intercellular forces. *Nature Materials*, 10(6):469–475, 2011.

[49] Zhigang Suo and John W Hutchinson. Interface crack between two elastic layers. *International Journal of Fracture*, 43(1):1–18, 1990.

[50] John W Hutchinson and Zhigang Suo. Mixed mode cracking in layered materials. *Advances in applied mechanics*, 29:63–191, 1991.

[51] John Dundurs et al. Mathematical theory of dislocations. *American Society of Mechanical Engineers, New York*, pages 70–115, 1969.

[52] Shiyu Liu, Guangyu Bao, Zhenwei Ma, Christian J Kastrup, and Jianyu Li. Fracture mechanics of blood clots: measurements of toughness and critical length scales. *Extreme Mechanics Letters*, 48:101444, 2021.

[53] Jiaxi Cui, Dirk-Michael Drotlef, Iñigo Larraza, Juan P Fernández-Blázquez, Luciano F Boesel, Christian Ohm, Markus Mezger, Rudolf Zentel, and Aránzazu del Campo. Bioinspired actuated adhesive patterns of liquid crystalline elastomers. *Advanced Materials*, 24(34):4601–4604, 2012.

[54] Qiguang He, Yue Zheng, Zhijian Wang, Xuming He, and Shengqiang Cai. Anomalous inflation of a nematic balloon. *Journal of the Mechanics and Physics of Solids*, 142:104013, 2020.

Chapter 3

Stimulation regulates adhesion and mechanics of adhesive hydrogels

This chapter is based on journal publication [J1]. Reprinted with permission from [1].

abstract

The ability to modulate the adhesion of soft materials on-demand is desired for broad applications ranging from tissue repair to soft robotics. Research effort has been focused on the chemistry and architecture of interfaces, leaving the mechanics of soft adhesives overlooked. Stimuli-responsive mechanisms of smart hydrogels could be leveraged for achieving stimuli-responsive hydrogel adhesives that respond mechanically to external stimuli. Such stimuli-responsive hydrogel adhesives involve complex chemomechanical coupling and interfacial fracture phenomena, calling for mechanistic understanding to enable rational design. Here, we combine experimental, computational, and analytical approaches to study a thermo-responsive hydrogel adhesive. Experimentally, we show that the adhesion and mechanical properties of a stimuli-responsive hydrogel adhesive are both enhanced by the application of a stimulus. Our analysis further reveals that the enhanced adhesion stems from the increased fracture energy of the bulk hydrogel and the insignificant residual stress on the adhesive-tissue interface. This study presents a framework for designing stimuli-responsive hydrogel adhesives based on the modulation of bulk properties and sheds light on the development of smart adhesives with tunable mechanics.

3.1 Introduction

Adhesive materials find significant use in engineering and medicine [2, 3, 4]. They can be categorized into two classes: mechanically passive adhesives that are designed to maintain their structural and mechanical properties after placement, and switchable adhesives that allow for on-demand modulation of their bonding state and mechanical properties [5]. The former include pressure sensitive adhesives (PSAs), cyanoacrylate (super glue), and epoxy, which are commonly used in daily life [6]. The latter is exemplified with the Command Strip (3M Company) that can attach/detach under different loading conditions, as well as thermomorphic PSAs that can reshape upon the temperature change [7]. Other switchable adhesives that can detach upon exposure of chemical, physical or mechanical stimuli [8, 9, 10, 11, 12, 13, 14] are under development. Recent efforts have been focused on interfacial mechanisms, such as chemical reactions and wrinkling, confined between the adhesive and the adherend. A knowledge gap exists for methodologies to enable on-demand and predictive modulation of

both the interfacial and bulk properties of the adhesive. This ability is desired for broad applications, ranging from tissue repair, regenerative medicine to soft robotics [3, 15, 16].

Stimuli-responsive hydrogels are appealing for the development of switchable adhesives. They are also known as smart hydrogels, whose network can be regulated by chemical (ions, pH, proteins) or physical (temperature, light, electrical or magnetic fields) cues [17, 18]. The molecular-level regulation results in configurational transition of the hydrogel, as well as its mechanical properties. These hydrogels feature tunable mechanical properties, dramatic volumetric change, and biocompatibility [19]. They are well poised for drug delivery, actuators and soft robotics [20]. Recently, a thermo-responsive PNIPAm-based hydrogel was engineered into active wound dressings, which can adhere strongly to tissues and contract the edge of a wound in response to skin temperature, demonstrating accelerated wound closure *in vitro* and *in vivo* [21]. However, little is known about the effects of stimulation on the mechanical properties of the hydrogel adhesive. The interplay between the stimuli-responsive mechanism and the performance of the adhesive remains elusive and calls for further investigation.

Here we report a design of switchable adhesive, named as smart adhesive, based on stimuli-responsive mechanisms of smart hydrogels. The stimulation applied externally could elicit phase transition and contraction of the adhesive matrix, thus modulating the bonding state and bulk properties of the adhesive. Specifically, together with the mechanical constraint by the adherend, the contraction could raise residual stress in the adhesive matrix, which yields an energy release rate G for an initial crack on the interface. We hypothesize that when G exceeds the adhesion energy G_c, the adhesive would debond, otherwise the mechanical properties of the adhesive such as stiffness and toughness could be modulated (Fig 3.1). To demonstrate the design principle of stimuli-responsive hydrogel adhesives, we use a thermo-responsive adhesive consisting of a PNIPAm/alginate double network hydrogel as a model system, hereafter referred to as the dually cross-linked (DC) hydrogel since both networks are crosslinked. This system can form strong tissue adhesion [22, 23], expel water and shrink at around 32°C [24] due to PNIPAm.

To test our hypothesis, we combine experimental, theoretical, and computational approaches to study the stimuli-responsive behavior of the smart adhesive. We first characterize the mechanical properties of the smart adhesive before and after stimulation, demonstrating its responsiveness to temperature. We develop a finite element (FE) model to simulate the smart adhesive attached on a rigid substrate upon stimulation. By leveraging the FE model and an analytical model, we then evaluate quantitatively the effects of stimulation on the interfacial fracture process. We find a good agreement among experiments, FE simulations and analytical estimations. This work presents a comprehensive

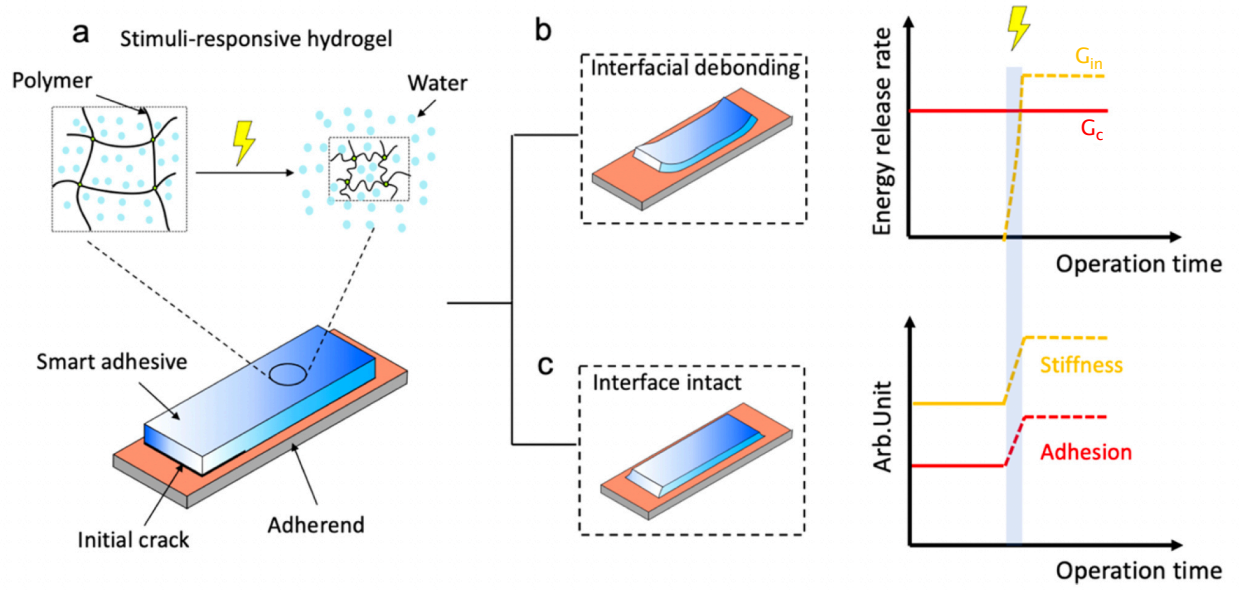

Fig. 3.1: Schematics of design and proposed responses of stimuli-responsive hydrogel adhesives adaptive to external stimulation. (a) A stimuli-responsive hydrogel adhesive is attached to an adherend, with an initial crack introduced at the interface and adhesion energy Γ_a. The adhesive matrix repels water and contracts upon stimulation. The stimuli-triggered contraction induces residual stress in the bulk hydrogel, yielding intrinsic energy release rate G_{in} to drive the interfacial crack. (b) The interface debonds when G_{in} is greater than the interfacial adhesion energy Γ_a. (c) The interface stays intact when G_{in} is smaller than Γ_a, and the adhesive hydrogel exhibits enhanced mechanical properties such as stiffness and adhesion energy.

framework and valuable insights for designing smart adhesives and is expected to motivate the development of future adhesives with unprecedented properties. The rest of the paper is organized as follows. Section 3.2 describes the theoretical basis to model the stimulation of PNIPAm, including a free energy function and a procedure to characterize it for the PNIPAm-alginate hydrogel. Section 3.3 presents experimental details. Section 3.4 presents the experimental, analytical, and computational results. Finally, conclusions are made in Section 3.5.

3.2 Theoretical section

3.2.1 Free energy function

Following previous studies [25, 26, 27], we assume the Helmholtz free energy of the hydrogel matrix of the smart adhesive to be the total free energy due to mixing of the polymer and the solvent (W_{mix}) and stretching of the network (W_{stretch}):

$$W = W_{\text{stretch}} + W_{\text{mix}} \tag{3.1}$$

This assumption is also known as the Flory-Rehner model. The free energy due to stretching of the polymer chains is assumed to follow the Gaussian-chain model [28]:

$$W_{\text{stretch}} = \frac{1}{2}NkT\left[\lambda_1^2 + \lambda_2^2 + \lambda_3^2 - 3 - 2\log(\lambda_1\lambda_2\lambda_3)\right] \tag{3.2}$$

where N is the nominal chain density; λ_1, λ_2, and λ_3 are the principle stretches. The free energy due to mixing is formulated based on the Flory−Huggins model [29, 30]:

$$W_{\text{mix}} = kT\left[C\log\frac{\Omega C}{1+\Omega} + \frac{\chi C}{1+\Omega C}\right] \tag{3.3}$$

where k is the Boltzmann constant, T is the absolute temperature, Ω is the volume of a water molecule, C is the nominal number of water molecules per unit volume, and χ is the Flory interaction parameter.

From Eqn(3.1)-(3.3), the hydrogel network can be fully characterized once the Flory interaction parameter χ is temperature-dependent and is assumed to follow the form below [31]:

$$\chi(T,\phi) = \chi_0 + \chi_1\phi, \tag{3.4}$$

where $\chi_0 = A_0 + B_0T$, $\chi_1 = A_1 + B_1T$, and $\phi = 1/(1 + \Omega C)$ are the volume fractions of the polymer in the hydrogel. Due to the presence of alginate, the four coefficients (A_0, B_0, A_1, and B_1) for the PNIPAm-alginate hydrogel are expected to differ from those measured with the PNIPAm hydrogel, which are to be determined in the following experiment.

3.2.2 Determination of the Flory Interaction Parameter

In the Flory-Rehner theory, the nominal chain density N is related to the shear modulus μ by

$$\mu = \frac{NkT}{J^{1/3}} = NkT\phi^{1/3}, \tag{3.5}$$

where $J = \phi^{-1}$ is the equilibrium swelling ratio. The shear modulus can be measured using various methods such as rheological [32] or tensile [33] tests. The Flory interaction parameter χ can be obtained by fitting the equations of states for ideal elastomeric gels [34]. The equation of states of the elastomeric gel is given by

$$\sigma_i = \frac{\partial W_{\text{stretch}}(\lambda_i, \lambda_j, \lambda_k)}{\lambda_j \lambda_k \partial \lambda_i} + \frac{dW_{\text{mix}(J)}}{dJ} - \frac{\psi}{\Omega}, \tag{3.6}$$

where σ_i is the true stress, ψ is the chemical potential of the solvent in the reservoir, and i, j, and k are the permutation notations which can take on 1, 2, and 3. Note that repeated indices do not imply summation (i.e., the summation convention is not adopted here. By substituting Eqns.(3.2) (3.3) into Eqn (3.6), we obtain the condition for the hydrogel to reach the swollen equilibrium at a specified temperature T, which together with the stress-free condition under free swelling yields a fitting function

$$\frac{NkT}{J}(\lambda_f^2 - 1) + \frac{kT}{\Omega}\left[\log\left(1 - \frac{1}{J}\right) + \frac{1}{J} + \frac{\chi_0 - \chi_1}{J^2} + 2\frac{\chi_1}{J^3}\right] - \frac{\psi}{\Omega} = 0, \tag{3.7}$$

where $\lambda_f = J^{1/3}$. This equation can be characterized as follows. A hydrogel is submerged in a aqueous solution and swells to equilibrium at a certain temperature. The equilibrium swelling ratio J and the corresponding temperature T are recorded. Repeating the procedure for the same type of hydrogel under different temperatures enables the establishment of Eqn (3.7), from which the Flory interaction parameter χ can be fitted.

It needs to be pointed out that the direct characterization of χ for the PNIPAm-alginate DC hydrogel is complicated by the fact that the ionic crosslinker of the alginate network, Ca^{2+}, can migrate out from the DC hydrogel during swelling, thereby altering the cross-linking density of the hydrogel. To bypass the confounding effect, we adopted an alternative strategy

by testing the PNIPAm-alginate hydrogel without Ca^{2+} crosslinkers, denoted as the singly crosslinked (SC) hydrogel. Furthermore, we submerged the SC hydrogels in an alginate solution of the same polymer content to equate the chemical potential of water in the hydrogel and in the solution, such that ψ vanishes in Eqn (3.7).

3.3 Experimental section

3.3.1 Adhesion Energy Measurement

We adhered the adhesive onto the model tissue and divided the samples into two groups. The first group was kept at room temperature before testing. The other group were stimulated at 37 °C for 3 hrs and then returned to room temperature, with the surface water removed by tissue paper. Before the adhesion measurement, a PET film was glued onto the back of the hydrogel to constrain the deformation. The model tissue was clamped onto a sliding tray and the hydrogel adhesive was peeled off using a universal testing machine (model 5965; Instron, Norwood, MA, USA). During the peeling process, the angle between the adhesive and the tissue substrate was fixed at 90°, and the loading rate was maintained at 0.5 mm·s^{-1}. The force and the displacement were recorded.

3.3.2 Free Swelling Test

The SC hydrogel samples (10 × 10 × 10 mm^3) were submerged in 2% w/v alginate solution at different temperatures for 1 week such that the hydrogels had sufficient time to reach equilibrium swelling. The samples were then taken out from the solution and blotted with tissue paper to remove the excessive liquid on the surface and were weighed immediately using an analytical scale at room temperature to determine the mass m_{gel}. After that, the samples were transferred to a freeze dryer (FreeZone 2.5 L; Labconco, Kansas, MO, USA) for complete dehydration for 5 days, after which they were weighted again to determine the mass of the dry polymer m_{dry}. The free swelling ratio was calculated using the gravimetric method: $(m_{\text{gel}} - m_{\text{dry}})/\rho_{\text{polymer}}/m_{\text{dry}} + 1$, where we have used $\rho_{\text{water}} = 1$ g/cm^3; the weighted average density of the two polymers within the hydrogel is $\rho_{\text{polymer}} = 1.05$ g/cm^3.

3.3.3 Fracture Energy Measurement

The fracture energy of the DC hydrogel was measured using a pure shear test (Section 2.4.3). Two samples were tested with one sample containing a notch and the other not. In the

un-deformed configuration, the hydrogel under room temperature had a width of $w = 80$ mm, thickness of $t = 1.5$ mm, and height of $h = 6$ mm (the distance between two clamps). In the notched sample, an initial crack of length 30 mm was introduced by a razor blade, and the sample was pulled until rupture to record the critical stretch ratio λ_c. The unnotched sample was pulled to the same stretch ratio λ_c. The force and displacement were recorded. The fracture energy of pure shear specimen can be calculated as:

$$\Gamma = W(\lambda_c)h \tag{3.8}$$

where $W(\lambda_c)$ is the strain energy stored in the unnotched sample subjected to stretch λ_c and can be evaluated by the area underneath the nominal stress-stretch curve up to λ_c.

3.3.4 Rheological Measurements

The complex shear modulus of the SC hydrogel was measured using a rheometer (TA Instruments). Cylindrical samples, 5mm in diameter and 2 mm in thickness, were subjected to a constant shear strain of 1% with the angular frequency ramping from 0.5 to 0.05 rad/s.

3.4 Results and Discussion

3.4.1 Modulating Adhesion via Stimulation.

The adhesion between the hydrogel adhesive and the model tissue involves two mechanisms: (i) the interfacial bonding and (ii) the bulk energy dissipation in the hydrogel. The first part is due to the interfacial bridging network (chitosan) formed *in situ*, with its one end in topological entanglement with the hydrogel network and the other end anchored on the tissue surface via covalent bonding and physical interpenetration [23] (Fig S13). To drive an interfacial crack, either the hydrogel network or the stitching network needs to break. Then, the force needed to break the bridging network is transmitted into the bulk hydrogel, leading to the breakage of sacrificial bonds (the ionically cross-linked alginate hydrogel) and consequently substantial bulk energy dissipation [23, 35]. The effects of stimulation are expected to be twofold: the stimuli-triggered transition could alter the bulk properties of the adhesive while resulting in a residual stress and an intrinsic energy release rate to drive the interfacial crack, which offsets the adhesion energy of the stimuli-responsive adhesive. We first demonstrated the stimulation could trigger debonding of the stimuli-responsive adhesive. Given the absence of covalent bonding on the interface and a low adhesion energy G_c, the

adhesive hydrogel came off the tissue substrate after phase transition at 37°C, leaving behind an observable thin layer of water on the interface. The result supports our hypothesis shown in Fig 3.1b that the interface debonds when the stimulation-triggered G exceeds G_c.

We then hypothesized that the debonding could be arrested when G_c is sufficiently large and that the post-stimulation (PS) adhesive is expected to exhibit higher stiffness and adhesion (Fig 3.1c). To test the hypothesis, we characterized the adhesion property of the stimuli-responsive adhesives before and after stimulation when introducing covalent bonding to the interface. We observed that the stimuli-responsive adhesive applied on the tissue substrate experienced large volume changes (∼50% volume reduction, see Fig S2). After returning to room temperature, the volume reduction due to stimulation was retained since the sample accessed no additional solvent. Notably, in the presence of a relatively weak interfacial adhesion (corresponding to 2% w/v coupling reagents in the topohesive), localized debonding was observed near the edge of the interface (Fig S3). When a strong interfacial adhesion is present (e.g., 6% w/v coupling reagents in the topohesive), such localized debonding was not observed.

We conducted the 90° peeling test to measure the initial and the PS adhesion energies (Fig 3.2a). Fig 3.2b shows two representative force-displacement curves with the topohesive containing 6% w/v coupling reagents. The initial portion of the two curves fall together, but their plateaus values deviate from each other, with the peel force in the PS state being considerably higher. The adhesion energies with different concentrations of topohesives are calculated via [36]

$$G_c = F_p/w \tag{3.9}$$

where F_p is the plateau peeling force and w the width of the adhesion region. Note that the width of the contact surface decreased slightly (∼ 14.7 and 14 mm with 6 and 0% w/v reagents, respectively) compared to the initial value (∼ 15 mm). Fig 3.2c shows that the PS adhesion energy is higher than the initial counterpart under all the tested conditions. For example, the averaged PS adhesion energies are 540 and 40 Jm^{-2} at 6 and 2% w/v of coupling reagents, respectively. They are higher than the initial values, 280 and 28 Jm^{-2}, with the same concentrations of coupling reagent. Note that the initial adhesion energy with 0% w/v reagents is too low to be measured by the peeling test and hence not shown in the Figure. These results demonstrate that in the presence of high initial adhesion energy mediated by coupling reagents, the adhesion is retained and even becomes stronger after stimulation despite the significant deformation and possible localized debonding near the edges of the interface (Figs S2 and S3). To the best of our knowledge, this is the first observation of hydrogel adhesion toughening by a stimuli-responsive mechanism. Furthermore, the adhesive

is expected to restore its initial state under room temperature with the presence of sufficient water supply, for example, in a humid ambient. Thus, the enhanced adhesion in the PS state can be suppressed for reciprocating smart adhesion.

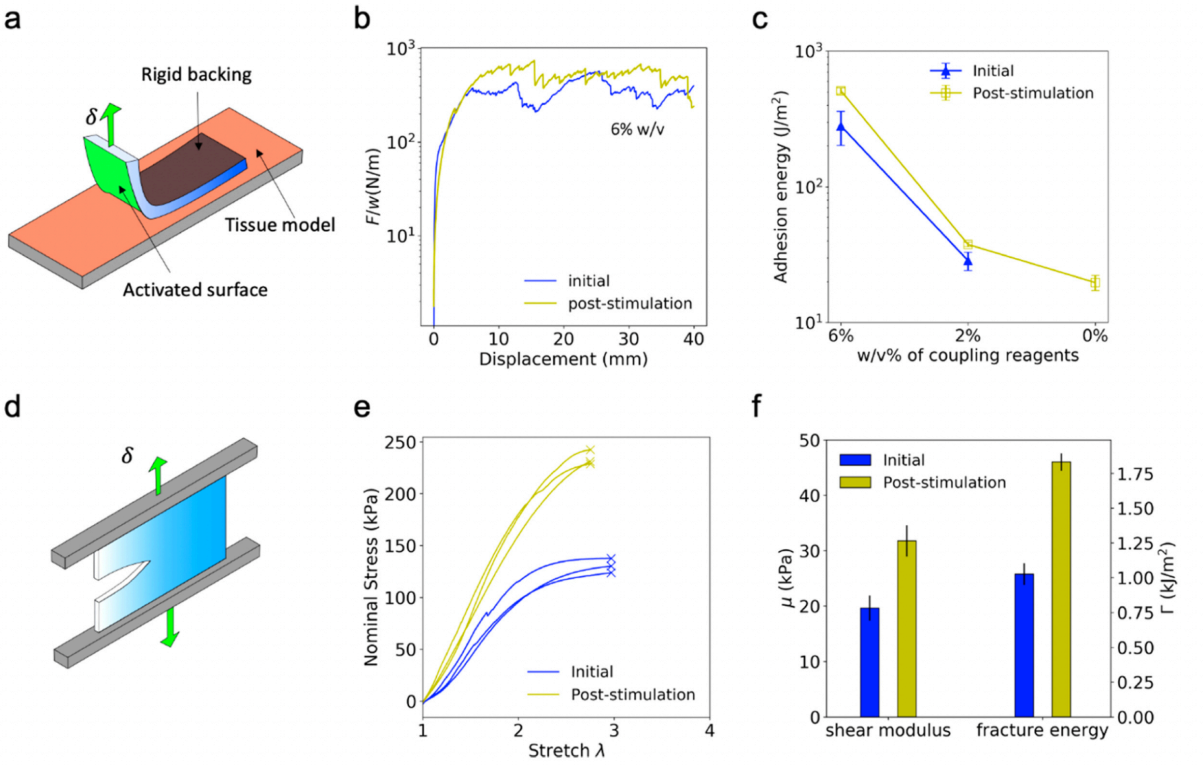

Fig. 3.2: Adhesion and fracture energy measurements (a-c) adhesion energy measurement. (a) Schematic of the 90° peeling test. (b) Representative curves of force/width vs displacement with topohesives containing 6% w/v reagents. (c) Initial and PS adhesion energies with topohesives containing different concentrations of the coupling reagents. (d-f) Fracture energy measurement. (d) Schematic of the pure shear test with a notched specimen. (e) Representative nominal stress-displacement curves for the unnotched specimens. The critical stretch corresponding to the onset of the crack propagation in the notched sample is marked using × marker. (f) Initial and PS shear modulus μ and fracture energy Γ for the alginate/PNIPAm DC hydrogel. Sample size n=3.

It should be noted that the PS adhesion energy measured above might differ from the exact value corresponding to the interface between the stimulated adhesive and the substrate. The difference is attributed to the residual stress created by stimulation, which results in an energy release rate G for the edge crack (Fig 3.1) that tends to decrease the peel force and thus the measured adhesion energy. From a molecular perspective, this can be understood as the contraction of the bulk hydrogel matrix induced by stimulation stretches the stitching network, thus generating a pre-strain in it. As a result, the peel force required to drive the edge crack is reduced. The enhanced adhesion in the PS state indicates that G did not

exceed the interfacial adhesion energy because otherwise debonding would have occurred after stimulation. Nevertheless, the energy release rate G due to residual stress acts to offset the PS adhesion energy and thus needs to be quantified. It will be studied with analytical and computational models to be shown later. In addition, the formation of interfacial water released from the adhesive matrix in the presence of low initial adhesion affects the PS adhesion, which will be further explored in a separate study.

3.4.2 Modulating Mechanical Properties via Stimulation.

To delineate the effect of stimulation on the bulk properties of the stimuli-responsive adhesive, we next characterize the shear modulus and the fracture energy of the adhesive hydrogel before and after stimulation using the pure shear test (Fig 3.2d). Fig 3.2e shows that the nominal stress-stretch curve for the unnotched PS specimen exhibits a larger initial slope and higher strength but a slightly lower stretchability. The measured shear modulus and the fracture energy are plotted in Fig 3.2f. The initial shear modulus of the hydrogel is $\mu_{\text{initial}} = 19$ kPa and increases to $\mu_{\text{PS}} = 30$ kPa after stimulation (Fig S4a,b). The stiffening effect is attributed to the increased polymer content of the shrunken hydrogel, as indicated by Eqn 3.5. Note that the scaling relationship ($\mu \propto \phi^{1/3}$) is applicable to hydrogels which were prepared in their dry state and stressed upon swelling [37, 38]. In our case, however, the hydrogels were formed in the solution and hence stressed in the dry state. In addition, there are also cases where the shear modulus of the hydrogel does not scale with ϕ upon the exponent 1/3 depending on the properties of the precursor solution and of the state of observation [39, 40], but all showing the positive correlation between μ and ϕ.

As well, we observed a considerable increase in the fracture energy in the PS state. This positive correlation between the fracture energy and the polymer content can be interpreted with the Lake-Thomas theory [41]. A detailed comparison is not pursued here as the DC hydrogel features substantial amount of bulk dissipation that dominates the fracture energy, which is not considered in the Lake-Thomas theory. Along with the measured adhesion energy, all the measured quantities of the adhesive are raised by the stimulation. Interestingly, we found they followed a similar scaling relation with respect to the swelling ratio J (Fig S4c). The observations coincide with a recent work in our group [42]. In particular, we showed that a double network alginate/PAAm hydrogel exhibits a universal negative scaling relation of shear modulus, adhesion energy, and fracture energy as a function of the swelling ratio. The phenomenon was attributed to the unique double-network structure, in which the bulk dissipation dominates both the adhesion and fracture energies. Taken together, our results demonstrate that the stimulation allows for on-demand enhancement of the adhesion and

mechanical properties of stimuli-responsive hydrogels.

3.4.3 Analytical Estimation of the Energy Release Rate G.

The problem analyzed here is illustrated in Fig 3.3. The two materials are assumed to be isotropic and elastic. The upper part represents the hydrogel adhesive with shear modulus μ and initial thickness h_1, while the lower one represents the model tissue with initial thickness h_2. The model tissue is much stiffer than the hydrogel adhesive and is hence approximated to be rigid in this analysis. We assume $h_1 = h_2$ based on the dimensions of the specimen in the experiment. The bi-material specimen is subjected to combined loadings and moments P_i and M_i (i = 1, 2, 3) (Fig 2.7).

Following Suo and Hutchinson [43] the general loadings and moments applied to the bi-material specimen are first converted to the equivalent loading and moment P_r and M_r (Fig 3.3a). Upon stimulation, the hydrogel adhesive undergoes phase transition and shrinks. An analogy can be drawn from the shrunken adhesive to a residually stressed one, such that $M_r = 0$ and $P_r = S_r h_1$, with S_r being the residual stress. By taking the difference between the energies stored far ahead of and far behind the crack tip, the strain energy release rate G is given by (Section 2.5)

$$G = \frac{S_r^2 h_1}{8\mu} \tag{3.10}$$

Eqn 3.10 reveals that G is quadratic in S_r (Fig 3.3b) and the task to estimate G has become how to estimate the residual stress S_r in the hydrogel adhesive due to the shrinkage. S_r is estimated to be 33 kPa for the adhesive hydrogel during the phase transition (Supporting Information); thus the strain energy release rate G due to the residual stress in the PS state is $G(S_r = 33\text{kPa}) = 6.6$ J/m^2. This value is much smaller than the measured adhesion energies with topohesives containing 6 and 2% w/v coupling reagents (Fig 3.1e). Importantly, it needs to be pointed out that Eqn 3.10 is only valid for small deformation, so it only gives a first-order approximation. Provided that the hydrogel adhesive undergoes large deformation during the phase transition (Fig S2), a more accurate estimation of G_{in} demands the implementation of FE modelling. We next perform experiments to characterize the thermodynamic properties of the adhesive matrix in pursuit of FE modelling.

3.4.4 Characterization of Stimuli-Responsive Behavior.

The free energy function of the adhesive matrix was characterized with rheological and free swelling tests. We focus on the SC hydrogel, which was composed of a covalently cross-linked

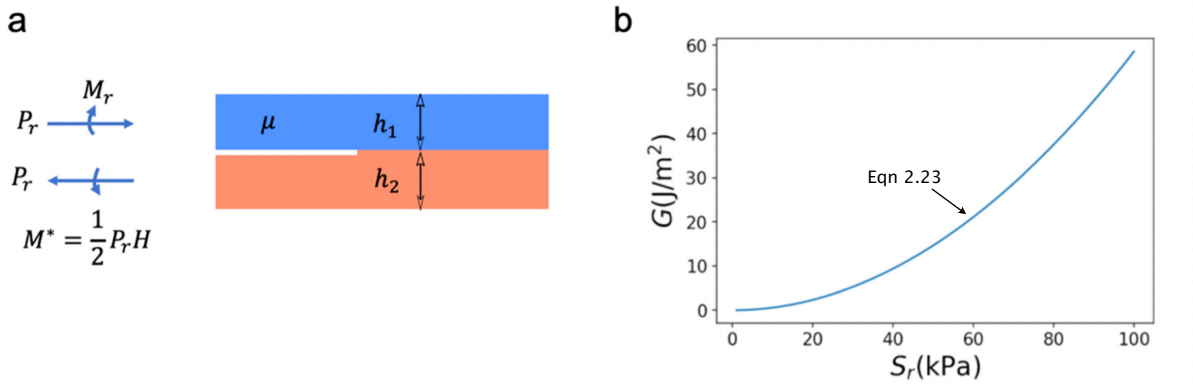

Fig. 3.3: Analytical estimation of the strain energy release rate G on the hydrogel-tissue interface. (a) Schematics of an interfacial crack embedded in a bi-material specimen subjected to the general and equivalent loadings. (b) Strain energy release rate G plotted against the residual stress in the hydrogel for $h_1 = h_2 = 1.5$ mm.

PNIPAm network but un-crosslinked alginate chains of the same polymer content as the filler (Fig 3.4a). The SC hydrogel swells freely in the alginate solution till equilibrium (Fig 3.4b). Based on the postulation in the Flory-Huggins theory that the free energy due to mixing is independent of the crosslink density, it is reasonable to assume that χ for the SC hydrogel is the same to that of the DC hydrogel. As such, we can avoid the complication of ion exchange of the DC hydrogel during the swelling. Fig 3.4c illustrates the storage and the loss shear modulus μ' and μ'' of the SC hydrogel measured using a rheometer. The storage modulus μ' decreases monotonically with the frequency, and the low-frequency storage modulus linked with the crosslink density was estimated by linearly extrapolating the last three data points in the range of 0.05-0.13 rad/s. Besides, since μ' is approximately 8 times larger than μ'' across the whole test frequency, we approximate the complex shear modulus with the storage modulus $\mu = \mu' = 171$ Pa. Using Eqn 3.5, the dimensionless chain density of the SC hydrogel is determined, $N\Omega = 3.9 \times 10^{-6}$.

To establish Eqn 3.7, we measured the equilibrium swelling ratio J for the SC hydrogel using free swelling tests at different temperatures. Fig 3.4d shows that the $J = 25$ initially for the swollen equilibrium SC hydrogel under room temperature, which then drastically decreases with increasing temperature and eventually approaches 2 in the high temperature range. This is clearly different from the pure PNIPAm hydrogel, which approaches a swelling ratio of 1 at elevated temperatures. The difference is attributed to the presence of the hydrophilic alginate polymer in the hydrogel.

As well, we measured the swelling ratio J for the as-prepared DC hydrogels in the initial and the PS states, which are also plotted for comparison. Note that the as-prepared DC hydrogel

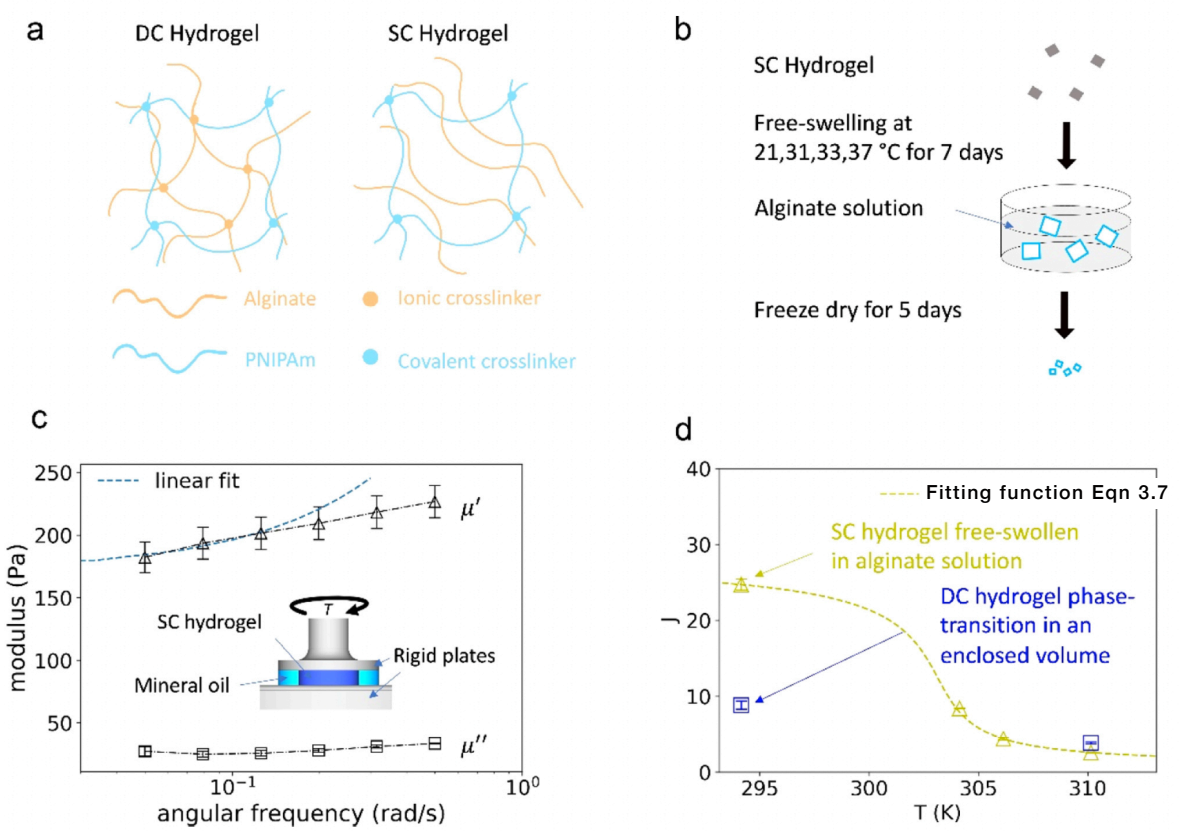

Fig. 3.4: Rheological and swelling measurements. (a) Schematics of PNIPAm-alginate hydrogels with both covalent and ionic cross-links (DC hydrogel) and with covalent crosslinks solely (SC hydrogel). (b) Schematic of the free swelling test using the SC hydrogel. (c) Complex modulus of the alginate/PNIPAm SC hydrogel measured using a rheometer. (d) Equilibrium swelling ratio J for the SC hydrogel at different temperatures (yellow). The swelling ratio of the as-prepared DC hydrogel is also plotted at 294 and 310 K (blue).

adhesive is not in the swollen-equilibrium state. Different from the swelling test, the DC hydrogel in the PS state is obtained by phase transition in an enclosed bag to avoid dehydration. The J value in the initial state for the as-prepared DC hydrogel is 8.8, which is considerably smaller than the equilibrium J value for the SC hydrogel due to the higher crosslink density. The J value in the PS state is comparable with the equilibrium J value for the SC hydrogel. Lastly, we plugged the measured dimensionless chain density $N\Omega$ into the fitting function (Eqn 3.7) to fit the equilibrium swelling ratio J for the SC hydrogel. As can be seen, the fitted curve agrees well with the experimental results (Fig 3.4d). The fitted χ is defined with the following parameters: $A_0 = -1.95, B_0 = 0.00868K^{-1}, A_1 = -2.64, B_1 = 0.00929K^{-1}$. These efforts lead to the establishment of a free energy function of the stimuli-responsive hydrogel adhesive matrix, which will be utilized in the FE simulation later.

3.4.5 FE Simulation of the Stimuli-Responsive Hydrogel Adhesive.

We conduct FE simulations with a commercial package Abaqus (2020, Simulia). The Flory-Rhener free energy function (Eqn 3.1) is implemented in the FE model using a user-defined subroutine for hyperelastic materials (UHYPER). To validate the UHYPER subroutine, a free swelling test is performed for the DC and the SC hydrogels. Briefly, a cubic block of a hydrogel, $8 \times 8 \times 8$ mm^3 in size, is subjected to a temperature increase from 294 to 320 K. The equilibrium swelling ratio J calculated from the FE model agrees well with those predicted by Eqn 3.7 and measured in the experiments (Fig S6). The FE model simulates the swollen equilibrium state (i.e., the transient solvent migration process is not included in the simulations). We estimate the equilibrium swelling ratio of the initial DC hydrogel as $J_0 = 10.1$ by using the measured shear modulus $\mu_{\text{gel}} = 19$ kPa and numerically iterating Eqns 3.5 and 3.7. This value is not far from the experimentally measured swelling ratio $J_0 = 8.8$ of the as-prepared DC hydrogel, which further justifies the use of the FE model.

With the validated model for the stimuli-responsive adhesive, we next build a two-dimensional plane-strain model to simulate the adhesion between the adhesive and the model tissue. This model consists of an adhesive layer (80×1.5 mm^2) on top and a rigid substrate (100×3 mm^2) underneath to represent the model tissue (Fig 3.5a). At the interface, an edge crack of 10 mm is introduced in the left end, and the rest of the interface is bonded through a cohesive zone model, which is set as mode-independent and defined by a prescribed adhesion energy G_c (Fig S7). The cohesive zone model has been widely implemented to model bulk and interfacial cracks [44, 45, 46]. Notably, it was used to successfully model the peeling process of a tough hydrogel from a rigid substrate in recent studies [35, 47]. A typical simulation starts from 294 K to a higher temperature under a prescribed adhesion energy G_c. Fig 3.5b plots two simulations at 315 K but with different G_c values. The interfacial crack is trapped when $G_c = 11$ J/m^2 (Fig 3.5b top) but propagates when $G_c = 4$ J/m^2 (Fig 3.5b bottom). As the temperature increases, the energy release rate G ramps from zero due to volume shrinkage of the adhesive matrix. When G reaches the prescribed adhesion energy G_c at a certain temperature, the interface crack starts to propagate. Therefore, the debonding is governed by the critical condition $G = G_c$. Note that the debonded portion of the adhesive undergoes free deswelling upon stimulation, which explains why the debonded adhesive for $G_c = 4$ J/m^2 (Fig 3.5b bottom) appears to be shorter than that for $G_c = 11$ J/m^2 (Fig 3.5b top).

3.4.6 Numerical Estimation of the Energy Release Rate G.

After the establishment of the FE model, we leverage the critical debonding condition $G = G_c$ to estimate the energy release rate G at a given temperature T. As can be seen below, the approach is facile to determine G without invoking a sophisticated analysis. We conduct a series of above-mentioned FE simulations with varying adhesion energies G_c, which allows us to determine a specific temperature when the interfacial crack starts to propagate. Note that these simulations do not account for bulk hysteresis in the adhesive matrix (Fig S5), which have been shown to enhance the adhesion energy G_c. This is because our focus here is on estimating G at different temperatures and thus G_c is treated as a prescribed variable. The critical condition $G = G_c$ for the onset of crack propagation is still valid in the case of bulk hysteresis, as long as the contribution of bulk hysteresis is incorporated into G_c [48]. Although the exact values of G_c are not pursued here, it is worth noting that they can be characterized by a fatigue test and have recently been incorporated into the FE simulations to determine the apparent adhesion energy [49].

Given the severe modulus mismatch between the hydrogel and the model tissue, the interface crack is expected to be subjected to a mixed-mode fracture condition. To probe the effect of the mixed-mode condition on the G estimation, we also conduct simulations with the mode-I-dominant cohesive zone model in addition to the mode-independent counterpart (Supporting Information). The mode-I-dominant model relaxes the resistance to slippage on the interface than the former, which could result in distinct deformation modes near the crack tip [50] (Figs S8 and S9). Fig 3.5c shows that the two types of cohesive zone models lead to a quantitative difference in the G estimation, which is attributed to the different deformation modes of the interface crack, as observed in Figs S8 and S9. However, the two cases, mode-I-dominant or mode-independent, follow a qualitatively similar trend, that is, G increases monotonically with temperature T and then approaches a plateau at a sufficiently high T in both cases. The plateau in G is because the incremental volume shrinkage of the DC hydrogel becomes much smaller when T exceeds 310 K.

3.4.7 Rational Design of the Bonding of a Stimuli Responsive Hydrogel Adhesive.

These results provide a rational guideline to control the bonding state of the smart adhesive upon stimulation. When the adhesion energy is set beyond the plateau value, no debonding is found in the simulation, indicating the phase transition is insufficient to drive the interfacial crack propagation. Specifically, the plateau value of G at a high temperature is about 9 J/m^2

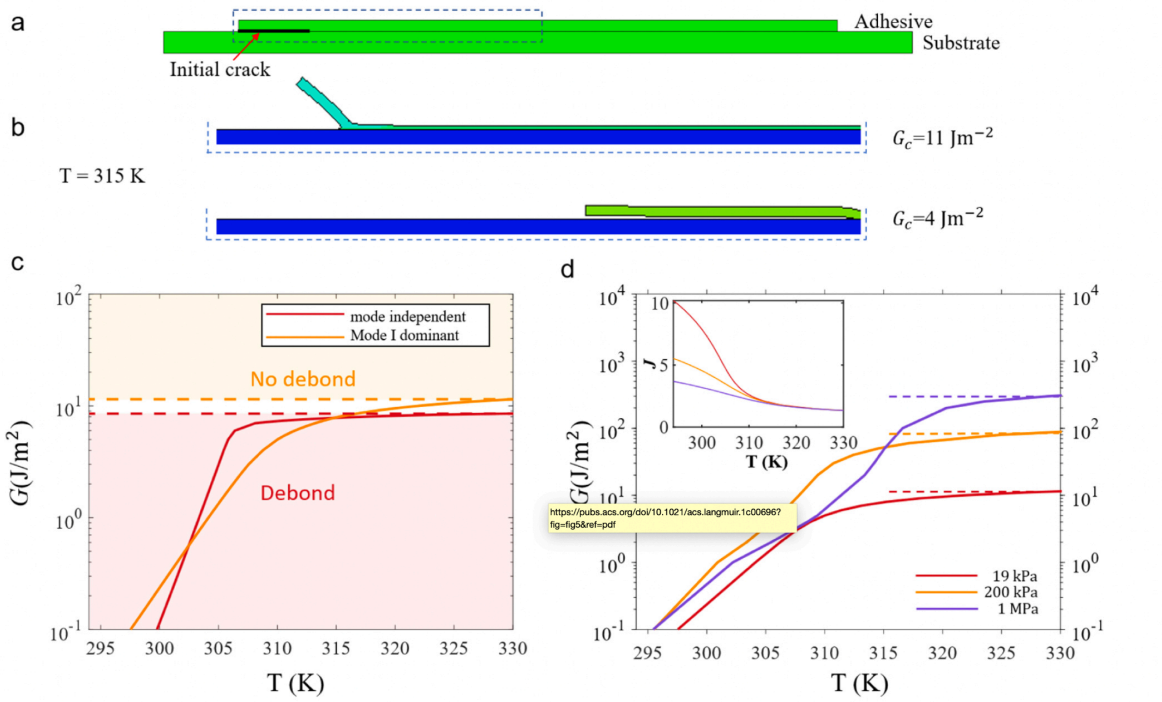

Fig. 3.5: FE model of the stimuli-responsive hydrogel adhesive. (a) FEM profile of the hydrogel adhesive and the substrate in the undeformed configuration. (b) Enlarged views of the crack tip region, boxed with dashed lines in (a), when temperature is at 315 K with $G_c = 11$ J/m^2 (top) and $G_c = 4$ J/m^2 (bottom) assuming a mode-independent crack. For $G_c = 4$ J/m^2, most of the adhesive (99% in area) is detached from the substrate as the temperature reaches 315 K. (c) Strain energy release rate G on the adhesive-tissue interface for mode-I-dominant and mode-independent cracks with $\mu = 19$ kPa. (d) Strain energy release rate G on the adhesive-tissue interface with different shear moduli given a mode-I dominant crack. The adhesive matrix with higher moduli exhibits higher plateau values of G. The inset shows the equilibrium swelling ratio J of the DC hydrogels as a function of temperature.

for the mode-independent crack, slightly lower than that of the mode-I-dominant crack (~ 11 J/m^2). These two plateau values, on the same order of magnitude as that estimated by the analytical model (6.6 J/m^2), provide a threshold band of the adhesion energy G_c as illustrated in Fig 3.5C. When G_c is below this band, crack propagation would occur under both the mode-I-dominant and mode-independent cases. When G_c is above this band, debonding would not occur in neither case.

Besides the adhesion energy G_c, the shear modulus of the adhesive matrix could be tuned to manipulate the bonding state. Since Eqns 3.10 and 2.23 imply that the energy release rate G induced by the residual stress is positively correlated to the shear modulus μ of the DC hydrogel, we also varied μ in the FE model and investigate the corresponding range of G. To this end, we set the shear modulus μ to be 19 kPa, 200 kPa, or 1 MPa (an accessible

range for hydrogels) and plot the values of G at different temperatures in Fig 3.5D. It should be noted that the equilibrium swelling ratio J is also affected by μ as predicted by Eqn 3.7, that is, the relative volume change due to phase transition decreases with increasing shear modulus (inset in Fig 3.5D). For example, if $\mu = 19$ kPa, the swelling ratio J changes from 10.2 to 2.5 as temperature T increases from 294 to 310 K. However, if $\mu = 1$ MPa, J changes from 3.7 to 2.2 over the same temperature range. Despite the smaller relative volume change accompanying the increasing shear modulus, the plateau G value still increases considerably, that is, from 10 J/m^2 for $\mu = 19$ kPa to 300 J/m^2 for $\mu = 1$ MPa. The result shows good agreement with the trend predicted by Eqn 3.10. The study sheds light on potential avenues to achieve high level control over the adhesion and mechanics of adhesive materials.

3.4.8 Applicability of Our Results.

Lastly, we discuss the applicability and implication of this work. The analytical and computational models above were built upon several assumptions. First, the tissue is assumed to be much stiffer than the adhesive. It is a reasonable assumption for skin and other tissues such as cartilage, which exhibit large moduli and/or potent strain-stiffening effects. Considering very soft tissues such as brain and adipose, the tissue substrate can deform to offset the deformation of the adhesive upon stimulation. Thus, a lower G_{in} is expected on the interface compared to the prediction from our analysis. While the toughening effect of the stimulation on the adhesive still holds, we expect robust adhesion of the stimuli-responsive hydrogel adhesive, independent of stimulation, for other substrates with a wide range of stiffness. The point is supported by our prior work and other ongoing studies, showing robust adhesion of the stimuli-responsive hydrogel adhesive on porcine skin and rodent skin in *vivo* [21]. Second, we demonstrate the design principle of the stimuli-responsive adhesive using the alginate/PNIPAm hydrogel because its stimulus, i.e., temperature, is easily controllable and its utility for wound management has been demonstrated. Given the diversity of stimuli-responsive hydrogels, our design is not limited to this specific material system but can be applied to other material systems responsive to other stimuli such as pH and light as long as they can form appreciable adhesion with different adhesive strategies. Moreover, the analytical model developed in this work is applicable to other material systems, while the FE model can be extended by incorporating the formulations for other stimuli-responsive mechanisms, as reported in the literature [51].

3.5 Conclusion

To summarize, we developed a design principle of switchable adhesives based on stimuli-responsive behavior of hydrogels. We demonstrated that the bonding of the adhesives can be modulated with stimulation depending on the interfacial bonding. With sufficient initial adhesion energy, such adhesives were able to stiffen and toughen on-demand in response to external stimuli such as temperature. In particular, the stimulation doubled the adhesion energy of the adhesive on a tissue-mimicking collagen substrate, suggesting PS deswelling as a toughening mechanism. Also, we characterized the free energy function of the stimuli-responsive adhesive and developed both analytical and FE models to quantitatively study the interplay between the stimulation and the interfacial fracture process. Our analysis determined the quantitative contribution of the stimulation to the strain energy release rate that drives the interfacial crack. We further presented strategies to modulate the interfacial fracture process, for instance, by tuning the modulus of the adhesive. The design principle of stimuli-responsive adhesives offers enormous design space to accommodate different stimuli-responsive hydrogels and adhesive strategies. This study establishes a rational design of stimuli-responsive hydrogel adhesive and is anticipated to spark the interest and motivate the development of smart adhesives.

3.6 Nomenclature

G: energy release rate induced by contraction or intrinsic energy release rate

G_c: adhesion energy

Γ: fracture energy

μ: shear modulus

E: elastic modulus

S_r: nominal residual stress

σ_r: true residual stress

P_i (i = 1,2,3): force per length

M_i (i = 1,2,3): moment per length

P_r and M_r: effective force per length and moment per length

J: swelling ratio with respect to dry polymer

F_f: plateau peeling force

W: strain energy density

N: nominal chain density

k: Boltzman constant

T: Temperature

C: nominal number of water molecules per unit volume

χ: Flory parameter

Ω: volume of a water molecule

Bibliography

[1] Zhen Yang, Xingwei Yang, Rong Long, and Jianyu Li. Stimulation modulates adhesion and mechanics of hydrogel adhesives. *Langmuir*, 37(23):7097–7106, 2021.

[2] Carrie E Brubaker and Phillip B Messersmith. The present and future of biologically inspired adhesive interfaces and materials. *Langmuir*, 28(4):2200–2205, 2012.

[3] Zhenwei Ma, Guangyu Bao, and Jianyu Li. Multifaceted design and emerging applications of tissue adhesives. *Advanced Materials*, 33(24):2007663, 2021.

[4] Sungmin Nam and David Mooney. Polymeric tissue adhesives. *Chemical Reviews*, 121(18):11336–11384, 2021.

[5] Andrew B Croll, Nasibeh Hosseini, and Michael D Bartlett. Switchable adhesives for multifunctional interfaces. *Advanced Materials Technologies*, 4(8):1900193, 2019.

[6] Costantino Creton. Pressure-sensitive adhesives: an introductory course. *MRS bulletin*, 28(6):434–439, 2003.

[7] Joaquin Delgado and Spencer F Silver. Thermomorphic" smart" pressure sensitive adhesives, March 30 1999. US Patent 5,889,118.

[8] Yang Gao, Kangling Wu, and Zhigang Suo. Photodetachable adhesion. *Advanced Materials*, 31(6):1806948, 2019.

[9] Xiaoyu Chen, Hyunwoo Yuk, Jingjing Wu, Christoph S Nabzdyk, and Xuanhe Zhao. Instant tough bioadhesive with triggerable benign detachment. *Proceedings of the National Academy of Sciences*, 117(27):15497–15503, 2020.

[10] Pei-Chun Lin, Shilpi Vajpayee, Anand Jagota, Chung-Yuen Hui, and Shu Yang. Mechanically tunable dry adhesive from wrinkled elastomers. *Soft Matter*, 4(9):1830–1835, 2008.

[11] Qi Li, Ping Zhang, Canhui Yang, Huiling Duan, and Wei Hong. Switchable adhesion between hydrogels by wrinkling. *Extreme Mechanics Letters*, 43:101193, 2021.

[12] Ameya R Narkar and Bruce P Lee. Incorporation of anionic monomer to tune the reversible catechol–boronate complex for ph-responsive, reversible adhesion. *Langmuir*, 34(32):9410–9417, 2018.

[13] Patrick G Lawrence and Yakov Lapitsky. Ionically cross-linked poly (allylamine) as a stimulus-responsive underwater adhesive: Ionic strength and ph effects. *Langmuir*, 31(4):1564–1574, 2015.

[14] Hoon Eui Jeong, Moon Kyu Kwak, and Kahp Y Suh. Stretchable, adhesion-tunable dry adhesive by surface wrinkling. *Langmuir*, 26(4):2223–2226, 2010.

[15] Chunxiao Chai, Yiyi Guo, Zhaohui Huang, Zhuo Zhang, Shuang Yang, Weiwei Li, Yunpeng Zhao, and Jingcheng Hao. Antiswelling and durable adhesion biodegradable hydrogels for tissue repairs and strain sensors. *Langmuir*, 36(35):10448–10459, 2020.

[16] Xuezhong He, Xiaoming Yang, and Esmaiel Jabbari. Combined effect of osteopontin and bmp-2 derived peptides grafted to an adhesive hydrogel on osteogenic and vasculogenic differentiation of marrow stromal cells. *Langmuir*, 28(12):5387–5397, 2012.

[17] Gabriele Sadowski and Walter Richtering. *Intelligent hydrogels*, volume 140. Springer, 2014. ISBN: 9783319016832.

[18] Xinyue Liu, Ji Liu, Shaoting Lin, and Xuanhe Zhao. Hydrogel machines. *Materials Today*, 36:102–124, 2020.

[19] Jianyu Li and David J Mooney. Designing hydrogels for controlled drug delivery. *Nature Reviews Materials*, 1(12):1–17, 2016.

[20] Yoonho Kim, German A Parada, Shengduo Liu, and Xuanhe Zhao. Ferromagnetic soft continuum robots. *Science Robotics*, 4(33):eaax7329, 2019.

[21] Serena Blacklow, Jianyu Li, Benjamin R Freedman, Mahdi Zeidi, Chen Chen, and David J Mooney. Bioinspired mechanically active adhesive dressings to accelerate wound closure. *Science Advances*, 5(7):eaaw3963, 2019.

[22] Jeong-Yun Sun, Xuanhe Zhao, Widusha RK Illeperuma, Ovijit Chaudhuri, Kyu Hwan Oh, David J Mooney, Joost J Vlassak, and Zhigang Suo. Highly stretchable and tough hydrogels. *Nature*, 489(7414):133–136, 2012.

[23] Jianyu Li, Adam D Celiz, Jiawei Yang, Quansan Yang, Isaac Wamala, William Whyte, Bo Ri Seo, Nikolay Vasilyev, Joost J Vlassak, and Mooney David J Suo, Zhigang. Tough adhesives for diverse wet surfaces. *Science*, 357(6349):378–381, 2017.

[24] Howard G Schild. Poly (n-isopropylacrylamide): experiment, theory and application. *Progress in polymer science*, 17(2):163–249, 1992.

[25] Wei Hong, Xuanhe Zhao, Jinxiong Zhou, and Zhigang Suo. A theory of coupled diffusion and large deformation in polymeric gels. *Journal of the Mechanics and Physics of Solids*, 56(5):1779–1793, 2008.

[26] Shengqiang Cai and Zhigang Suo. Mechanics and chemical thermodynamics of phase transition in temperature-sensitive hydrogels. *Journal of the Mechanics and Physics of Solids*, 59(11):2259–2278, 2011.

[27] Wei Hong, Zishun Liu, and Zhigang Suo. Inhomogeneous swelling of a gel in equilibrium with a solvent and mechanical load. *International Journal of Solids and Structures*, 46(17):3282–3289, 2009.

[28] Paul J Flory. *Principles of polymer chemistry*. Cornell university press, 1953. ISBN: 9780801401343.

[29] Paul J Flory. Thermodynamics of high polymer solutions. *The Journal of chemical physics*, 10(1):51–61, 1942.

[30] Maurice L Huggins. Solutions of long chain compounds. *The Journal of chemical physics*, 9(5):440–440, 1941.

[31] Maurice L Huggins. A revised theory of high polymer solutions. *Journal of the American Chemical Society*, 86(17):3535–3540, 1964.

[32] Widusha RK Illeperuma, Jeong-Yun Sun, Zhigang Suo, and Joost J Vlassak. Force and stroke of a hydrogel actuator. *Soft Matter*, 9(35):8504–8511, 2013.

[33] Ziqian Li, Zishun Liu, Teng Yong Ng, and Pradeep Sharma. The effect of water content on the elastic modulus and fracture energy of hydrogel. *Extreme Mechanics Letters*, 35:100617, 2020.

[34] Jianyu Li, Yuhang Hu, Joost J Vlassak, and Zhigang Suo. Experimental determination of equations of state for ideal elastomeric gels. *Soft Matter*, 8(31):8121–8128, 2012.

[35] Hyunwoo Yuk, Teng Zhang, Shaoting Lin, German Alberto Parada, and Xuanhe Zhao. Tough bonding of hydrogels to diverse non-porous surfaces. *Nature Materials*, 15(2):190–196, 2016.

[36] Kevin Kendall. Thin-film peeling-the elastic term. *Journal of Physics D: Applied Physics*, 8(13):1449, 1975.

[37] Canhui Yang, Tenghao Yin, and Zhigang Suo. Polyacrylamide hydrogels. i. network imperfection. *Journal of the Mechanics and Physics of Solids*, 131:43–55, 2019.

[38] Shengqiang Cai and Zhigang Suo. Equations of state for ideal elastomeric gels. *EPL (Europhysics Letters)*, 97(3):34009, 2012.

[39] Ken-ichi Hoshino, Tasuku Nakajima, Takahiro Matsuda, Takamasa Sakai, and Jian Ping Gong. Network elasticity of a model hydrogel as a function of swelling ratio: from shrinking to extreme swelling states. *Soft Matter*, 14(47):9693–9701, 2018.

[40] Takamasa Sakai, Manami Kurakazu, Yuki Akagi, Mitsuhiro Shibayama, and Ung-il Chung. Effect of swelling and deswelling on the elasticity of polymer networks in the dilute to semi-dilute region. *Soft Matter*, 8(9):2730–2736, 2012.

[41] Jingda Tang, Jianyu Li, Joost J Vlassak, and Zhigang Suo. Fatigue fracture of hydrogels. *Extreme Mechanics Letters*, 10:24–31, 2017.

[42] Xiang Ni, Zhen Yang, and Jianyu Li. Scaling behavior of fracture properties of tough adhesive hydrogels. *ACS Macro Letters*, 10(2):180–185, 2021.

[43] Zhigang Suo and John W Hutchinson. Interface crack between two elastic layers. *International Journal of Fracture*, 43(1):1–18, 1990.

[44] Chung-Yuen Hui, Andy Ruina, Rong Long, and Anand Jagota. Cohesive zone models and fracture. *The Journal of Adhesion*, 87(1):1–52, 2011.

[45] Viggo Tvergaard and John W Hutchinson. On the toughness of ductile adhesive joints. *Journal of the Mechanics and Physics of Solids*, 44(5):789–800, 1996.

[46] Yueguang Wei and John W Hutchinson. Interface strength, work of adhesion and plasticity in the peel test. In *Recent advances in fracture mechanics*, pages 315–333. Springer, 1998.

[47] Teng Zhang, Hyunwoo Yuk, Shaoting Lin, German A Parada, and Xuanhe Zhao. Tough and tunable adhesion of hydrogels: experiments and models. *Acta Mechanica Sinica*, 33(3):543–554, 2017.

[48] Rong Long and Chung-Yuen Hui. Fracture toughness of hydrogels: measurement and interpretation. *Soft Matter*, 12(39):8069–8086, 2016.

[49] Zhen Yang, Zhenwei Ma, Shiyu Liu, and Jianyu Li. Tissue adhesion with tough hydrogels: Experiments and modeling. *Mechanics of Materials*, 157:103800, 2021.

[50] Bi-min Zhang Newby, Manoj K Chaudhury, and Hugh R Brown. Macroscopic evidence of the effect of interfacial slippage on adhesion. *Science*, 269(5229):1407–1409, 1995.

[51] Romain Marcombe, Shengqiang Cai, Wei Hong, Xuanhe Zhao, Yuri Lapusta, and Zhigang Suo. A theory of constrained swelling of a ph-sensitive hydrogel. *Soft Matter*, 6(4):784–793, 2010.

Supporting information

Materials

Materials

Chemicals used in this work were purchased without further purification. Poly(N-isopropylacrylamide) (NIPAm, monomer) was purchased from TCI (Portland, USA); N,N'-methylenebis (acrylamide) (MBAA, covalent crosslinker), N,N,N',N'-tetramethylethylenediamine (TEMED, accelerator), ammonium persulfate (APS, initiator), calcium sulfate (ionic crosslinker), N-hydroxysulfosuccinimide (NHS), and 1-ethyl-3-(3-dimethylaminopropyl) carbodiimide (EDC) were purchased from Sigma Aldrich (St. Louis, Missouri, USA). Alginate (I-1G) was purchased from KIMICA Corporation (Tokyo, Japan). Chitosan (deacetylation degree 95%, medium to high molecular weight) was purchased from Xi'an Lyphar Biotech (Shanxi, China). Glass and acrylic sheets were purchased from McMaster-Carr to make reaction molds. Collagen casing was purchased from a local grocery store and then stored in the fridge at 4°C before use.

Synthesis of stimuli-responsive hydrogel adhesive.

Following previously reported protocols [1, 2], the stimuli-responsive adhesive is made of two layers: a dissipative matrix made of PNIPAm/alginate hydrogel and a topohesive surface (chitosan, EDC and NHS) to form a bridging network with tissues. To synthesize the hydrogel, 6.3 g of NIPAm monomers and 1 g of sodium alginate were first dissolved in 50 mL of deionized water. Then, 10 ml of the NIPAm-alginate solution was mixed with 22.54 μL of MBAA aqueous solution (0.28 mM) and 5.8 μL of TEMED (3.7 mM) within a syringe. Meanwhile, 234.7 μL of APS solution (6.5 mM) and 179.72 μL calcium sulfate slurries ($CaSO_4$, 0.15M) were mixed in another syringe. The two syringes were connected with a Luer Lock connector and syringe-mixed quickly to form a homogeneous solution. The mixture was immediately injected into a mold with 80×15×1.5 mm^3 in size, covered with a glass plate and subsequently kept at 4°C for 24 hours to complete the reaction. The same procedure was followed for synthesizing the PNIPAm/alginate single-network (SC) hydrogel, except that the calcium sulfate slurries were replaced by deionized water of the same volume.

To prepare topohesive with chemical reagents, 1 g of chitosan powder was firstly dissolved in 50 mL deionized water with 400 μL of acetic acid for a final pH of 4.5. The mixture was stirred overnight to form a homogenous solution and then kept at 4°C before use. Then,

varying concentrations (0, 2 and 6% w/v) of coupling reagents (EDC and NHS at equal weights) were added into 1 mL of the 2% w/v chitosan solution.

To prepare topohesive without chemical reagents, 0g, 0.25 g, 0.5g, 1g of chitosan powder were dissolved in 50 mL deionized water with acetic acid for a final pH of 4.5, for 0%, 0.5%, 1%, and 2% w/v chitosan concentrations, respectively.

Fabrication of the model tissue.

We fabricated a model tissue substrate with a collagen casing and an acrylic sheet. The dry collagen casing was soaked in deionized water for 30 minutes and subsequently glued onto the acrylic sheet (Fig S1). The model tissue provides abundant amino and carboxyl groups from collagen casing for covalent bonding with the adhesive. It is considered as a rigid substrate due to the high elastic modulus of the acrylic (on the order of 1 GPa). Also, the model tissue is flat and smooth. The hydrogel adhesives were attached onto the model tissues with topohesives of varying chemical reagent inputs, while other conditions, for example, the applied compression and the reaction time, were kept the same. An initial crack of 15 mm was introduced near the one end of the sample, and the length of the overlapping joint was 65 mm for adhesion energy measurements. After the placement of the adhesive, the samples were clamped between two acrylic sheets for compression and then stored in a seal bag at 4°C for 24 hours.

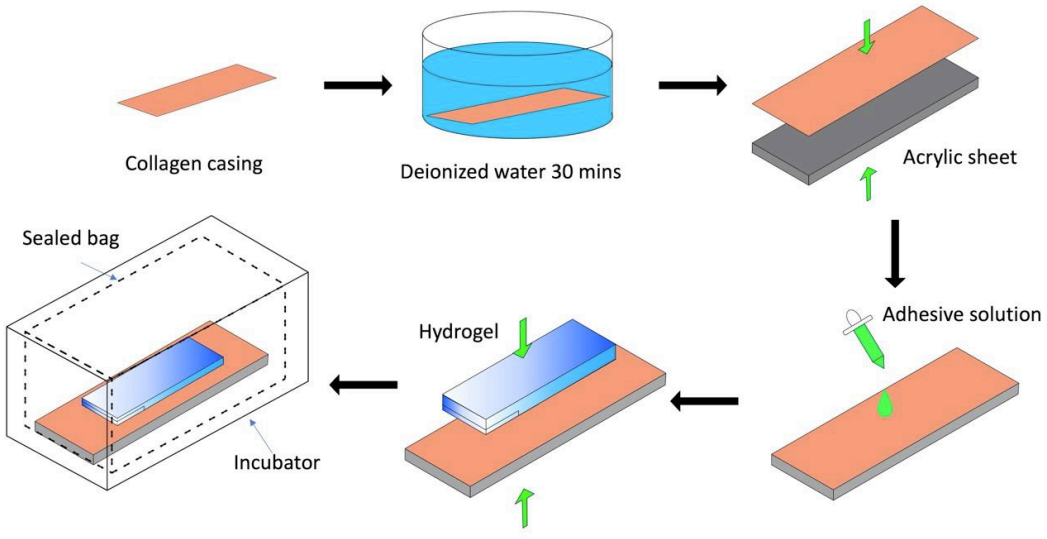

Fig. 3.S1: Fabrication of the model tissue and the application of the stimuli-responsive adhesive. The stimulation is realized by placing the specimen in an incubator of 37°C.

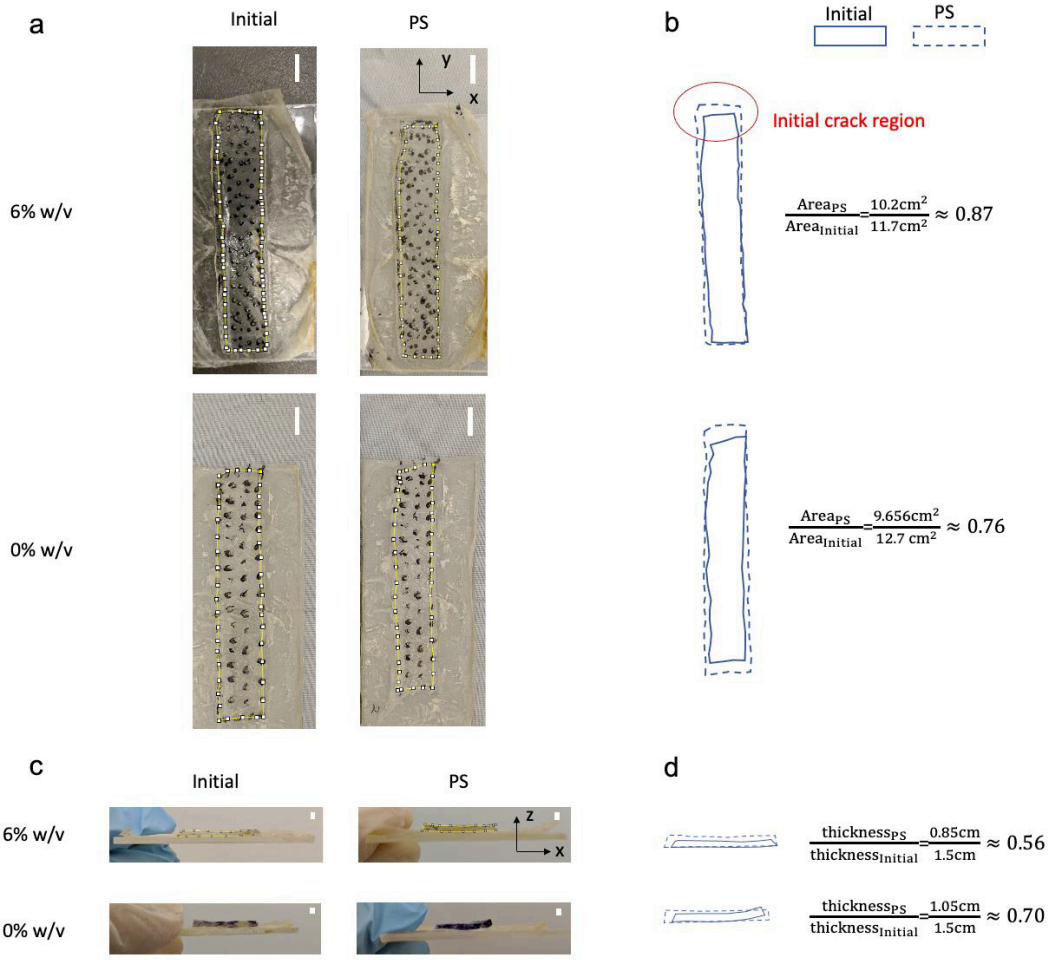

Fig. 3.S2: Images and contours of the stimuli-responsive adhesive adhered onto the model tissue substrate before and after stimulation. (a) Images of the stimuli-responsive adhesive before and after stimulation and the contours (b) overlaid in the x-y plane. Scale bar, 1 cm. The ratio of the contour areas is calculated. The strong adhesion formed with 6% w/v coupling reagents results in in-plane contraction (area ratio ∼0.87) limited to the initial crack region. Without any coupling reagent, the adhesion is weaker, enabling substantial in-plane contraction (area ratio ∼ 0.76) at all edges of the specimen. (c) Images and (d) cross-sectional profiles of the stimuli-responsive adhesive before and after the stimulation in the x-z plane. Scale bar, 1.65 mm. The profiles shown in (d) is magnified for better illustration. The thickness reduction with 6% w/v reagent is slightly larger than that with 0% w/v reagent. Notably, one end of the adhesive with 0% reagent tilts up upon stimulation, indicative of delamination.

Additional information on finite element modeling.

Finite element (FE) simulations were performed using the commercial software ABAQUS (version 2020, Simulia, Providence, RI, USA). Below described are two types of simulations performed in this work, i.e., free swelling and interface debonding.

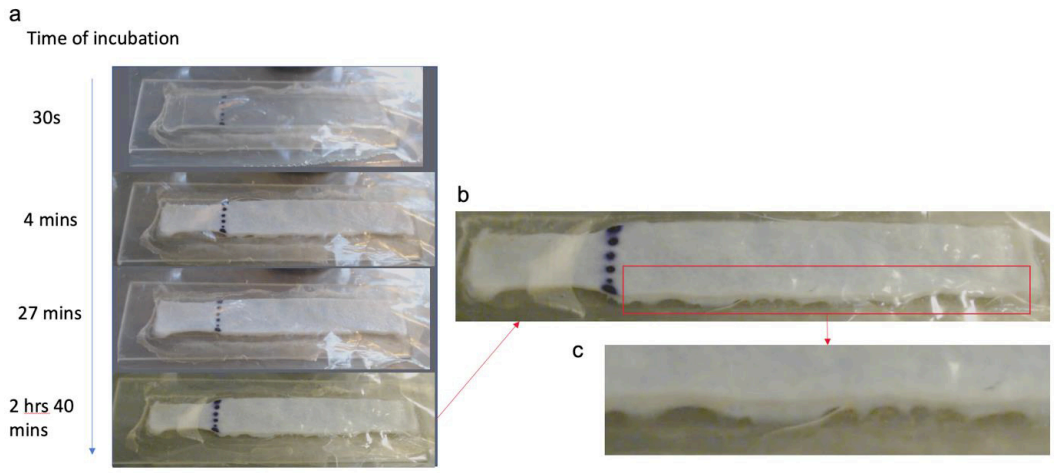

Fig. 3.S3: Time series images of the stimuli-responsive adhesive with 2%w/v reagents. (a) plots deformation change with incubation time. (b) Enlarged view of the adhesive hydrogel at 2hrs 40 mins in (a). (c) Enlarged view of the highlighted region in (b), showing localized debonding near the edge of the interface.

Free swelling.

A cubic block, $8\times8\times8\text{mm}^3$ in size, was used to represent the DC hydrogel in the FE model and was meshed using the 3D continuum element C3D8HT (512 elements in total). The hydrogel was subjected to a temperature change from 294K to 320K throughout the simulation. The simulations were performed using the coupled temperature-displacement analysis. Fig S6 shows the volume change of the hydrogel block in the FE model, when the temperature is elevated. The FE results is compared with the analytical estimation of the equilibrium swelling ratio J curve, i.e., the fitting function $H(J,T)$ for the shear modulus of the hydrogel μ=19 kPa. The two results show a good agreement. Moreover, the experimental results for the swelling test of the as-prepared DC hydrogel is also plotted in Fig S6 for comparison, showing a qualitative agreement with both the FE and the analytical results. The quantitative difference is due to the fact that the as-prepared DC hydrogel is not in swelling equilibrium under the room temperature, nor under 320 K due to the limited stimulation time.

Interface debonding.

A two-dimensional plane strain model was developed to study the interface debonding between the hydrogel adhesive and the model tissue. The model consists of a hydrogel adhesive on a substrate representing the model tissue (Fig S7). The substrate was modelled as a rigid body with the bottom surface fixed in all degrees of freedom. The hydrogel adhesive was modelled using the Flory-Rhener free energy function via the UHYPER user subroutine.

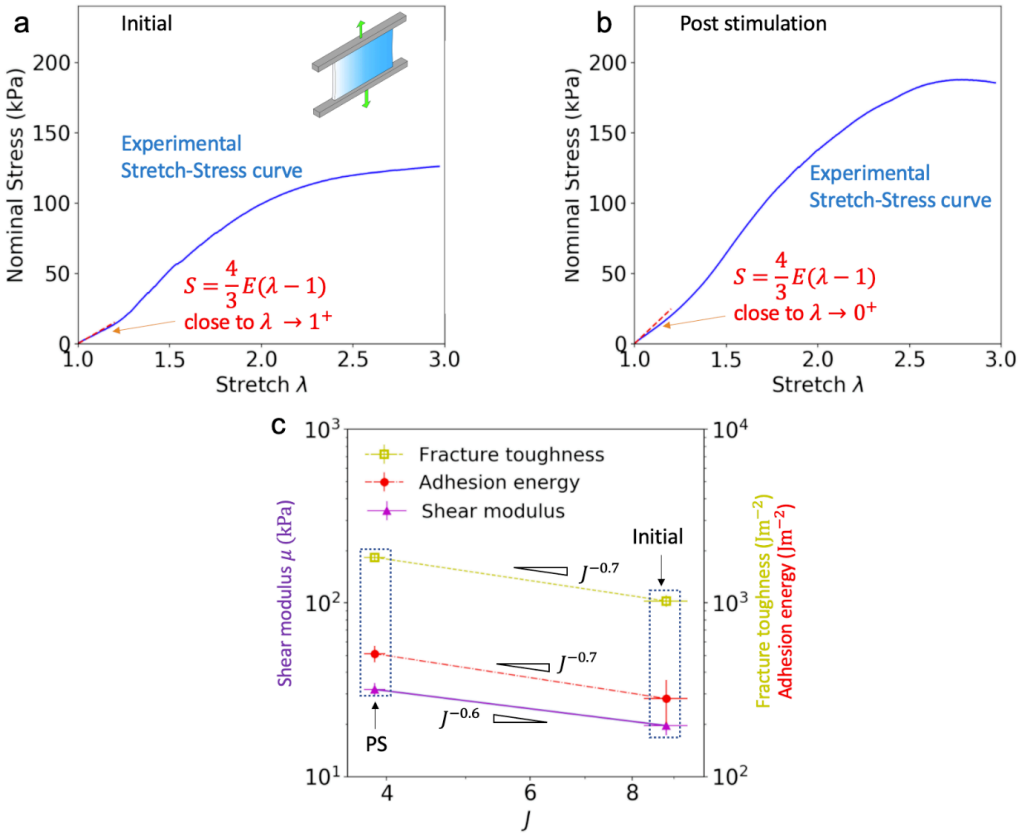

Fig. 3.S4: Stress-stretch curves of the stimuli-responsive adhesive before and after stimulation in pure shear tests. Representative nominal stress-stretch curves for the initial (a) and the post stimulation (b) states. The elastic modulus is measured by assessing the slope of the initial portion of the curve, $\partial S/\partial(\lambda - 1) = 4E/3$. (c) Adhesion energy, bulk fracture energy and shear modulus plotted as functions of swelling ratio J. The adhesion energy corresponding to the case with topohesives containing 6% w/v reagents. Sample size n = 3.

The interface between the hydrogel adhesive and the model tissue was modelled using a cohesive zone model, which was defined by prescribing a relation between the mechanical traction and the relative separation between the two contacting surfaces. [3] Here we adopted a simple bilinear traction-separation law for the cohesive zone model, as illustrated in Fig S7. The cohesive zone model features a few parameters: δ_f and σ_{max} are the maximum separation and strength, respectively, while K is the initial stiffness and $\Gamma_a = \sigma_{max}\delta_f/2$ is the area underneath the traction-separation curve, representing the adhesion energy between the interface. Complete interface failure occurs when δ_f is reached and the traction reduces to 0. In this work, we used $\delta_f = 0.5$ mm and $K = 10^{11}$ N/m^3. The schematic in Fig S7 only shows the traction-separation law along one direction. However, in simulations the interface is subjected to tractions both in its normal and tangential directions. To account

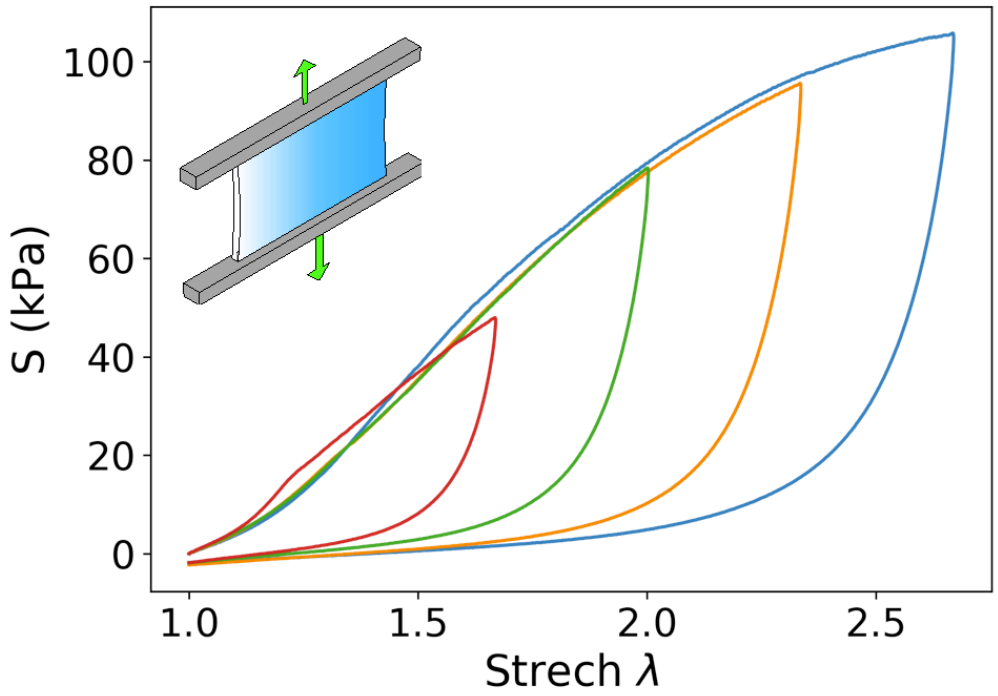

Fig. 3.S5: Nominal stress-stretch curves for the PNIPAm/alginate DC hydrogels in a pure shear specimen (inset) loaded up to different stretches. The loading-unloading curves form hysteresis loops, indicative of significant energy dissipation.

for tractions in these two directions, we used the following quadratic stress criterion for the damage initiation:

$$\left(\frac{\sigma_{\mathrm{n}}}{\sigma_{n,max}}\right)^2 + \left(\frac{\sigma_{\mathrm{t}}}{\sigma_{t,max}}\right)^2 = 1$$

with σ_{n} and σ_{t} representing tractions normal and tangential to the interface, respectively. As mentioned in the main text, two types of cohesive zone models were used: i) mode-independent, and ii) Mode-I dominant. In the former model, we set $\sigma_{\mathrm{n,max}} = \sigma_{\mathrm{t,max}}$ and Γ_a depends on both the normal and tangential directions in an isotopic manner. In the latter model, we set $\sigma_{\mathrm{n,max}} = 20\ \sigma_{\mathrm{t,max}}$ such that the adhesion energy Γ_a is dominated by traction along the normal direction. In the simulations, the hydrogel adhesive and substrate were initially at 294K. They were subjected to a temperature increase until the crack started to propagate on the interface, after which the temperature was held until most of the interface (i.e., ¿90% in area) delaminates. Different adhesion energies Γ_a were prescribed to determine the temperature at the onset of interface crack propagation. Examples showing the deformed configurations of the mode-independent and Mode- I dominant cases are shown in Fig S8 and Fig S9, respectively. In the mode-independent case, we observed that the deformed

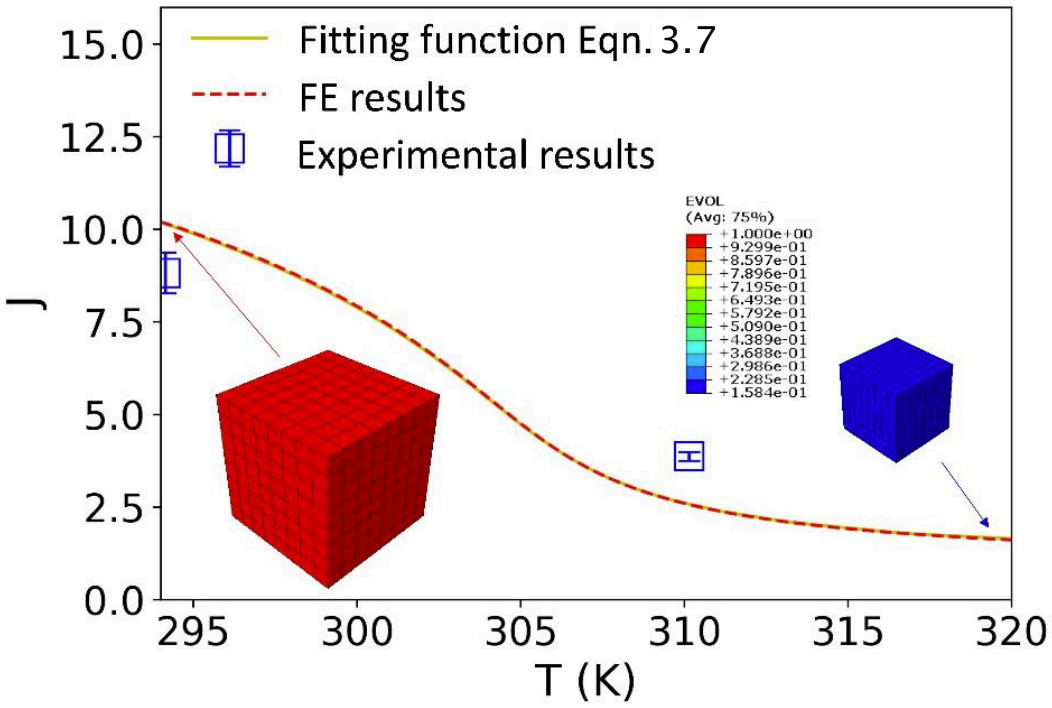

Fig. 3.S6: Equilibrium swelling ratio J: analytical estimate (solid line), FE results (dashed line) and experimental data (symbols). The insets illustrate the volumetric deformation of a hydrogel cube subjected to the temperature increase. The color contour shows the swelling ratio defined as EVOL, the ratio of the current volume versus the initial volume.

crack surface deflected forward and exhibited a fingertip-like shape (Fig S8 (a) and (b)), leading to the excessive distortion in the elements near the crack tip and causing convergence issue. As a result, for the mode-independent case, the 6-node modified displacement and temperature element CPE6MHT was used [Figure S8(c)] to suppress mesh distortion. The size of the element was set to be uniformly 0.25 mm, which was half of δ_f and capable of capturing the interfacial behavior of the system. In the Mode-I dominant case, the absence of the fingertip-like shape near the crack tip enables us to use a more refined mesh to capture the large deformation of the hydrogel near the interface. The 4-node bilinear displacement and temperature element CPE4HT with a transition mesh (Fig S9(c)) was adopted for the hydrogel with the smallest element size being $\sim$0.03 mm. In addition to the pre-existing crack at the left side of the hydrogel, a new crack can initiate and propagate from the right edge of the hydrogel (Fig S8(a) and S9(a)). The critical temperature at the onset of crack propagation were extracted from FE simulations based on the damage parameter of the cohesive zone. Once the damage parameter of the first few cohesive elements near the crack tip reaches 1, the crack, either the pre-existing one or the new one initiated at the right

edge, can propagate steadily. Figure S10 shows the energy release rate G versus temperature for the two cases with mode-independent and Mode-I dominant cohesive zone models. The energy release rate for the pre-existing crack (left edge) and the new crack initiated (right edge) are close to each other, especially for relative high temperature (e.g., T > 305 K). For consistency, we adopted the results for the pre-existing crack in Fig 3.5 of the main text.

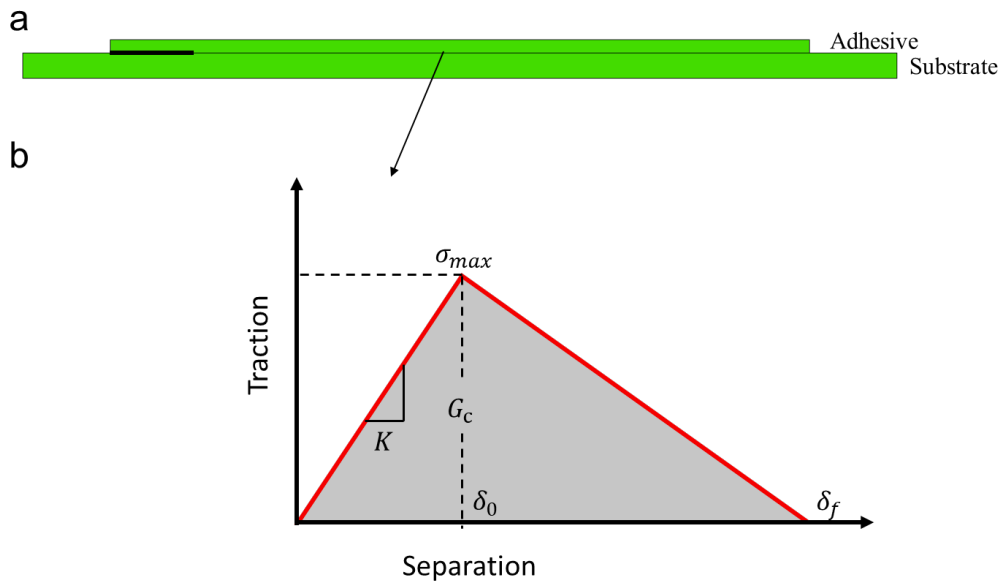

Fig. 3.S7: FE model geometry and cohesive zone. (a) The FE model consists of a hydrogel adhesive bonded to the top of a rigid substrate. (b) Adhesion on the interface between the hydrogel adhesive and the substrate is simulated using a cohesive zone model with bilinear traction-separation law.

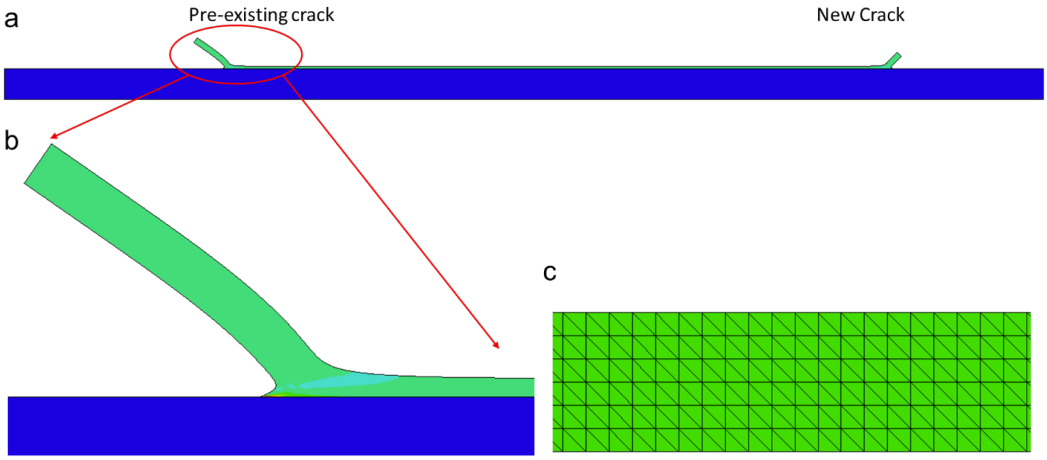

Fig. 3.S8: FE model with mode independent cohesive zone. (a) A representative deformation profile of the hydrogel adhesive. (b) Zoomed-in view of the crack tip. (c) Mesh used in the hydrogel adhesive.

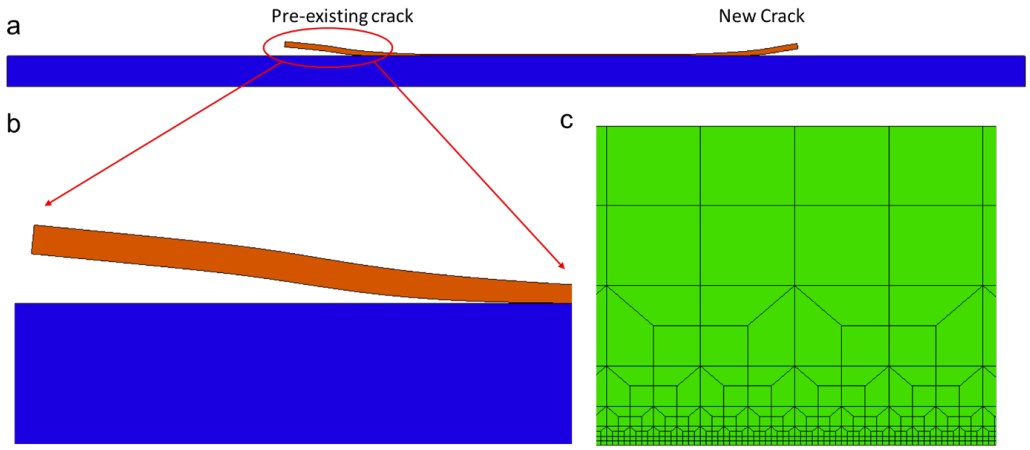

Fig. 3.S9: FE model with the Mode-I dominant cohesive zone. (a) A representative deformation profile of the hydrogel adhesive. (b) Zoomed-in view of the crack tip. (c) Mesh used in the hydrogel adhesive.

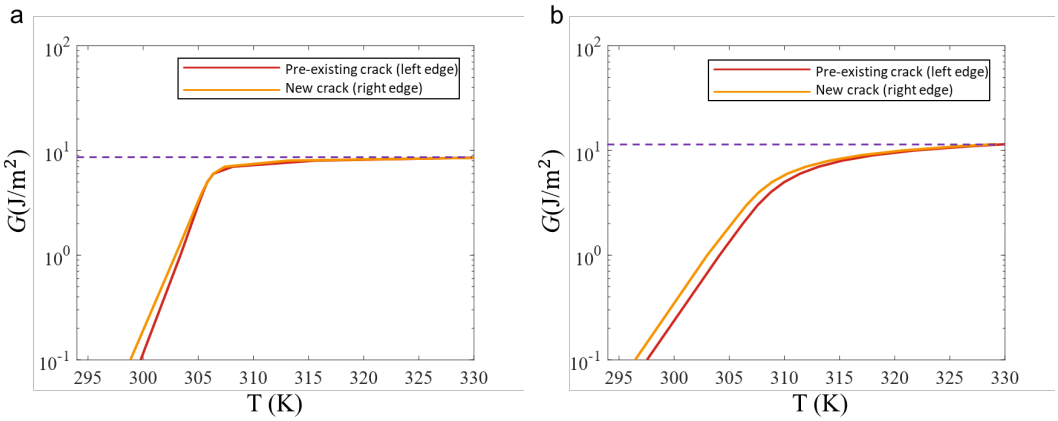

Fig. 3.S10: Intrinsic energy release rate G_{in} under temperature increase. (a) The intrinsic energy release rate G_{in} for both the pre-existing crack (left edge) and the new crack (right edge) using the mode independent cohesive zone. (b) G_{in} for both the pre-existing crack (left edge) and the new crack (right edge) using the Mode-I dominant cracks. The dashed lines in (a-b) represent the maximum values of G_{in} found in the simulation.

Bibliography

[1] Serena Blacklow, Jianyu Li, Benjamin R Freedman, Mahdi Zeidi, Chen Chen, and David J Mooney. Bioinspired mechanically active adhesive dressings to accelerate wound closure. *Science Advances*, 5(7):eaaw3963, 2019.

[2] Jianyu Li, Adam D Celiz, Jiawei Yang, Quansan Yang, Isaac Wamala, William Whyte, Bo Ri Seo, Nikolay Vasilyev, Joost J Vlassak, and Mooney David J Suo, Zhigang. Tough adhesives for diverse wet surfaces. *Science*, 357(6349):378–381, 2017.

[3] Chung-Yuen Hui, Andy Ruina, Rong Long, and Anand Jagota. Cohesive zone models and fracture. *The Journal of Adhesion*, 87(1):1–52, 2011.

Preamble to Chapter 4

Chapter 3 introduces a strategy for modulating hydrogel adhesion through the utilization of stimuli-responsive hydrogels. When subjected to stimulation, the hydrogel adhesive undergoes a spontaneous development of an intrinsic energy release rate. This energy release rate serves to counterbalance the adhesion energy, and its estimated value is within the order of 10 Jm^{-2} for alginate/PNIPAm hydrogel adhesives. It's important to note that this energy release rate falls short of achieving delamination at interfaces where the adhesion energy exceeds 100 Jm^{-2}. Moreover, in scenarios where the adhesion energy greatly surpasses this intrinsic energy release rate induced by contraction, the enhanced bulk mechanics of the hydrogel adhesive can even result in a nearly two-fold enhancement of adhesion, corresponding to a switch ratio of 2 (defined as the ratio of high adhesion energy to low adhesion energy). This insight lends strong support to the feasibility of designing stimuli-responsive hydrogel adhesives for applications like wound dressing, where robust adhesion can be achieved with relatively weak adhesion energies based on physical interactions. This is achievable as long as the adhesion energy remains greater than the energy release rate induced by the contraction mechanism, which is approximately 10 Jm^{-2}.

While the utilization of stimuli-responsiveness offers a valuable means to modulate adhesion, it's important to note that its capability might be somewhat limited when it comes to achieving more intricate control over adhesion kinetics and the spatial distribution of adhesion energy. To this end, the subsequent chapter adopts an alternative approach by directly manipulating the adhesion energy through the design of the polymer network topology. This strategy enables the fine-tuning of adhesion energy over a significant range. Furthermore, the manipulation of the polymer network topology introduces a novel design domain that encompasses the programming of adhesion energy, kinetics, and spatial distribution in a cohesive manner.

Chapter 4

Programming hydrogel adhesion with engineered network topology

4.1 Abstract

Hydrogel adhesion that can be easily modulated in magnitude, space, and time is desirable in many emerging applications ranging from tissue engineering and soft robotics to wearable devices. In synthetic materials, these complex adhesion behaviors are often achieved individually with mechanisms and apparatus that are difficult to integrate. Here, we report a universal strategy to embody multifaceted adhesion programmability in synthetic hydrogels. By designing the surface network topology of a hydrogel, supramolecular linkages that result in contrasting adhesion behaviors are formed on the hydrogel interface. The incorporation of different topological linkages leads to dynamically tunable adhesion with high-resolution spatial programmability without alteration of bulk mechanics and chemistry. Further, the association of linkages enables stable and tunable adhesion kinetics that can be tailored to suit different applications. We rationalize the physics of polymer chain slippage, rupture, and diffusion at play in the emergence of the programmable behaviors. With the understanding, we design and fabricate various soft devices such as smart wound patches, fluidic channels, drug-eluting devices, and reconfigurable soft robotics. Our study presents a simple and robust platform in which adhesion controllability in multiple aspects can be easily integrated into a single design of a hydrogel network.

4.2 Introduction

The precise programming of hydrogel adhesion, including its magnitude, kinetics, and spatial distribution, has significant implications for engineering, biology, and medicine. The ability to control adhesion energy is essential for bonding reinforcement or easy detachment after placement [1, 2, 3], while the ability to control adhesion spatially is useful for applications requiring varying adhesion properties on the targeted surface such as wound dressings [4]. While most current research has focused on the adhesion magnitude at the equilibrium stage, controlling adhesion kinetics, which involves modulating transient adhesion over time, is less explored but equally important as it allows for tuning the operating time window for adhesive placement. As such, programming the multifaceted nature of hydrogel adhesion could enable and improve various applications ranging from tissue repair to soft robotics. However, such programmable adhesion is difficult to achieve for synthetic adhesives because they require the addition of complex chemistry and apparatus that are potentially difficult to integrate. For instance, tough hydrogels with covalent bond-based adhesion provide robust adhesion to diverse surfaces [5], but it is challenging to modulate their adhesion without introducing

specific chemistry [6]. In contrast, physical interactions offer more flexibility to modulate hydrogel adhesion energy, but they require specific material properties (e.g., viscoelasticity) or additional apparatus (light, ultrasound, etc.) [7, 8, 9]. In terms of controlling adhesion kinetics, the rate of covalent bonding is fundamentally limited by the specific chemical reactions involved. Physical interactions such as hydrogen bond often form instantaneously [10], providing limited tunability in terms of adhesion kinetics. Achieving spatial control of adhesion requires sophisticated patterning and treatment of the opposing surface [11, 12], and the outcome could be compromised by uncontrolled diffusion of chemical reagents, especially when the two adherends are sufficiently permeable [7]. Selective masking of the opposing surface could enable spatially controlled adhesion [13, 14, 15], but may be difficult to perform on highly-uncontrolled and unpredictable surfaces such as biological tissues. A universal design strategy that inherently allows for robust and multifaceted adhesion programming on diverse surfaces is still missing.

It has been found that cells utilize dynamic bonding through non-covalent protein-protein interactions, known as slip bonds [16, 17]. These bonds exhibit dynamic adhesion strength, with a shorter lifetime under applied force due to the reduced energy barrier to bond rupture, allowing them to switch between bonding and motile states under different physiological environments [18]. Furthermore, cells can achieve complex spatiotemporal adhesion controls [19, 20], which are not yet seen among synthetic hydrogel adhesives. In this study, we present a novel approach to engineer surface network topology in hydrogels, which enables the creation of polymer entanglement referred to as the slip linkage (Fig 4.1a). The slip linkage has a topology of a long polymer chain entangled with another crosslinked network (chain-to-network) and can dissociate via chain slippage, a thermally activated process that results in dynamic adhesion analogous to slip bonds in cell adhesion. This enables the adhesion energy to be varied by many folds without background dissipation (Fig 4.1c). Moreover, the kinetics of slip linkage association dominates over other sub-kinetics that are dependent on operating conditions. By carefully tuning the governing length scale, it is possible to control the kinetics of slip linkage association, resulting in a stable adhesion kinetics with adjustable half time ranging from $\sim$50s to $\sim$1000s (Fig 4.1d). Furthermore, we demonstrate a simple fabrication method to pattern the slip linkage with another type of polymer entanglement, the stitch linkage, at the same interface (Fig 4.1b,e). The stitch linkage has the topology of two crosslinked polymer networks entangled together (network-to-network), as found in the hydrogel topological adhesion and offers less tunability in terms of adhesion energy and kinetics [7]. These two entanglement types display contrasting adhesion behaviors, allowing for pre-definable and spatially-varying adhesion on diverse surfaces. Thus, our study

provides an approach to embody multifaceted adhesion programmability into a hydrogel adhesive through a single design of the network structure. We refer to this approach as the topologically engineered adhesives (TEA), which offers a robust, facile, and predictive strategy for unprecedented control over hydrogel adhesion, and opens up numerous opportunities in engineering and medicine.

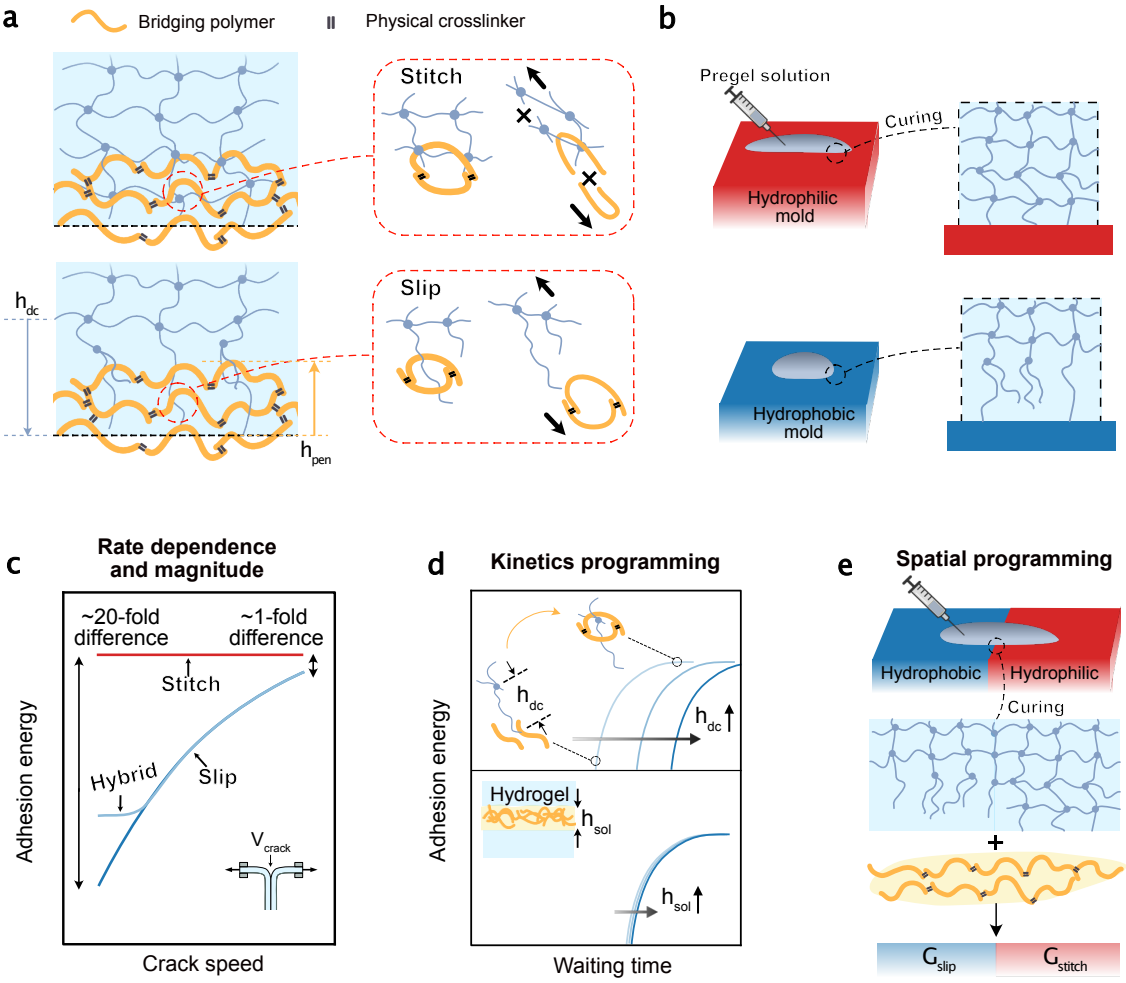

Fig. 4.1: Engineered network topology and linkages for multifaceted programming of hydrogel adhesion. (a) Schematics of the stitch linkage (Top) and slip linkage (Bottom) formed between a bridging polymer and networks without and with surface dangling chains. The thickness of the dangling chain layer and the penetration depth of the bridging polymer are denoted as h_{dc} and h_{pen}, respectively. (b) Hydrophilic and hydrophobic molds are used to form a regular network (Top) and a network carrying surface dangling chains (Bottom), respectively. (c) Rate dependence and magnitude of the adhesion energy depend on the interfacial linkage types: stitch linkages with $h_{\mathrm{pen}}/h_{\mathrm{dc}} \to \infty$, slip linkages with $h_{\mathrm{pen}}/h_{\mathrm{dc}} \ll 1$, and their hybrid with $h_{\mathrm{pen}}/h_{\mathrm{dc}} \approx 1$. (d) The slip linkage offers programmable adhesion kinetics through tuning h_{dc} (Top), which is also insensitive to processing conditions such as the thickness of bridging polymer solution h_{sol} (Bottom). (e) Spatially controllable adhesion obtained from patterning the topological linkages at the interface.

4.3 Results and Discussion

To robustly program hydrogel adhesion, we create a diffusive interface by placing a third species of diffusive polymer, called bridging polymer, to the interface between hydrogel

adhesives and targeted surfaces[7, 21]. Formation of the chain-to-network topology of the slip linkage demands the following conditions: (1) the hydrogel network needs to contain dangling chains and (2) a thermodynamic driving force is needed to facilitate the diffusion of bridging polymers into the gel network. Meanwhile, the diffusion needs to be halted once the linkage forms to prevent the over-diffusion of bridging polymers into the bulk gel, which may reduce the number of linkages at the interface.

To meet the first condition, we choose polyacrylamide (PAAm) as a model hydrogel network and polymerize it on a mold with low surface tension such as Poly(methyl methacrylate) (PMMA). The hydrophobicity and other associated effects inhibit the free-radical polymerization of the gel in the vicinity of the mold [22, 23, 24].This effect results in a surface layer of branched dangling chains with thickness h_{dc} ranging from ~ 10 to ~ 100 μm estimated using our experimental results (described later), "protruding" from the crosslinked bulk network. This estimation is in reasonable agreement with an early study [23] showing that a layer of much lower polymer content forms near the surface of Teflon mold during the polymerization of poly-2-acrylamide2-methyl-1-propanesulfonic acid (PAMSP) and poly-acrylic acid (PAAc). The low polymer content layer has a thickness spanning over $\sim 100\mu$m, which manifests as a dangling chain layer when the gel fully cures. In contrast, gels polymerized on molds with high surface tension such as glass are not subject to the hydrophobic mold effect, and hence contain crosslinked networks instead of branched dangling chains on their surfaces. The gels with and without engineered surface dangling chains are hereafter referred to as the TEA and regular gels, respectively. To meet the second criterion, stimuli-responsive polymers such as chitosan or gelatin were chosen as bridging polymers. The polarity of the hydrogel network and chitosan chains and the entropy of mixing promote the diffusion of chitosan chains into the hydrogel; meanwhile, the chitosan chains can be triggered to crosslink into a bridging network through a reaction-diffusion process in responding to pH changes, leading to penetration depths h_{pen} on the order of tens of microns [21]. Other strategies to form the chain-to-network topology of slip linkage at soft material interfaces are discussed in *SI Appendix* note 1.

4.3.1 Structural characterization

Based on the above principles, we fabricate a model TEA using single-network TEA gel made of PAAm and use chitosan as the bridging polymer. To probe the engagement length between the dangling chains and the bridging polymer chains, we used confocal microscopy to visualize how fluorescently labelled chitosan chains penetrate the TEA gel at equilibrium. The fluorescence intensities exponentially decrease from the outermost surface to the bulk of the

TEA gels with different crosslinker-to-monomer ratios C (colored dash lines, Fig 4.2a). For different C, we measured similar distances where the intensities meet the lower plateau (black dash line, Fig 4.2a), defining the penetration depth of the bridging polymer $h_{\text{pen}} \approx 70\mu m$. Note that h_{pen} may depend on the polydispersity of chitosan polymers (*SI Appendix* Fig S9). A systematic study with carefully controlled chitosan polymer molecular weight and C varied in a wide range is needed for a holistic investigation on the relation between the h_{pen} and C. Further, this value may also depends on the reaction-diffusion process and thus may vary with the type of bridging polymers. For instance, h_{pen} for gelatin is expected to be temperature-dependent.

To confirm the presence of the dangling chain layer in TEA gels, we utilized scanning electron microscopy (SEM) to examine a cryosectioned and dehydrated TEA gel sheet (100 μm thick, *SI Appendix* note 1 and Fig S3). The dehydrated TEA gel sheet exhibited more pronounced edge shrinkage compared to a regular gel sheet. This phenomenon is presumably due to the lower polymer content and crosslinking density near the edge then in the bulk, indicating the presence of the dangling chain layer near the surface of TEA gels. Since directly imaging the dangling chains is challenging, we made a first-order estimation of the thickness h_{dc} of the dangling chain layer from the experimentally measured elastic moduli. The TEA gel has a total thickness of h and is idealized with a tri-layer model (Fig 4.2b): a layer of a regular network is sandwiched by two layers of branched dangling chains. The elastic modulus of the sandwiched regular network E_{reg} can be measured from a regular hydrogel formed at the same conditions except using a hydrophilic mold, given their observed structural similarity [23, 24, 25]. The elastic modulus of the dangling chain layer is assumed to be negligible since it cannot carry any transverse loads. As such, we can estimate h_{dc} from the ratio of measured elastic moduli of the TEA and regular gels $E_{\text{tea}}/E_{\text{reg}}$ in uniaxial tensile tests (Fig 4.2c, *SI Appendix* note 1 and Fig. S1). We further perform micro-indentation test to ascertain the dangling chain layer thickness, and the results show reasonable agreement with the h_{dc} estimation from uniaxial tensile test if considering the non-zero compressible modulus of the branched dangling chains (SI *Appendix* note 1). The estimations of h_{dc} show a decreasing trend with the increasing value of C. The trend $h_{\text{dc}} \sim C^{-1}$ may be attributed to the competition between bulk elasticity of the gel network and interface tension during gelation on hydrophobic mold[22] (*SI Appendix* note 1), demonstrating a controlled method for fabricating the dangling chain layer of different sizes.

With the measured length scales, we calculate their ratio $h_{\text{pen}}/h_{\text{dc}}$ to quantify the extent to which the bridging polymers engage the dangling chains, which is expected to govern the formation of different topological linkages at the TEA gel interface (*SI Appendix* Fig. S4a).

When $h_{\text{pen}}/h_{\text{dc}} \ll 1$, the bridging network only engages a part of the dangling chain layer, so that the interface only comprises slip linkage. If $h_{\text{pen}}/h_{\text{dc}} \approx 1$, a complete engagement ensues which indicates that part of the bridging polymers may diffuse across the dangling chain layer to stitch the underlying network of the TEA gel. In this case, the linkage is expected to behave as the combination of the slip and stitch linkage and is referred to as the hybrid linkage (Fig 4.1c). Lastly, a regular hydrogel interface that only comprises stitch linkage corresponds to $h_{\text{pen}}/h_{\text{dc}} \to \infty$ since $h_{\text{dc}} \to 0$. Fig 4.2c shows $h_{\text{pen}}/h_{\text{dc}} \approx 0.2$ when $C = 0.024\%$ and increases to unity as C increases to 0.06% for the TEA gel interface. By tuning C, we can vary the degree of engagement and consequently the formation of different linkages, which will be shown later to modulate the resulting adhesion energy.

4.3.2 Interfaical topological linkages to program rate-dependent adhesion energy

To test our hypothesis, we first focus on two extremities: the interfaces containing either slip or stitch linkages. To form slip linkage-mediated adhesion, we adhere two TEA gels using chitosan as the bridging polymer with $h_{\text{pen}}/h_{\text{dc}} \approx 0.2$ ($C = 0.024\%$), followed by a T-peeling specimen to measure the adhesion energy G as a function of crack speed V_{crack} (*Methods*). Fig 4.2d shows that the slip linkage-mediated adhesion $G^{1/2}$ varies logarithmically with V_{crack}, the crack speed. We observed a factor of 25 in the change of G as V_{crack} varies by two decades. Together plotted in Fig 4.2d is the stitch linkage-mediated adhesion formed between two regular hydrogels for the same C and chitosan concentration c_{chi}, showing higher magnitude but much weaker rate-dependence. The contrast between slip and stitch adhesion is the most pronounced at low V_{crack} but diminishes at high V_{crack}. We also observed adhesive failure and mixed adhesive-cohesive failure at the slip and stitch linkage-mediated interfaces, repspectively. Our experiments further confirmed the similar bulk mechanics between the TEA and the regular gels: they both show minimal hysteresis in cyclic loadings and weak rate dependences, indicating near-perfect elasticity (*SI Appendix* Fig. S1a-b). The data suggest that different interfacial network topologies regulate hydrogel adhesion independent of the bulk properties.

These results motivate us to further analyze the data with a kinetic model proposed by Chaudhary [26]. The model considers the breaking of linkages as thermally activated processes [26, 27, 28, 29], and treats each linkage as a linear spring with stiffness k_{i} and an activation energy of dissociation E_{i} (i can be slip or stitch). These parameters influence the dissociation rates of the linkages (Fig 4.2e), and consequently the rate-dependence of the

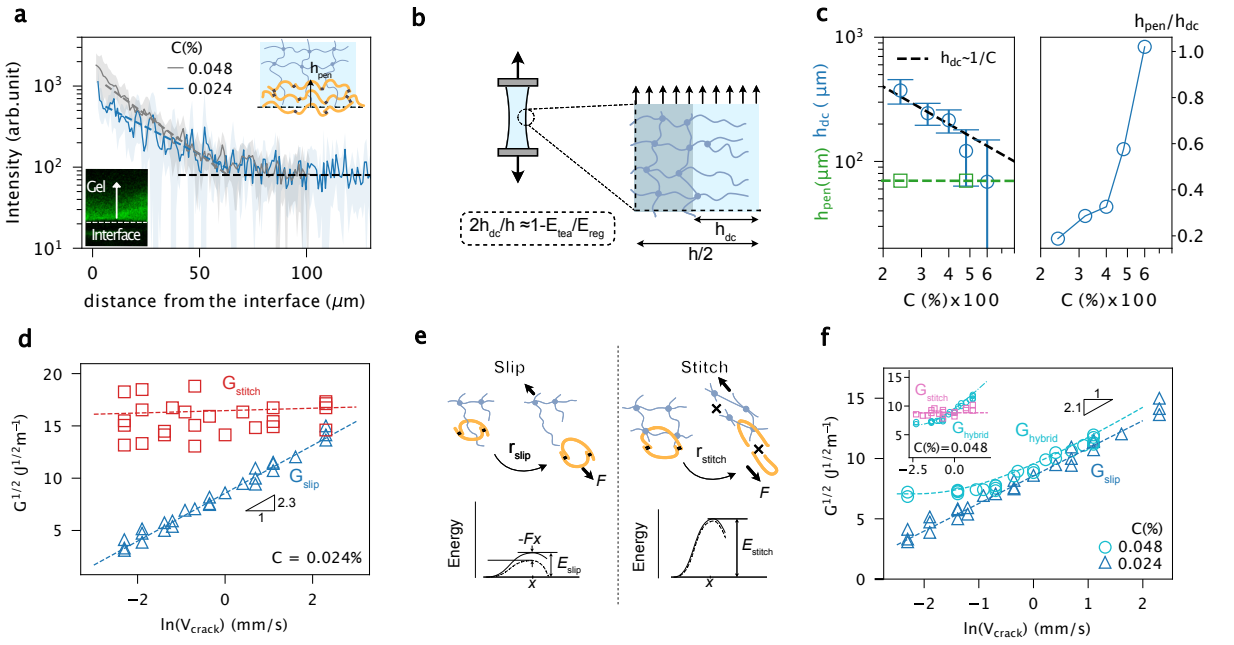

Fig. 4.2: Design and characterization of topology-engineered adhesive (TEA). (a) Intensities of florescent chitosan chains diffused in TEA gels. The shaded area represents the standard deviation from 5 measures. The stronger chitosan intensity for higher C may be due to more chitosan chains trapped by the denser dangling chains on the interface. (b) An idealized model used to estimate the thickness of branched dangling chain layer. (c) Left panel: estimated h_{dc} and measured h_{pen} as functions of the crosslinker-to-monomer ratio C. Error bars represent standard deviation. Right panel: relative engagement length $h_{\mathrm{pen}}/h_{\mathrm{dc}}$ as a function of C. **Dissimilar topological linkages lead to contrasting adhesion behaviors.** (d) Slip and stitch linkages-mediated $G^{1/2}$ plotted as functions of $\ln(V_{\mathrm{crack}})$ for $C = 0.024\%$ and $c_{chi} = 2\%$ g/mL. (e) Illustration showing the dissociations of slip and stitch linkages as thermally activated processes, with reaction rate of dissociation r_i (i can be slip or stitch). Upon a separation force F, the activation energy of the linkage is decreased by $-Fx$, where x is the seperation distance. (f) The formation of topological linkages and the resulting adhesion depend on $h_{\mathrm{pen}}/h_{\mathrm{dc}}$, which is controlled by C. Slip and hybrid linkages are achieved for TEA gels with $C = 0.024\%$ and 0.048%, respectively. The inset shows the same curves as (d) but for $C = 0.048\%$.

hydrogel adhesion energy. As detailed in *SI Appendix* note 2, the model states the adhesion energy for linkage i relates to the crack speed via $G^{1/2} \sim \ln V_{\mathrm{crack}}$, which agrees perfectly with our experimental data for the slip linkage-mediated adhesion (blue dash lines in Fig 4.2d). Further, the model shows that the slope of the linear relation scales inversely to $k_i^{1/2}$, while the intercept depends on E_i. By fitting this model to our data we were able to determine k_i and E_i, which are otherwise difficult to characterize directly. Specifically, we found $k_{\mathrm{slip}} = 1.7 \times 10^{-7}$ N/m and $E_{\mathrm{slip}} = 75$ kJ/mole for the slip linkage with $C = 0.024\%$ and $h_{\mathrm{pen}}/h_{\mathrm{dc}} \approx 0.2$. It is plausible that the hydrogel dangling chains that determine k_{slip} is of entropic type, so that $k_{\mathrm{slip}} = 3k_BT/R^2$ with k_BT the energy in temperature and R

the average end-to-end distance of the dangling chains. The model allows us to estimate $R \approx 250$ nm with the fitted value of k_{slip}, which is 50 times larger than the mesh size of the underlying network $\xi \approx 5$ nm (SI *Appendix* note 1). The fitted value of E_{slip} is larger than the typical activation energy of hydrogen bond (4-50 kJ/mole), suggesting potential synergistic contributions of multiple hydrogen bonds (between chitosan and PAAm) to a single slip linkage. Besides, the model captures the rate-insensitivity of $G^{1/2}_{\text{stitch}}$ of the stitch linkage with $k_{\text{stitch}} \gtrapprox 300 k_{\text{slip}}$ and $E_{\text{stitch}} \approx 185$ kJ/mole (red dash line, Fig 4.2d). The much larger k_{stitch} may be due to the full extension of the entangled networks prior to network rupture, driving the polymer chains far beyond the entropic limit. The estimation of E_{stitch} is in the range of the bond energy of the C-C bond (350 kJ/mole) [30] and the theoretically estimated energy stored in each bond prior to rupture using molecular parameters (60 kJ/mole)[31], in line with the assumption that the stitched networks must rupture during separation. This model reveals quantitatively that the slip linkages exhibit much lower stiffness and dissociation energy compared to those of stitch linkages.

Additionally, the model predicts that the hybrid linkage formed when $h_{\text{pen}}/h_{\text{dc}}$ is close to 1, would impart tunable dependence on loading rate through the relation $G_{\text{hybrid}} = G_{\text{slip}} + G_{\text{stitch}}$. In this case, $G^{1/2}_{\text{hybrid}}$ is predicted to be a nonlinear function of $\ln V_{\text{crack}}$ with a finite and constant value of G_{stitch} (Fig 4.1c), indicating that the hybrid linkage behaves as slip or stitch linkage respectively in different ranges of loading rates. To test the hypothesis, we prepared TEA gels with $h_{\text{pen}}/h_{\text{dc}} \approx 0.6$ ($C = 0.048\%$, Fig 4.2c), and the resulting $G^{1/2}$ shows a nonlinear trend as expected: at high crack speed, the data collapses onto a master curve with that with $h_{\text{pen}}/h_{\text{dc}} \approx 0.2$ ($C = 0.024\%$), following $G^{1/2}_{\text{slip}} \sim \ln V_{\text{crack}}$ (Fig 4.2f). Note that in this regime, the slip linkage-mediated adhesion is higher than that mediated by stitch linkage for the same C between two regular gels (Fig 4.2f inset). Below V_{crack}=0.5mm/s, the data converges to a plateau corresponding to rate-independent adhesion energy of ~ 50 Jm^{-2}. This baseline adhesion is also close to the value of G_{stitch} for the same C ($\sim$60 Jm^{-2}, Fig 4.2f inset), confirming the co-existence of stitch- and slip-linkages on the interface. Fixing G_{stitch} = 50 Jm^{-2}, our model captures the experimentally measured $G^{1/2}_{\text{hybrid}}$ with fitting parameters $k_{\text{slip}} = 1 \times 10^{-7}$ N/m and $E_{\text{slip}} = 71$ kJ/mole (Fig 4.2f, cyan dot line), closed to the values of the sample with $h_{\text{pen}}/h_{\text{dc}} \approx 0.2$ ($C = 0.024\%$). The ability to control the formation of linkage by tuning the entanglement length between TEA gel and bridging polymers offers a high level of adhesion programmability: not only can we predictably tune the adhesion energy by varying loading rates, but also program rate dependence in different ranges of loading rate. The finite adhesion energy at low loading rates provided by the hybrid linkage can effectively prevent the adhesive from failing at static load to ensure good durability.

4.3.3 Programming adhesion kinetics

In addition to the equilibrium state of adhesion, we next demonstrate that the association of the topological linkages regulates the transient adhesion, which can be exploited to encode adhesion kinetics (Fig 4.1d). When the bridging polymer solution is placed between the hydrogel and a permeable substrate, they diffuse into the two networks while simultaneously crosslinking into a bridging network in response to a trigger. The reaction-diffusion process comprises two concurrent sub-processes: the gelation and the diffusion of the bridging polymer with their kinetic time t_{gel} and t_{d}, respectively. We assume that the overall adhesion kinetics is governed by the slower sub-kinetics: $t \equiv \max\{t_{\text{d}}, t_{\text{gel}}\}$.

When using chitosan as the bridging polymer, the gelation process is due to the decrease of pH, which is associated with the diffusion of gelling trigger (protons) away from the cast adhesive solution. The thickness of the solution h_{sol} sets the critical diffusion length, and thus its kinetics time follows $t_{\text{gel}} \sim h_{\text{sol}}^2/D_{\text{eff,gel}}$ [32] where $D_{\text{eff,gel}}$ is the effective diffusion coefficient of the gelling trigger. However, h_{sol} is sensitive to the applied compression or wettability of the interface, yielding the gelation kinetics uncertain in practice without carefully controlled h_{sol}.

In contrast, the diffusion process of bridging polymers depends on the value of h_{dc}, and hence the type of formed linkages. For a regular gel, $h_{\text{dc}} \to 0$, the interface is dominated by stitch linkages which only require the bridging polymer to diffuse by one mesh size of the gel network, thus taking negligible kinetic time $t_{\text{d}} \approx 0$ s [32]. As such, one can expect the adhesion kinetics of the regular hydrogel interface to be limited by t_{gel}, which is difficult to control in practice due to the variable h_{sol}. We hypothesize that incorporation of slip or hybrid linkages can resolve the issue. In this case, the formation of the linkages requires the bridging polymers to diffuse through the dangling chains layer (Fig 4.3a), and h_{dc} sets the characteristic diffusion length scale which yields $t_{\text{d}} \sim h_{\text{dc}}^2/D_{\text{eff}}$ where D_{eff} is the effective diffusion coefficient of the bridging polymers. The prolonged diffusion process can bypass the uncertain gelation process to govern the overall adhesion kinetics. Importantly, since h_{dc} is a material property, it can render the overall adhesion kinetics insensitive to processing or environmental conditions.

To test the hypothesis, we characterized the adhesion kinetics with different values of h_{sol} (50 and 120 μm) controlled by nylon meshes of different thicknesses[32] (Methods and *SI Appendix* Fig. S6). We define the adhesion kinetics using the half time $t_{1/2}$ when G reaches half of the equilibrium state value G_{eq}. For the regular gel interface, we observe a strong h_{sol}-dependent adhesion kinetics, and the associated kinetic time follows $t_{1/2} \sim h_{\text{sol}}^2$ (Fig 4.3b and inset). On the contrary, we observe that the adhesion kinetics of the TEA gel interface

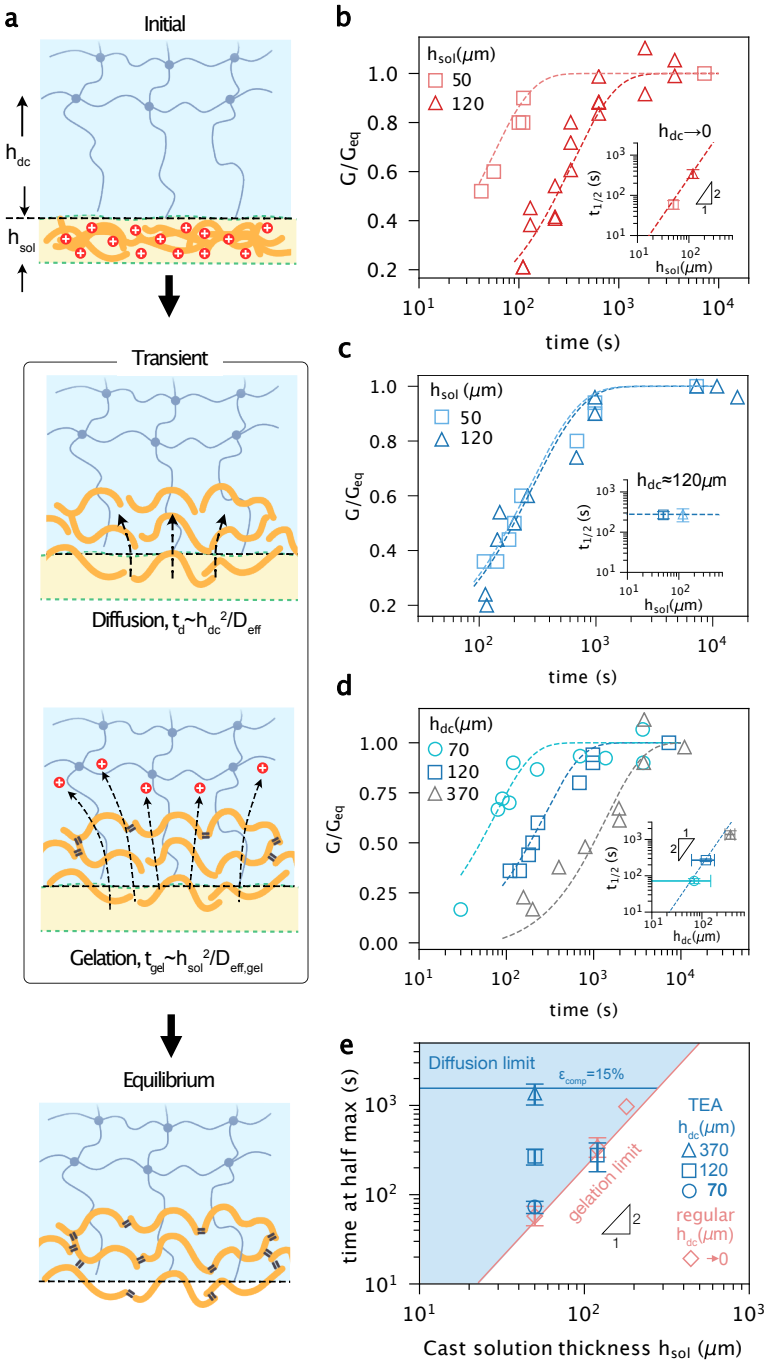

Fig. 4.3: Programmable adhesion kinetics of TEA.(a) Illustrations showing that the total adhesion kinetics comprises two sub-kinetic processes: diffusion and gelation. (b) Dimensionless adhesion between two regular hydrogels G/G_{eq} with $G_{\mathrm{eq}} = 49.98\mathrm{Jm}^{-2}$ and $47.42\mathrm{Jm}^{-2}$, as functions of waiting time for cast solution thicknesses $h_{\mathrm{sol}} = 50\mu m$ and $120\mu m$, respectively. The inset shows $t_{1/2}$ as a function of h_{sol}. Error bars represent 95% confidence intervals from fitting the exponential function. (c) Similar curves as (b) measured at the interface between two TEA gels with $h_{\mathrm{dc}} \approx 120\mu m$. $G_{\mathrm{eq}} = 48.10\mathrm{Jm}^{-2}$ and $47.4\mathrm{Jm}^{-2}$ for $h_{\mathrm{sol}} = 50\mu m$ and $120\mu m$, respectively. (d) Adhesion kinetics of TEA interfaces with fixed h_{sol} ($50\mu m$) and varying values of h_{dc} ($h_{\mathrm{dc}} \approx 370, 120, 70\mu m$, achieved using $C = 0.024\%$, 0.048%, and 0.06%, respectively). $G_{\mathrm{eq}} = 76.37\mathrm{Jm}^{-2}$, $48.10\mathrm{Jm}^{-2}$ and $28.78\mathrm{Jm}^{-2}$, for $h_{\mathrm{dc}} \approx 370, 120, 70\mu m$, respectively. The inset shows $t_{1/2}$ as a function of h_{dc}. The y error bars represent a 95% confidence interval from fitting an exponential function while the x error bars represent the standard deviation from 3 measures. (e) $t_{1/2}$ for regular ($h_{\mathrm{dc}} \to 0$) and TEA gels (varying h_{dc}) plotted as functions of h_{sol}. The blue horizontal line of corresponds to the TEA gel subject to an instantaneous compression of 15% strain without thickness-defining mesh (*SI Appendix* Fig S6c). The red diamond at $h_{\mathrm{sol}} = 180\mu m$ is adapted from reference [32].

with $h_{dc} \approx 120\mu m$ ($C = 0.048\%$) is insensitive to the value of h_{sol} (Fig 4.3c and inset). Our point is further strengthened by applying an initial compression (15% strain) to the TEA gel interface ($h_{dc} \approx 370\mu m$) without controlling h_{sol}, which yields the same adhesion kinetics as the TEA gel interface with controlled h_{sol} (*SI Appendix* Fig. S6c). Thus, incorporation of the engineered dangling chain layer leads to adhesion kinetics insensitive to processing conditions, validating our hypothesis.

Importantly, not only is the TEA kinetics insensitive to processing conditions, but also it is controllable through changing h_{dc}. Fixing h_{sol}, we observed strong h_{dc}-dependent adhesion kinetics of the TEA gel interface: the kinetics accelerates as h_{dc} decreases, suggesting shorter distance that the bridging polymers need to diffuse across to form hybrid or slip linkages (Fig 4.3d). The half time follows $t_{1/2} \sim h_{dc}^2$ at $h_{dc} \approx 70$ and 120 μm. Fitting of the scaling relation to the data at these two h_{dc} values yields $D_{eff} \approx 0.5 \times 10^{-12} m^2 s^{-1}$, agreeing reasonably well with the value predicted by Rouse model (Fig 4.3d inset, *SI Appendix* note 3). Our data, however, deviates from the scaling relation at $h_{dc} \approx 370$ μm (Fig 4.3d inset). In the last case, the kinetics time is presumably bounded by the total diffusion-reaction time since $h_{pen}/h_{dc} \ll 1$, indicating that the underlying crosslinked network of the TEA gel is beyond the reach of bridging polymers.

Next, we discuss the role of each sub-kinetic process in determining the overall kinetics of TEA adhesion (Fig 4.3e). In principle, the overall adhesion kinetics is a function of two key parameters: h_{dc} and h_{sol}, which govern the two sub-kinetics t_d and t_{gel}, respectively, i.e., $t_{1/2} \equiv \max\{t_d(h_{dc}), t_{gel}(h_{sol})\}$. A simple scaling analysis allows determination of the critical condition at which the limiting kinetic mechanisms switch: $h_{dc}^2 D_{eff,gel}/h_{sol}^2 D_{eff} = 1$. Taking $D_{eff,gel} \approx 10^{-11}$ m^2 s^{-1} [32] and using the estimated value of $D_{eff} \approx 5 \cdot 10^{-12}$ m^2 s^{-1} lead to $h_{dc} \approx h_{sol}$. When $h_{dc} \gg h_{sol}$ (the blue regime of Fig 4.3e), $t_d \gg t_{gel}$, so that the $t_{1/2}$ of TEA gel is solely dependent on h_{dc} through $t_{1/2} \equiv t_d \sim h_{dc}^2/D_{eff}$. This allows us to tune the adhesion kinetics by varying h_{dc}. On the other hand when $h_{dc} < h_{sol}$, the limiting kinetic mechanism switches due to $t_d < t_{gel}$, so that the adhesion kinetics is tunable by varying h_{sol} through $t_{1/2} \equiv t_{gel} \sim h_{sol}^2/D_{eff,gel}$. Therefore, the adhesion kinetics of the regular gels can be considered as a special case of TEA gels in the limit of $h_{dc} \to 0$, where the dominating kinetic mechanism is the gelation of the bridging polymers (indicated by the red line in Fig 4.3e). The programmable TEA kinetics and can be tailored to suit different applications. For instance, a small h_{dc} can be used with compression to achieve fast kinetics for hemostatic applications [33], while a large h_{dc} provides a sufficient and adjustable time window for adhesive placement.

We further note that h_{dc} in this study is reduced by increasing C, which tends to embrittle

the bulk and hence reducing the equilibrium adhesion energy G_{eq} of the TEA gel (Fig 4.3d). For certain applications that demand both fast and strong adhesion, one could vary h_{dc} independently of C by polymerizing gels on molds with different hydrophobicity. This approach could enable the tuning of adhesion kinetics without changing G_{eq}. As a proof of concept, we demonstrate that a regular hydrogel, polymerized on a hydrophilic mold, contains negligible dangling chain layer $h_{dc} \to 0$ regardless of the value of C. Thus, a regular gel with relatively low crosslinking density $C = 0.024\%$ shows both fast adhesion kinetics ($\sim$70s with $h_{\mathrm{sol}} = 50\mu$m) and high G_{eq} (200 Jm^{-2}) due to the combination of small h_{dc} and small C (*SI Appendix* Fig S6d). This strategy enables the formation of fast and strong adhesion simultaneously.

4.3.4 Universal applicability

The design and fabrication of TEA are universally applicable to a wide range of material systems, including various bridging polymers, targeted substrates, and TEA networks (Fig 4.4a). We first examine a different bridging polymer gelatin in addition to chitosan. Gelatin was prepared as polymer solution at $37°C$ and then applied to the interface between two TEA gels for $C = 0.024\%$ at room temperature. Similar to chitosan, gelatin diffused into the gel and was crosslinked into a bridging network in responding to a temperature drop to form slip linkages with the TEA dangling chains. Our data reveals an identical trend between the data obtained using gelatin and chitosan as bridging polymers (Fig 4.4b), highlighting the dominating role of polymer topology rather than material chemistry in the formation of slip linkages.

Second, slip linkages formed at the gel-bridging network interface can be coupled with other interactions that the bridging network can interact with the targeted substrates, such as slip, stitch linkages or covalent bonds [34]. For instance, the triggered crosslinking and the abundant amino groups of chitosan chains provide numerous options to interact with diverse substrates through stitch linkage or covalent bonds[35]. Based on the principle, slip-slip, slip-stitch, and slip-bond linkages were achieved between two TEA gels, between a TEA and a regular gel, and between a TEA gel and a VHB elastomer, respectively (*SI Appendix* Table S1). Our data reasonably collapse for the three linkage types to engage different targeted substrates (Fig 4.4c), suggesting that the overall adhesion behavior is dictated by the slip linkages while depending less on the types of interactions between the bridging network and targeted substrates. Without the slip linkage, the adhesion between two regular PAAm gels (stitch-stitch) and between a regular PAAm gel and a VHB elastomer (stitch-bond) show much less rate-dependence and higher magnitude (Fig 4.4C). These results validate the

robustness of adhesion programming through the TEA strategy.

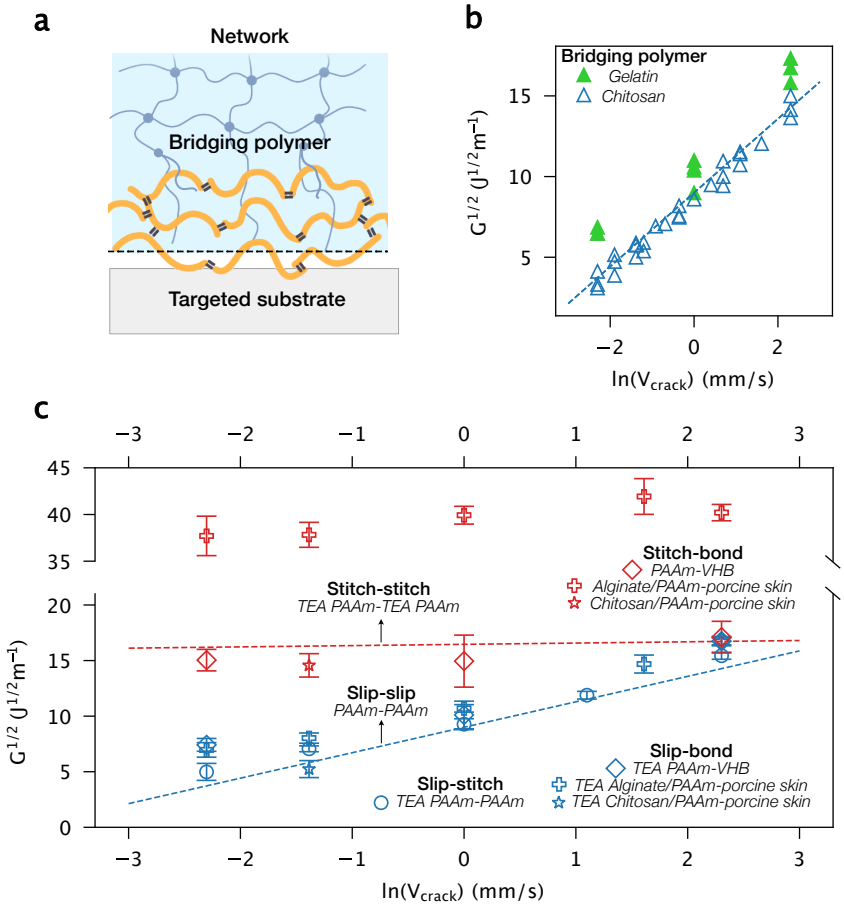

Fig. 4.4: Universal applicability of the TEA strategy. (a) Schematic showing that a TEA interface can be constituted by a variety of materials. (b) Slip-slip linage mediated adhesion between two TEA gels using gelatin and chitosan as bridging polymers. $c_{\text{chi}} = c_{\text{gelatin}} = 2\%$ g/ml (c) Topological linkages dictate hydrogel adhesion behaviors. The interfaces containing the slip linkage follow $G^{1/2} \sim \ln V_{\text{crack}}$, and the adhesion shows stronger rate-dependence compared to those not containing the slip linkage. The red and blue dash lines correspond to the stitch-stitch and slip-slip-mediated adhesion in Fig 2d, respectively. The bridging polymer is chitosan with $c_{\text{chi}} = 2\%$ g/ml. The TEA gels have crosslinker density $C = 0.024\%$. The constituents of different topological linkages are listed in Table S1.

Lastly, we explore using double-network (DN) hydrogel as the TEA network, which exhibit much higher fracture toughness and adhesion [5, 21, 36, 37] due to background dissipation compared to single-network (SN) hydrogels. We tested alginate/PAAm and chitosan/PAAm hydrogels as representative materials. In both types of DN gels, alginate and chitosan are physically crosslinked macromolecules and do not covalently interfere with the PAAm network, we expect that the hydrophobic mold could produce surface dangling chains in

the PAAm network within the DN gels. We confirmed the presence of the dangling chain layer in the surface of a alginate/PAAm hydrogel polymerized on hydrophobic substrate by EDTA treatment to remove calcium-alginate bonds followed by Atomic Force Microscopy (AFM) tests (*SI Appendix* Fig. S7a,b). We then examined the adhesion of TEA and regular DN gels that respectively polymerized on PMMA and glass molds on porcine skin (for a systematic study on different gelling molds, see *SI Appendix* Fig. S7c). We use chitosan as the bridging polymer and EDC/NHS reagent to form covalent bonds between chitosan and tissue surfaces [21]. Our data show that the adhesion of TEA alginate/PAAm gels on porcine skins (slip-bond) also follows $G^{1/2} \sim \ln V_{\text{crack}}$, with similar slope to those of SN TEA gels (slip-slip, slip-stitch, and slip-bond) (Fig. 4.4c). In contrast, the adhesion between regular algiante/PAAm gels and porcine skins (stitch-bond) show much higher adhesion energy with less rate-dependence within the tested range of crack speed. Further investigations were conducted with TEA chitosan/PAAm gels on porcine skins (slip-bond) at $V_{\text{crack}} = 0.25$mm/s, also agreeing with those of SN TEA gels. In comparison, the adhesion between regular chitosan/PAAm gels and porcine skins (stitch-bond) is almost 10-fold higher [37] than the TEA counterpart, consistent with the adhesion of SN regular gels (Fig. 4.4c). The results demonstrate that our methodology is not only applicable to SN hydrogels but also DN hydrogels as long as the topology of one of the networks can be engineered.

4.3.5 Programming spatial adhesion

The contrast between slip and stitch linkages allows us to program the adhesion spatially. To do so, we patterned a mold substrate with hydrophilic (Glass) and hydrophobic regions (PTFE films thickness ∼0.1mm), followed by polymerizing a TEA gel on the patterned mold (*SI Appendix* Fig. S7d). While the unequal thicknesses of the hydrophilic and hydrophobic regions can influence the flatness of the resulting gel, we performed a separate experiment with varying thickness mismatch between the hydrophilic and hydrophobic regions (± 0.1mm) to confirm that the flatness does not affect the adhesion selectivity (*SI Appendix* Fig. S7e). Given the predefined geometries (circle, triangle) of the hydrophobic domains, we can design the dangling chain region where weak adhesion G_{slip} is formed at low loading rates; meanwhile, strong adhesion G_{stitch} is formed in other areas to sustain tension or twisting applied to the interface without interface debonding. Fig 4.5a and *SI Appendix* Fig. S7f show that by shaping the dangling chain region, we can achieve weak adhesion region of complex shapes between a TEA gel and a regular gel by slowly injecting liquid dye into the weak interface. To further characterize the resolution of the spatially programmable adhesion, we made a series of circular islands of nominal radii r_{nominal} in which slip linkages are formed. By slowly

injecting the liquid dye, we visualized and measured their radii r_{measure} of the weak adhesion region using a digital camera (Fig. 4.5b). The excellent agreement between the nominal and measured radii suggests high spatial resolution ∼0.1 mm achieved with a manual procedure. Moreover, the one-step fabrication allows spatially heterogeneous adhesion to be assembled within a piece of monolithic hydrogel, which otherwise requires assembling different materials at the interface. This could be conducted beforehand and using 3D-shaped substrates for curved adhesive surface. It is beneficial when soft, wet, and curved biological tissues are involved, as the hydrogel interface is inherently soft and mechanically compatible with such tissues. There exist other strategies such as selective masking for creating spatial heterogeneity in adhesion [13, 14, 15]. Selective masking is a facile approach, but its implementation may involve the placement of masking materials, often made of rigid polymer films, which could be complicated by the mechanical mismatch and unwanted adhesion on soft, wet, rough and curved substrates such as biological tissues. Furthermore, substrate patterning procedures are time-consuming and may not suit time-sensitive scenarios such as surgical applications. In contrast, our method directly encodes the patterned adhesion into the soft and deformable hydrogel interface [38, 39], thereby alleviating the need for masking materials.

As the slip and stitch linkages show different sensitivities to loading rate, we expect the spatially selective adhesion, characterized by the adhesion energy contrast $G_{\text{slip}}/G_{\text{stitch}}$, to be also rate-dependent. Fig. 4.5c shows that $G_{\text{slip}}/G_{\text{stitch}}$ predicted by the parameterized model (*SI Appendix* note 2) approaches unity at high V_{crack} and decreases towards zero at low V_{crack}. The prediction is supported by our experimental observations: A TEA gel with the designed dangling chain region shows large adhesion contrast to a regular gel at low V_{crack}, while the interface appears to be uniformly adhesive at relatively larger V_{crack} (Fig. 4.5d). The rate-dependent spatially-programmable adhesion can potentially enable applications which desire tunable adhesion contrast in different regions under different loading rates. Additionally, not only we can achieve reduced adhesion ($G_{\text{slip}}/G_{\text{stitch}} < 1$) but also enhanced adhesion ($G_{\text{hybrid}}/G_{\text{stitch}} > 1$) in the engineered dangling chain region at large V_{crack} (*SI Appendix* Fig. S4b). In this case, the slip linkage acts as a toughener that synergistically contributes to the adhesion unit with the stitch linkage.

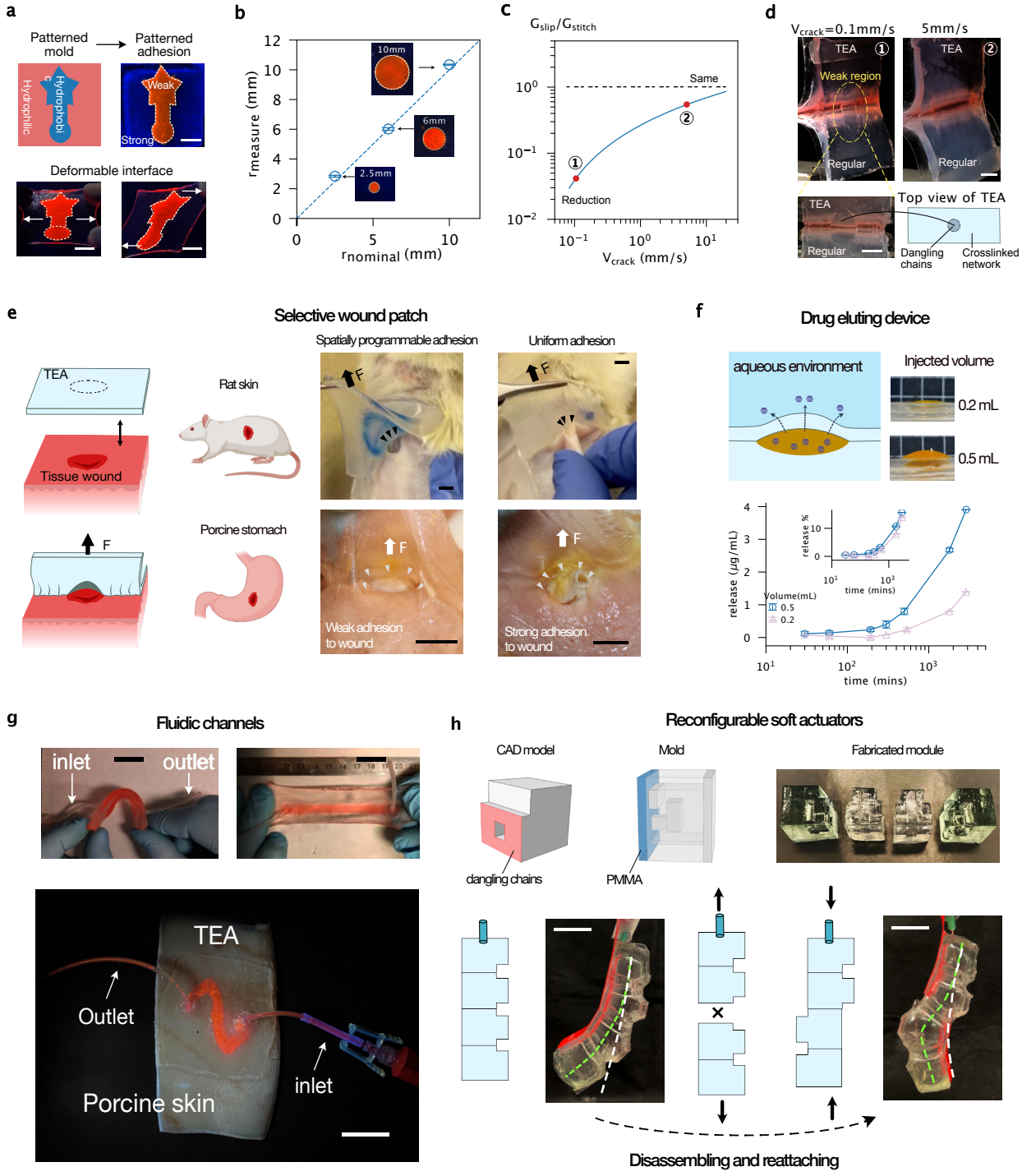
a
Patterned mold
Patterned adhesion
Hydrophilic
Hydrophobic
Weak
Strong
Deformable interface
b
10mm
6mm
2.5mm
rmeasure (mm)
rnominal (mm)
c
Gslip/Gstitch
Same
Reduction
Vcrack (mm/s)
d
Vcrack=0.1mm/s
5mm/s
TEA
Weak region
Regular
Top view of TEA
Dangling chains
Crosslinked network
e
Selective wound patch
TEA
Tissue wound
F
Rat skin
Porcine stomach
Spatially programmable adhesion
Uniform adhesion
Weak adhesion to wound
Strong adhesion to wound
f
Drug eluting device
aqueous environment
Injected volume
0.2 mL
0.5 mL
release (μg/mL)
release %
time (mins)
Volume(mL)
0.5
0.2
g
Fluidic channels
inlet
outlet
TEA
Outlet
inlet
Porcine skin
h
Reconfigurable soft actuators
CAD model
Mold
Fabricated module
dangling chains
PMMA
Disassembling and reattaching

Fig. 4.5: Spatial programming and soft devices enabled with TEA (a) TEA strategy enables spatially programmable and deformable adhesion between a TEA alginate/PAAm gel and a regular alginate/PAAm gel. The patterned adhesion is visualized by slow injection of liquid dye into the weak interface. Scale bar: 1cm. (b) Spatial resolution of the spatially programmable adhesion. (c) Predicated adhesion energy contrast $G_{\text{slip}}/G_{\text{stitch}}$ achieved using the parameterized model (*SI Appendix* Eqn. S14) using the data of G_{slip} and G_{stitch} in Fig 4.2d. (d) Experimental demonstration of the rate-dependent $G_{\text{slip}}/G_{\text{stitch}}$ between a SN TEA gel with a circular-shaped dangling chain region and a SN regular gel. Scale bar: 1cm. (e) Wound patches made of TEA and regular alginate/PAAm gels adhered to wounds on rat skin (top, scale bar: 8mm) and porcine stomach (bot, scale bar: 12mm). (f) A drug-eluding device enabled by injecting drug into the weakly-adhered interface between a SN TEA gel and a SN regular gel. Grid size of the inset: 10mm. (g) Deformable hydrogel-based fluidic channels created by adhering a TEA alginate/PAAm gel to a regular alginate/PAAm gel. Scale bars: 2cm. (Bottom) A TEA alginate/PAAm gel with designed adhesion selectivity forms a fluid channel on the surface of a porcine skin. Scale bar: 2.5cm. (h) Reconfigurable soft actuators. (Top) the fabrication process of the actuator units with connection surfaces composed of dangling chains. (Bottom) two modes of actuation. The initial and the actuated stages are indicated by the white and green dash lines, respectively. Scale bars: 2cm.

4.3.6 TEA-based devices

The programmable adhesion of TEA enables various applications such as wound patches, drug depots, fluidic channels, and soft actuators. For the application of wound patches, TEA allows for programming weak adhesion to wound beds while maintaining strong adhesion to the surrounding healthy tissue. As such, the patch could protect the wound without impairing tissue regeneration and wound closure. Using the one-step fabrication process (Fig 4.1e and *SI Appendix* Fig. S7d), we prepared such a TEA gel with its surface composed of a circular region of dangling chains and the surrounding region of crosslinked network. The dangling chain region forms slip linkages which attach weakly to the wound site upon slow removal to minimize the damage to the wound. Meanwhile, the stitch linkages attach strongly to the surrounding healthy tissue to maintain the stickiness of the patch. In contrast, a regular hydrogel exerts strong and uniform adhesion to both wounded and healthy tissues, which ruptures the wound bed upon removal (Fig 4.5e).

Besides, the creation of a weak adhesion region between two hydrogels could serve as a drug depot. Upon slow injection, mock drug solution filled up the weak interface. Further injection created a bulge of hydrogel to accommodate a high amount of drug, which can be continuously released through the hydrogel network when the whole device is immersed in an aqueous environment (Fig. 4.5f Top). Our data show that the initial amount of drug injected into the depot affects the amount of release over time but the relative kinetics of release remains similar (Fig. 4.5f Bottom). As well, we can create a drug depot above a wound site, where drugs can be directly released into wounded tissue. In contrast, the strong adhesion of

a regular hydrogel prevents the injection of drug solution to interface (*SI Appendix* Fig. S7g).

We then demonstrate hydrogel-based fluidic devices assembled with TEA. A PAAm-alginate TEA DN gel with a rectangular-shaped dangling chain region forms a partially weak interface with a regular DN gel, which subsequently becomes a fluidic channel upon slow injection of liquids. The resulting device is highly deformable while no liquid leakage is observed (Fig 4.5g Top). The one-step fabrication technique provides a simple approach to fabricate hydrogel fluidic channels compared with conventional methods that typically involve multiple molding steps [40, 41]. In addition, the spatially programmable adhesion is applicable to varying surfaces as it requires no patterning of the targeted substrate. As such, we can form such a fluid channel directly on tissue surfaces such as porcine skin (Fig 4.5g Bottom). This feature could benefit medical devices that contact with tissue surfaces for sustained drug release [42], or in-*vitro* organ-on-chip models to study cellular behaviors [43].

Lastly, we show that the TEA made of SN PAAm hydrogels can be used to construct reconfigurable soft actuators, featuring minimal bulk dissipation for efficient actuation and dynamic adhesion for reversible attachment (Fig 4.5h). Such actuators are formed with hydrogel units that contain surface dangling chains on each face and are connected to each other with the aid of bridging polymer (Methods). The slip linkage-mediated adhesion between the units is strong enough to sustain actuation, and yet can be separated easily and slowly with a small force. The separated units can then be reconnected upon reapplying the bridging polymer solution to the interface so that one can modify configurations of assembly for different actuation. Our data shows that the slip linkage-mediated adhesion increases and reaches a plateau after cycles of detachment and reattachment (*SI Appendix* Fig. S5d). This property can be partially attributed to the fact that the dissociation of the slip linkage only involves chain slippage, hence not rupturing the adherend networks (*SI Appendix* Fig. S5e). Thus, the slip-mediated TEA interface is inherently subjected to minimal damage compared with those bonded by stitch linkages or covalent bonds.

4.4 Conclusion

In summary, we have demonstrated that designing the interfacial network topologies of hydrogels provides a facile and robust approach to program adhesion in multiple aspects including magnitude, space, and kinetics. Our approach can be potentially extended to different length scales using proper manufacturing processes. For instance, spatially programmable adhesion with a spatial resolution on the micro-scale can be achieved with microfabrication of the hydrogel network topology [44, 45], while that on the metre scale is

expected to be achieved using gelling molds of the same size for applications such as camouflaging skin [46]. Broadly, our methodology falls into the emerging paradigm of material intelligence, as the adhesion programming is directly encoded in the hydrogel network as material properties, similar to other properties such as elastic modulus. The implementation of adhesion control requires no external apparatus, making the methodology extremely facile, robust, and scalable. We hope that the design of TEA can spark interest in controlling hydrogel adhesion by designing their network topologies, opening the door to a new design space for intelligent materials/structures through programmable adhesion.

Materials

All chemicals were purchased and used without further purification. Materials for the hydrogel synthesis and the bridging polymer include acrylamide (AAm, Sigma-Aldrich, A9099), N,N'-methylenebisacrylamide (MBAA; Sigma-Aldrich, M7279), ammonium persulphate (APS, Sigma-Aldrich, A3678), N,N,N',N'-tetramethylethylenediamine (TEMED, Sigma-Aldrich, T7024), Alginate (I-1G) was purchased from KIMICA Corporation, chitosan (degree of deacetylation, DDA: 95%, medium and high molecular weight, Lyphar Biotech), sodium bicarbonate (Fisher Scientific, S233), sodium phosphate monobasic (NaH2PO4, Sigma, S8282), sodium phosphate dibasic (Na2HPO4, Sigma-Aldrich, S7907), acetic acid (Sigma-Aldrich, A6283), calcium sulfate (Sigma-Aldrich), N-hydroxysulfosuccinimide (NHS, Sigma-Aldrich, 130672), and 1-ethyl-3-(3-dimethylaminopropyl) carbodiimide (EDC, Sigma-Aldrich, 03450), Gelatin (Sigma-Aldrich, G2500). Glass, acrylic sheets (PMMA), PS, silicon, and PTFE were purchased from McMaster-Carr to make mold substrates for polymerization. VHB elastomer was purchased from 3M. Porcine skin was purchased from a local grocery store, then stored in a fridge at -20°C, and thawed at 4°C before use. Nylon mesh were purchased from McMaster Carr without further modification (9318T25, 9318T23 for thicknesses of 50 μm and 120 μm, respectively.)

Synthesis of TEA

The single network PAAm TEA gels were prepared as follows. AAm monomers of 6.76 g was first dissolved in 50 mL of deionized water. After degassing, the AAm solution of 25 ml was mixed with varying amounts of MBAA aqueous solution (0.02 g mL^{-1}) and 20 μL of TEMED in a syringe. The volumes of MBAA solution added were 90, 120, 150, 180, and 240 μL for the crosslinker−to−monomer molar ratios C at 0.024%, 0.032%, 0.04%, 0.048%, 0.06%, respectively. Meanwhile, another syringe was added with 565 μL of APS solution (0.066 g

mL^{-1}) and 478 μL deionized water. The two syringes were connected with a Luer−Lock connector, so the two solutions were syringe−mixed to form a homogeneous solution. The mixture was immediately injected into rectangular acrylic molds of 80 × 20 × 3 mm^3 or 80 × 15 × 1.5 mm^3, covered with PMMA on both sides, and then kept at room temperature for 24 hours to complete the reaction. To prepare the regular PAAm gels, we follow the same procedure except for injecting the mixed solution into the acrylic molds covered by glass sheets on the two sides. The synthesis of double network TEA gels is similar to that for the single network TEA gels, and is detailed in *SI Appendix*.

Preparation of the bridging polymer solutions

This study tested two types bridging polymers: chitosan and gelatin. To prepare the chitosan solutions of 2%, 1%, and 0.5% w/v, 50 mL of deionized water was added with chitosan powders of 1, 0.5, 0.25 g, respectively. 400 μL of acetic acid was also added for a final pH of 4.5. The mixture was stirred overnight to form a homogeneous solution and then kept at 4°C before use. To prepare the gelatin solution of 2% w/v, 1g of gelatin powder was dissolved in 50 mL of deionized water. The solution was stirred in a water bath at 37°C for 30 mins before use.

All details associated with sample preparations, mechanical tests, derivation and calibration of the thermally activated chain slippage model, estimation of the diffusion coefficients of bridging polymers can be found in *SI Appendix*

4.5 Nomenclature

G_{slip}: adhesion energy based on slip linkage

G_{stitch}: adhesion energy based on stitch linkage

G_{hybrid}: adhesion energy based on hybrid linkage

μ: shear modulus

E: elastic modulus

σ_r: norminal stress

W: strain energy density

N: area density of linkage

k_B: Boltzman constant

T: Temperature

k_{slip}: spring constant of the slip linkage linkage prior to rupture

k_{stitch}: spring constant of the stitch linkage linkage prior to rupture

l_a: activation length of a bond

τ_-: intrinsic relaxation time of a linkage

F: force applied to separate a linkage

V: Speed at which the linkage is seperated

E_{slip}: activation energy of a slip linkage

E_{stitch}: activation energy of a stitch linkage

Bibliography

[1] Zhen Yang, Xingwei Yang, Rong Long, and Jianyu Li. Stimulation modulates adhesion and mechanics of hydrogel adhesives. *Langmuir*, 37(23):7097–7106, 2021.

[2] Hyesung Cho, Gaoxiang Wu, Jason Christopher Jolly, Nicole Fortoul, Zhenping He, Yuchong Gao, Anand Jagota, and Shu Yang. Intrinsically reversible superglues via shape adaptation inspired by snail epiphragm. *Proceedings of the National Academy of Sciences*, 116(28):13774–13779, 2019.

[3] Andrew B Croll, Nasibeh Hosseini, and Michael D Bartlett. Switchable adhesives for multifunctional interfaces. *Advanced Materials Technologies*, 4(8):1900193, 2019.

[4] Serena Blacklow, Jianyu Li, Benjamin R Freedman, Mahdi Zeidi, Chen Chen, and David J Mooney. Bioinspired mechanically active adhesive dressings to accelerate wound closure. *Science advances*, 5(7):eaaw3963, 2019.

[5] Hyunwoo Yuk, Teng Zhang, Shaoting Lin, German Alberto Parada, and Xuanhe Zhao. Tough bonding of hydrogels to diverse non-porous surfaces. *Nature Materials*, 15(2):190–196, 2016.

[6] Xiaoyu Chen, Hyunwoo Yuk, Jingjing Wu, Christoph S Nabzdyk, and Xuanhe Zhao. Instant tough bioadhesive with triggerable benign detachment. *Proceedings of the National Academy of Sciences*, 117(27):15497–15503, 2020.

[7] Jiawei Yang, Ruobing Bai, and Zhigang Suo. Topological adhesion of wet materials. *Advanced Materials*, 30(25):1800671, 2018.

[8] Yang Gao, Kangling Wu, and Zhigang Suo. Photodetachable adhesion. *Advanced Materials*, 31(6):1806948, 2019.

[9] Zhenwei Ma, Claire Bourquard, Qiman Gao, Shuaibing Jiang, Tristan De Iure-Grimmel, Ran Huo, Xuan Li, Zixin He, Zhen Yang, Galen Yang, et al. Controlled tough bioadhesion mediated by ultrasound. *Science*, 377(6607):751–755, 2022.

[10] Yecheng Wang, Kun Jia, Chunping Xiang, Jiawei Yang, Xi Yao, and Zhigang Suo. Instant, tough, noncovalent adhesion. *ACS Applied Materials & Interfaces*, 11(43):40749–40757, 2019.

[11] Edwin P Chan, Dongchan Ahn, and Alfred J Crosby. Adhesion of patterned reactive interfaces. *The Journal of Adhesion*, 83(5):473–489, 2007.

[12] James M Dugan, Carles Colominas, Andrés-Amador Garcia-Granada, and Frederik Claeyssens. Spatial control of neuronal adhesion on diamond-like carbon. *Frontiers in Materials*, 8:756055, 2021.

[13] Hyunwoo Yuk, Teng Zhang, German Alberto Parada, Xinyue Liu, and Xuanhe Zhao. Skin-inspired hydrogel–elastomer hybrids with robust interfaces and functional microstructures. *Nature communications*, 7(1):12028, 2016.

[14] Wonhyung Lee, Jongkyeong Lim, and Joonwon Kim. Conformal hydrogel-skin coating on a microfluidic channel through microstamping transfer of the masking layer. *Analytical Chemistry*, 95(21):8332–8339, 2023.

[15] Dylan C Young, Isabel G Newsome, and Jan Scrimgeour. Incorporation of soft shaped hydrogel sheets into microfluidic systems using a simple adhesion masking process. *Applied Physics Letters*, 111(26):263705, 2017.

[16] Sabyasachi Rakshit, Yunxiang Zhang, Kristine Manibog, Omer Shafraz, and Sanjeevi Sivasankar. Ideal, catch, and slip bonds in cadherin adhesion. *Proceedings of the National Academy of Sciences*, 109(46):18815–18820, 2012.

[17] Valeri Barsegov and Devarajan Thirumalai. Dynamics of unbinding of cell adhesion molecules: transition from catch to slip bonds. *Proceedings of the National Academy of Sciences*, 102(6):1835–1839, 2005.

[18] Rodger P McEver and Cheng Zhu. Rolling cell adhesion. *Annual review of cell and developmental biology*, 26:363–396, 2010.

[19] Patrick W Oakes, Shiladitya Banerjee, M Cristina Marchetti, and Margaret L Gardel. Geometry regulates traction stresses in adherent cells. *Biophysical journal*, 107(4):825–833, 2014.

[20] Mathew E Berginski, Eric A Vitriol, Klaus M Hahn, and Shawn M Gomez. High-resolution quantification of focal adhesion spatiotemporal dynamics in living cells. *PloS one*, 6(7):e22025, 2011.

[21] Jianyu Li, Adam D Celiz, Jiawei Yang, Quansan Yang, Isaac Wamala, William Whyte, Bo Ri Seo, Nikolay Vasilyev, Joost J Vlassak, and Mooney-David J Suo, Zhigang. Tough adhesives for diverse wet surfaces. *Science*, 357(6349):378–381, 2017.

[22] Jian Ping Gong, Akishige Kii, Jan Xu, Yoshihiko Hattori, and Yoshihito Osada. A possible mechanism for the substrate effect on hydrogel formation. *The Journal of Physical Chemistry B*, 105(20):4572–4576, 2001.

[23] Akishige Kii, Jian Xu, Jian Ping Gong, Yoshihito Osada, and Xianmin Zhang. Heterogeneous polymerization of hydrogels on hydrophobic substrate. *The Journal of Physical Chemistry B*, 105(20):4565–4571, 2001.

[24] Joydeb Mandal, Kaihuan Zhang, Nicholas D Spencer, et al. Oxygen inhibition of free-radical polymerization is the dominant mechanism behind the "mold effect" on hydrogels. *Soft Matter*, 17(26):6394–6403, 2021.

[25] Kaihuan Zhang, Rok Simic, Wenqing Yan, and Nicholas D Spencer. Creating an interface: rendering a double-network hydrogel lubricious via spontaneous delamination. *ACS Applied Materials & Interfaces*, 11(28):25427–25435, 2019.

[26] Manoj K Chaudhury. Rate-dependent fracture at adhesive interface. *The Journal of Physical Chemistry B*, 103(31):6562–6566, 1999.

[27] Evan Evans and Ken Ritchie. Dynamic strength of molecular adhesion bonds. *Biophysical Journal*, 72(4):1541–1555, 1997.

[28] George I Bell. Models for the specific adhesion of cells to cells: a theoretical framework for adhesion mediated by reversible bonds between cell surface molecules. *Science*, 200(4342):618–627, 1978.

[29] Ilya V Pobelov, Kasper Primdal Lauritzen, Koji Yoshida, Anders Jensen, Gábor Mészáros, Karsten W Jacobsen, Mikkel Strange, Thomas Wandlowski, and Gemma C Solomon. Dynamic breaking of a single gold bond. *Nature communications*, 8(1):15931, 2017.

[30] Costantino Creton and Matteo Ciccotti. Fracture and adhesion of soft materials: a review. *Reports on Progress in Physics*, 79(4):046601, 2016.

[31] Shu Wang, Sergey Panyukov, Michael Rubinstein, and Stephen L Craig. Quantitative adjustment to the molecular energy parameter in the lake–thomas theory of polymer fracture energy. *Macromolecules*, 52(7):2772–2777, 2019.

[32] Jason Steck, Junsoo Kim, Jiawei Yang, Sammy Hassan, and Zhigang Suo. Topological adhesion. i. rapid and strong topohesives. *Extreme Mechanics Letters*, 39:100803, 2020.

[33] Guangyu Bao, Qiman Gao, Massimo Cau, Nabil Ali-Mohamad, Mitchell Strong, Shuaibing Jiang, Zhen Yang, Amin Valiei, Zhenwei Ma, Marco Amabili, et al. Liquid-infused microstructured bioadhesives halt non-compressible hemorrhage. *Nature Communications*, 13(1):5035, 2022.

[34] Jiawei Yang, Ruobing Bai, Baohong Chen, and Zhigang Suo. Hydrogel adhesion: a supramolecular synergy of chemistry, topology, and mechanics. *Advanced Functional Materials*, 30, 1 2019.

[35] Jiawei Yang, Ruobing Bai, Jianyu Li, Canhui Yang, Xi Yao, Qihan Liu, Joost J Vlassak, David J Mooney, and Zhigang Suo. Design molecular topology for wet–dry adhesion. *ACS Applied Materials & Interfaces*, 11(27):24802–24811, 2019.

[36] Jeong-Yun Sun, Xuanhe Zhao, Widusha R. K. Illeperuma, Ovijit Chaudhuri, Kyu Hwan Oh, David J. Mooney, David J. Mooney, and Zhigang Suo. Highly stretchable and tough hydrogels. *Nature*, 489(7414):133–136, 2012.

[37] Guangyu Bao, Ran Huo, Zhenwei Ma, Mitchell Strong, Amin Valiei, Shuaibing Jiang, Shiyu Liu, Luc Mongeau, and Jianyu Li. Ionotronic tough adhesives with intrinsic multifunctionality. *ACS Applied Materials & Interfaces*, 13(31):37849–37861, 2021.

[38] Xinyue Liu, Ji Liu, Shaoting Lin, and Xuanhe Zhao. Hydrogel machines. *Materials Today*, 36:102–124, 2020.

[39] Jiawei Yang, Jason Steck, Ruobing Bai, and Zhigang Suo. Topological adhesion ii. stretchable adhesion. *Extreme Mechanics Letters*, 40:100891, 2020.

[40] Nikolche Gjorevski, Mikhail Nikolaev, Tobin E Brown, Olga Mitrofanova, Nathalie Brandenberg, Frank W DelRio, Francis M Yavitt, Prisca Liberali, Kristi S Anseth, and Matthias P Lutolf. Tissue geometry drives deterministic organoid patterning. *Science*, 375(6576):eaaw9021, 2022.

[41] Shaoting Lin, Hyunwoo Yuk, Teng Zhang, German Alberto Parada, Hyunwoo Koo, Cunjiang Yu, and Xuanhe Zhao. Stretchable hydrogel electronics and devices. *Advanced Materials*, 28(22):4497–4505, 2016.

[42] William Whyte, Ellen T Roche, Claudia E Varela, Keegan Mendez, Shahrin Islam, Hugh O'Neill, Fiona Weafer, Reyhaneh Neghabat Shirazi, James C Weaver, Nikolay V Vasilyev, et al. Sustained release of targeted cardiac therapy with a replenishable implanted epicardial reservoir. *Nature Biomedical Engineering*, 2(6):416–428, 2018.

[43] Daniel Vera, Maria Garcia-Diaz, Nuria Torras, Mar Alvarez, Rosa Villa, and Elena Martinez. Engineering tissue barrier models on hydrogel microfluidic platforms. *ACS Applied Materials & Interfaces*, 13(12):13920–13933, 2021.

[44] Alexandru Tudor, Colm Delaney, Hongrui Zhang, Alex J Thompson, Vincenzo F Curto, Guang-Zhong Yang, Michael J Higgins, Dermot Diamond, and Larisa Florea. Fabrication of soft, stimulus-responsive structures with sub-micron resolution via two-photon polymerization of poly (ionic liquid)s. *Materials Today*, 21(8):807–816, 2018.

[45] Marco Carlotti and Virgilio Mattoli. Functional materials for two-photon polymerization in microfabrication. *Small*, 15(40):1902687, 2019.

[46] James H Pikul, Shuo Li, Hedan Bai, Roger T Hanlon, Itai Cohen, and Robert F Shepherd. Stretchable surfaces with programmable 3d texture morphing for synthetic camouflaging skins. *Science*, 358(6360):210–214, 2017.

Supporting information

Note 1: TEA gel prepared by heterogeneous polymerization

We consider here the heterogeneous structure of the TEA gel imparted by the hydrophobic mold substrate. The phenomenon was first discovered by Gong et al.[1, 2, 3], who proposed that the hydrophobic mold substrate suppresses the polymerization of the precursor solution near the substrate-solution interface due to the increased interfacial tension. When the pre-gel solution starts polymerizing on the low-surface-tension mold such as PMMA, the interfacial tension between the hydrophobic mold surface and the liquid solution γ_{sl} increases with the increased polymer fraction. To minimize the free energy of the whole system, the mold surface repulses the polymers to create a depletion layer of thickness ξ_{dp}, where the polymer fraction is significantly reduced compared to that in the bulk. As the polymerization continues, the polymer chains in the bulk start to entangle and from a crosslinked network with the bulk network elasticity E_{bulk}. Within the depletion layer, however, the crosslinking process is influenced due to the extremely low polymer fraction, resulting in a layer of dangling chains of thickness h_{dc}. We shall consider ξ_{dp} and h_{dc} to be equivalent. In equilibrium, the increased interfacial energy $\Delta\gamma_{sl}$ equals the work done against E_{bulk} over the distance ξ_{dp}, leading to the relation $\Delta\gamma_{sl} \sim E_{bulk}\xi_{dp}$ or $\Delta\gamma_{sl} \sim E_{bulk}h_{dc}$. By assuming γ_{sl} changes negligibly with E_{bulk} when C is varied, and all the crosslinkers effectively contribute to load-bearing chains, it leads to the scaling relation: $h_{dc} \sim 1/E_{bulk} \sim 1/C$, which is plotted in Fig. 2c with the estimated h_{dc} values.

Recently, several results suggested that the inhibition of free-radical polymerization by trapped oxygen on hydrophobic substrates may play significant roles in the heterogeneous polymerization[4, 5]. Despite the debates on the underlying mechanisms, the substrate effect effectively produces heterogeneous structure of a TEA gel that comprises a layer of branched dangling chains spanning a thickness of h_{dc} near the surface, and a homogeneously crosslinked bulk network that is affected minimally by the substrate effect of thickness $h-2h_{dc}$ (considering the gel is polymerized between two hydrophobic molds).

Indication of dangling chain layer in TEA gels using cryosectioning and SEM imaging

We performed cryosectioning of TEA and regular SN PAAm gels with $C = 0.024\%$ into sheets of 100 μm thickness, and dehydrated the sheets in the open air (Fig 4.S3). The top and bottom edges of the TEA gel sheet are composed of branched dangling chains. Using SEM imaging, we observed that the two edges of the section shrink more than the center, forming a "ridge" with the downhill portion spanning over $\sim 400\mu$m to $\sim 600\mu$m(Fig 4.S3 b, d). We attribute the significant shrinkage near the edge to the low polymer content and crosslinking density in the dangling chain layer compared to the bulk, causing more volume change during the process of dehydration. In contrast, a cryosectioned regular gel sheet shows a smaller edge shrinkage with size $< 200\mu$m (Fig 4.S3 c, e), which is presumably due to the inhomogeneous de-swelling resulted from the bottom confinement by the glass slide [6]. The different amounts of edge shrinkage in TEA and regular gel sheets indicate that the edges of the TEA gel is composed of dangling chains. The dangling chain layer thickness h_{dc} is characterized using uniaxial tensile and micro-indentation tests, detailed below

Estimation of h_{dc} using uniaxial tensile test

We propose a simple model to characterize the value of h_{dc} of TEA gels. The model considers the TEA gel has an effective modulus of E_{tea}, composed of the bulk elastic modulus E_{bulk} and the dangling chain elastic modulus E_{dc}. It assumes that the bulk of the TEA gel the same elasticity E_{bulk} as that of a regular gel polymerized on glass E_{reg}, while the dangling chains has a modulus $E_{dc} \approx 0$, yielding:

$$\frac{2h_{\mathrm{dc}}}{h} = 1 - \frac{E_{\mathrm{tea}}}{E_{\mathrm{reg}}} \tag{4.1}$$

where E_{tea} and E_{reg} can be measured from uniaxial tensile tests. We fit the data with 5% of strain to the linear-elastic model, which is degenerated to from the neo-Hookean model at the small strain limit:

$$\sigma_{\mathrm{linear}} = E(\lambda - 1) \tag{4.2}$$

where σ is the nominal stress and λ is the stretch. We also fit the data to another hyperelastic material model, the incompressible neo-Hookean model:

$$W_{\mathrm{neo-Hookean}} = \frac{E}{6}(I_1 - 3) \tag{4.3}$$

where $I_1 = \lambda_1^2 + \lambda_2^2 + \lambda_3^2$. The Neo-Hookean model assumes that the polymer chains follow Gaussian distribution and are free of entanglements. Under uniaxial tensile test, the principle stretches: $\lambda_1 = \lambda$, $\lambda_2 = \lambda_3 = 1/\sqrt{\lambda}$. The nominal stress-stretch curves derived from the models are:

$$\sigma_{\text{neo-Hookean}} = \frac{E}{3}(\lambda - \lambda^{-2}) \tag{4.4}$$

We plot representative stress-stretch curves from uniaxial tensile tests in Fig. 4.S1 e and along with the fitted models. The Neo-Hookean model underestimates the slopes of the curves at $\lambda \to 1^+$ for all samples. The linear model that fit the data within λ from 1 to 1.05 is used to estimate the moduli of TEA and regular gels with varying values of C, plotted in Fig. 4.S1 e. With the values of E_{tea} and E_{reg}, we estimated the value of h_{dc} using the Eqn. 4.1. Note that our estimation of h_{dc} is much larger than those estimated by observing force-displacement curves from nano-indentation tests[4][7], which may attribute to the different values of C used in the studies. The projection of our data yields a similar estimation of h_{dc} at the same level of C as in Simic et al[4] ($C \approx 1\%$).

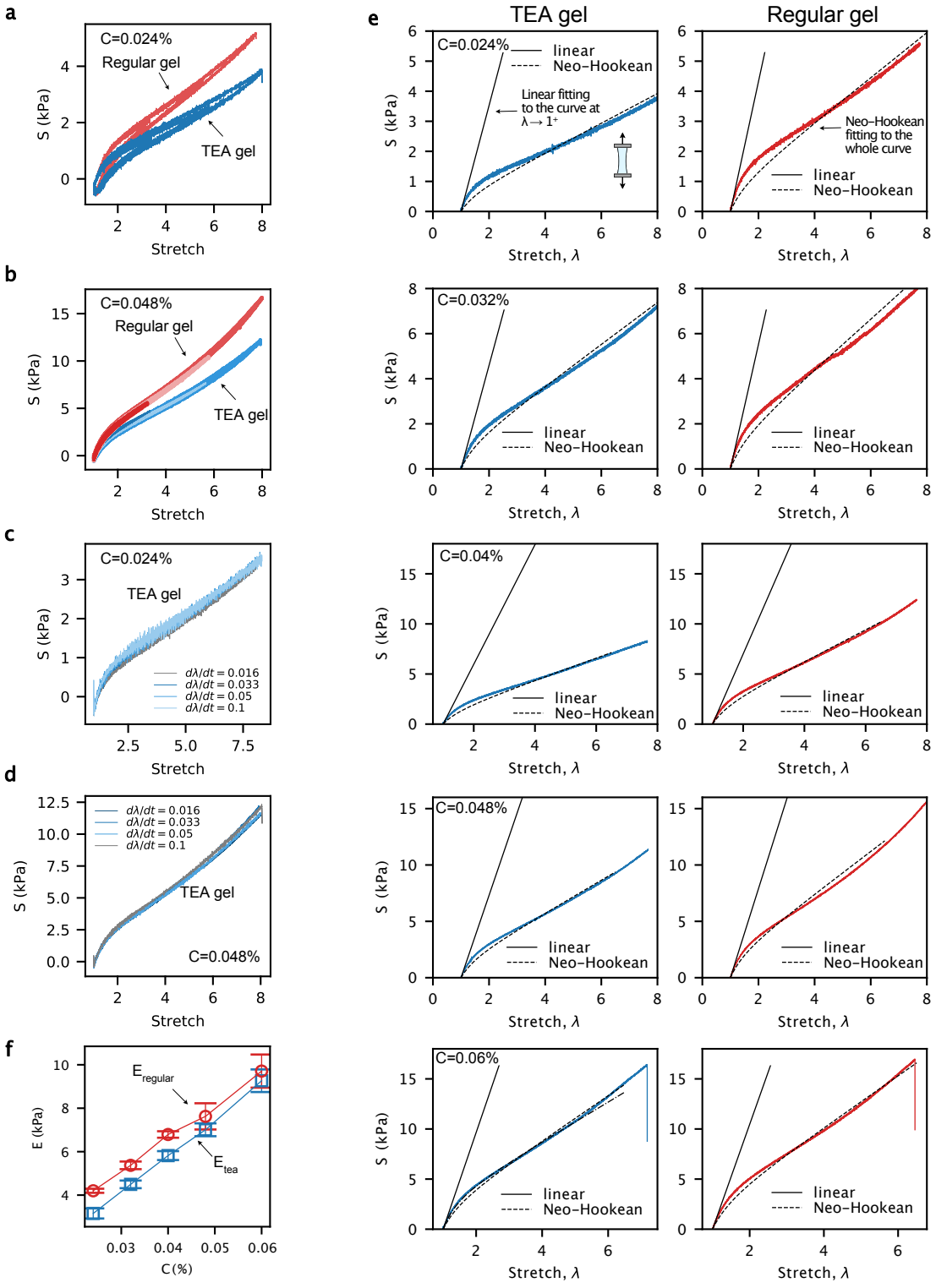

Fig. 4.S1: (a) Uniaxial cyclic tensile tests of a TEA and a regular gel made of SN PAAm for $C = 0.024\%$. (b) the same curves as (a) for $C = 0.048\%$. Uniaxial tensile test results of SN TEA gels with varying strain rates for (c) $C = 0.024\%$ and (d) $C = 0.048\%$. (e) representative stress-stretch curves of TEA (left) and regular (right) gels for different values of C measured in uniaxial tensile tests. (f) Measured elastic moduli by the linear model for SN TEA and regular gels, plotted as functions of C.

Estimation of h_{dc} using micro-indentation test

We further performed micro-indentation test to ascertain the value of h_{dc} using a custom built microindenter (Fig S2a and Methods). Fig 4.S2 b and c illustrate the indentation test on the regular and TEA gels.

It has been shown that the bulk network of TEA gels has similar moduli E_{bulk} as those of regular gels, but the modulus of the dangling chain layer E_{dc} is much smaller: $E_{\mathrm{dc}} \ll E_{\mathrm{bulk}}$ [8]. Thus the force-displacement curve of the TEA gel under indentation is expected to show a displacement delay δ_{delay} compared to that of the regular gel due to the soft dangling chain layer. Such displacement delay can be used as an indicator of the dangling chain thickness h_{dc}. For example, if $E_{\mathrm{dc}}/E_{\mathrm{bulk}} \to 0$, we expect $\delta_{\mathrm{delay}} \approx h_{\mathrm{dc}}$ (Fig 4.S2 c). Fig 4.S2 d shows that at large indentation depth, the force-displacement curves of all samples follow the scaling of $f \sim \delta^{3/2}$, indicating that the contacting behavior is Hertzian. At smaller indentation depths, the curves deviate from Hertzian contact presumably due to the adhesion between the gel surface and the indenter, resulting in JKR type of contact. Adhesion is also evidenced by our observation of a slight negative indentation force (i.e., tensile force) on the order of -200 μN as the indenter was approaching the substrate surface. This is the pull-in behavior where adhesion deforms the substrate to establish contact with the indenter. Given that the distance range of adhesive interaction (e.g., van der Waals forces) causing the pull-in event is much smaller than the range of indentation displacement ($\delta > 100\mu$m), we identify the pull-in event as the zero point for the indentation displacement. This condition is also adopted in other soft contact experiments [9]. The curve of the regular gel with $C = 0.048\%$ follows Hertzian contact even at small indentation depths, likely due to its higher modulus reducing the relative effect of adhesion [10].

Fig 4.S2 d also shows a displacement delay between TEA and regular gels as expected, with $\delta_{\mathrm{delay}} \approx 130\mu$m and 50μm for $C = 0.024\%$ and 0.048%, respectively. By shifting the indentation displacement δ of the TEA gels using their respective δ_{delay} values, the force-displacement curves of TEA and regular gels collapse onto each other, indicating that the bulk networks in TEA and regular gels have similar moduli E_{bulk} (Fig 4.S2 e). The ratio of $\delta_{\mathrm{delay}}/h_{\mathrm{dc}} \approx 0.4$ is consistent for both C values (Fig 4.S2 f) but is less than 1, suggesting that the dangling chain layer has a non-zero modulus when it is under compression. It has been shown that a layer of polymer brush can exhibit strong lateral compression stress due to the excluded volume effect [11], and behaves as nonlinear springs in compression [12] with a reported compressive modulus of 0.3kPa for varying grafting densities [13]. As such, we expect

that E_{dc} of the dangling chain layer to be non-zero when being compressed perpendicular to the dangling chain layer, but negligible when loaded in tension parallel to the dangling chain layer, as assumed in our uniaxial tensile test.

To provide an estimation of E_{dc}, we performed finite element (FE) modeling (Methods) to simulate the indentation of a layered material with the "bulk" and "dangling chain" regions of 2.63 mm and 0.37 mm, respectively, mimicking the structure of TEA gel at $C = 0.024\%$ (Fig 4.S2 g). We vary E_{dc}/E_{bulk} from 0 to 1 and extract δ_{delay} by comparing the force-displacement curves (Fig S2h). The ratio $\delta_{delay}/h_{dc} = 1$ when $E_{dc}/E_{bulk} = 0$, and decreases rapidly as E_{dc}/E_{bulk} increases, finally reaching 0 when $E_{dc}/E_{bulk} = 1$ (Fig S2i). Using an exponential fitting function $\delta_{delay}/h_{dc} = A \cdot \exp(-E_{dc}/E_{bulk})/B$ with A and B being fitting parameters, we find that $E_{dc}/E_{bulk} \approx 0.14$ when $\delta_{delay}/h_{dc} \approx 0.4$. Consequently, this suggests that $E_{dc} = 0.58$ kPa and 1.05 kPa for $C = 0.024\%$ and 0.048%, consistent with the compressive modulus of polymer brush swollen in viscous solvent tested in a quasi-static condition (0.3 kPa [13]).

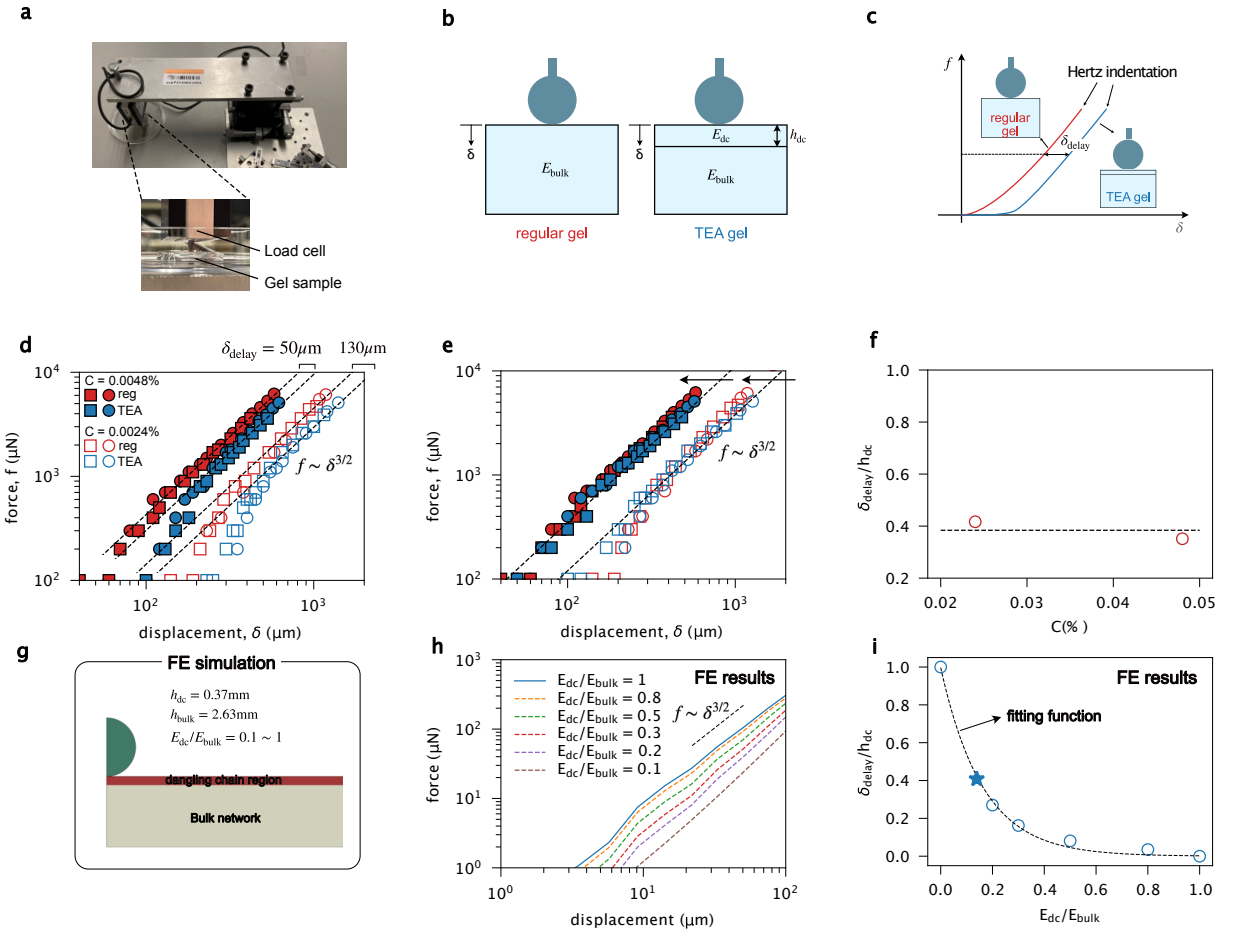

Fig. 4.S2: Micro indentation test of TEA and regular gels. (a) Experimental set up. (b) Schematics showing indentaion test on regular and TEA gels. (c) Schematics showing the proposed indentation behavior on the two types of gels. (d) Indentation results on regular and TEA gels, with two different C values. (e) Same as in (d) but with the curves of TEA gels shifted by their respective δ_{delay} values. (f) Ratio $\delta_{\text{delay}}/h_{\text{dc}}$ calculated using data in (d) and in Fig 2c, as a function of C. (g) Schematic illustrating the FE modeling of the indentation test. (h) force-displacement curves extracted from the FE simulation, for different $E_{\text{dc}}/E_{\text{bulk}}$ values. (i) $\delta_{\text{delay}}/h_{\text{dc}}$ plotted as a function of $E_{\text{dc}}/E_{\text{bulk}}$ extracted from the FE simulation.

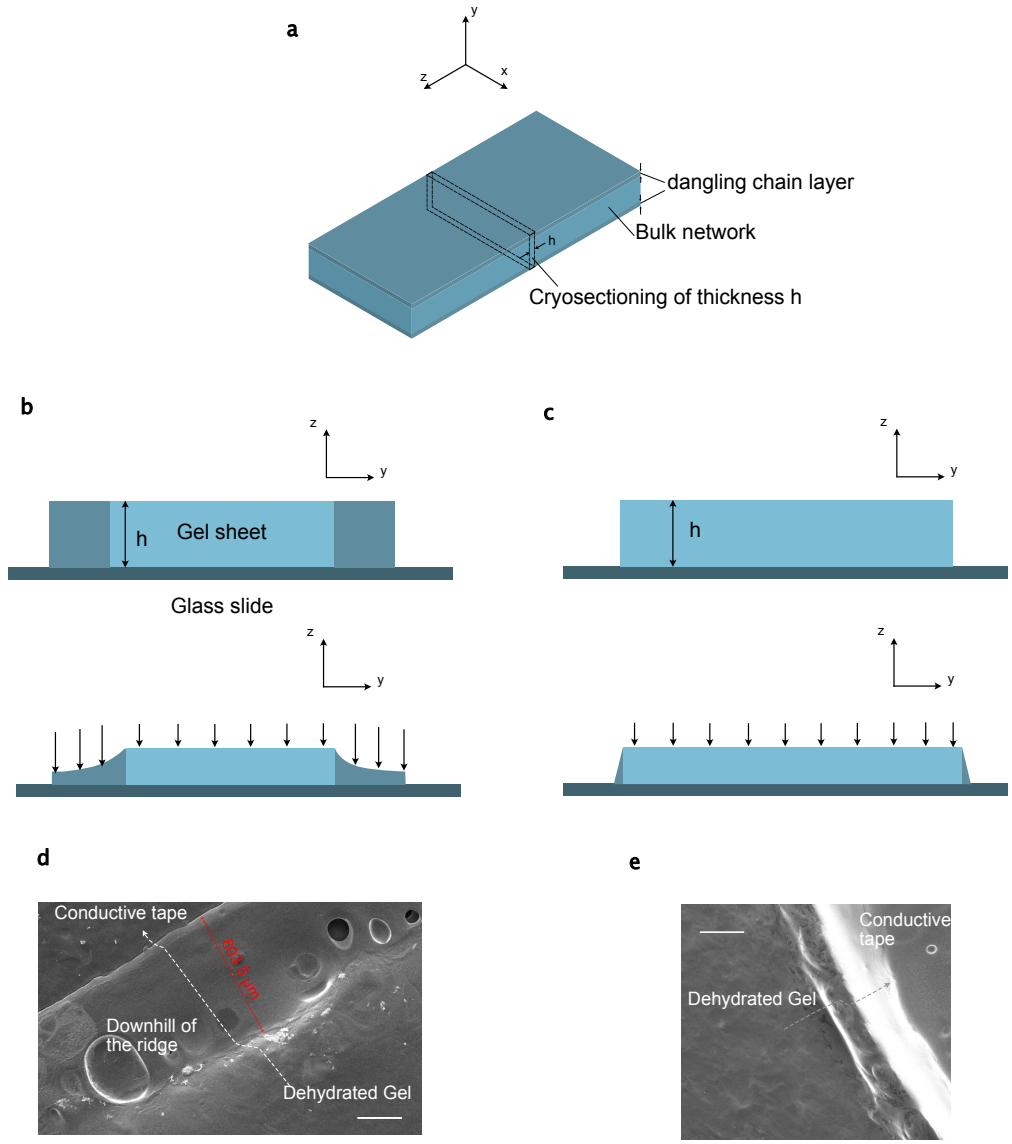

Fig. 4.S3: Cryosectioning of TEA and regular gels with $C = 0.024\%$. (a) Schematic showing the dimension of the samples. The samples were prepared by first immersing them in sucrose solution overnight, followed by immersing them in OCT solution overnight. The samples were then cryosectioned into sheets of thickness $h = 100\mu$m, transferred to glass slides, and dehydrated in open air. (b) Schematic showing the cross-sectional sheet of the cryosectioned TEA gel in the wet (top) and dehydrated (bottom) conditions. The sheet shrinks more significantly near the edge than in the center. (d) SEM image of a cryosectioned and dehydrated TEA gel sheet. They show "ridges" near the edge due to the inhomogeneous shrinkage. (c) Schematic showing the cross-sectional sheet of a cryosectioned and dehydrated regular gel in the wet (top) and dehydrated (bottom) conditions. (e) SEM image of a dehydrated regular gel sheet, showing less edge shrinkage effects. Scale bars in (d) and (e) are 200μm.

Estimation of bulk mesh size

Assuming the bulk network of the TEA gel and that of a regular gel have affine structures, so their shear modulus can be expressed as

$$\mu = \frac{E}{3} = \nu k_B T \tag{4.5}$$

where the density of the network strands $\nu = \frac{c_{\text{aam}}}{m_{\text{mono}} N_c} N_A$. The concentration of the aam solution is $c_{\text{aam}} = 6.76\text{g}/50 \times 10^{-6}\text{m}^3 = 1.352 \times 10^5$ g/m^3. The molar mass of aam is $m_{\text{mono}} \approx 71$ g/mole. Using the shear modulus of the regular PAAm gels for $C = 0.024\%$, the number of monomers between two crosslinkers are approximated as:

$$N_c = \frac{c_{\text{aam}}}{m_{\text{mono}}\mu} N_A = \frac{c_{\text{aam}}}{m_{\text{mono}}\mu / k_B T} N_A \approx 2348 \tag{4.6}$$

The mesh size is thus estimated as:

$$\xi = a N_c^{1/2} = 0.1 \times N_c^{1/2} \approx 5\text{nm} \tag{4.7}$$

where $a \approx 0.1$ nm is the length of a single bond.

Alternative approaches to create slip-linkage topology

Other approaches exist to create the similar chain-network topology of the slip linkage, such as by placing uncrosslinked polymer chains between hydrogel networks[14, 15]. The polymer chains can diffuse into the pre-formed gel networks to form slip entanglement. However, the highly permeable hydrogel would promote the diffusion of polymer chains into the gel matrix, greatly reducing the number of polymer entanglements on the interface.

Note 2: Thermally activated processes of chain slippage and ruptures

In experiments, we observed that $G^{1/2}$ for TEAs varies logarithmically with V_{crack} (Fig 2d and f) if $h_{pen}/h_{dc} \ll 1$, reminiscent of the dynamic adhesion of cell-cell interface[16], elastomer[17], and other bonds[18] due to thermally activated bond breaking. To rationalize the results, we adopt a kinetic theory which considers the linkage dissociation as thermally-activated processes[17, 19]. The activation for the dangling chain to slip from the bridging network is

assumed to decrease by the applied force (Fig 2e). Using the concept of mechanochemistry, the rate of dissociation of linkage i can be expressed as:

$$r_i(t) = -\frac{dN_i}{dt} = r_i N_i \tag{4.8}$$

where i can be stitch or slip. N_i is the areal density of linkage i, and r_i is the rate constant for linkage dissociation, and is assumed to be dependent on the force applied to the chains F via the Arrhenius law:

$$r_i = r_0 \exp\left(\frac{l_a F}{k_B T}\right) \tag{4.9}$$

where $r_0 = 1/\tau_-$ is the rate constant of the linkage dissociation without adding any force, τ_- is the intrinsic relaxation time of the slip linkage, $k_B T$ is the temperature in the unit of energy, F is the applied force to break a linkage. Note that we have assumed the linkage dissociation process is irreversible, thus the re-association of the linkage is not accounted for. We further consider an individual linkage has a spring constant k_i and is stretched at a fixed velocity V over an averaged bond survival time $\bar{t_i}$. Thus, the averaged force that an individual linkage can bear is given by:$\bar{F_i} = k_i V \bar{t_i}$.

For simplicity, the average linkage survival time $\bar{t_i}$ is estimated by the most probable survival time t_i^* corresponding to the maximum of the dissociation rate[20]: $d^2N/dt^2 = 0$. Therefore, $\bar{t_i}$ can be expressed as:

$$\bar{t_i} \approx t_i^* = \frac{k_B T}{k_i V l_a} \ln\left(\frac{l_a k_i V \tau_-}{k_B T}\right) \tag{4.10}$$

The energy released upon breaking linkage i can be expressed as:

$$e_i = \frac{\bar{F_i}^2}{2k_i} = \frac{V^2 \bar{t_i}^2 k_i}{2} \tag{4.11}$$

Substituting Eqn.4.10 into 4.11 and multiplying e_i with the number density of linkage N_i across an interface yields the energy released by advancing a unit area of an interface held by an array of slip linkages, namely, the adhesion energy:

$$G_i = \left(\frac{N}{2k_i}\right)\left(\frac{k_B T}{l_a}\right)^2 \left[\ln\left(\frac{l_a k_i V \tau_-}{k_B T}\right)\right]^2 \tag{4.12}$$

We further assume that the crack geometry remains invariant during the steady state peeling process, so $V_{\text{crack}} \sim V$. We express $\tau_- = h/(k_B T)\exp\left[E_i/(k_B T)\right]$, where E_i and h are the

activation energy of linkage i and Planck constant, respectively.

To calibrate N_i, we deduced that it is limited by the area density of the chitosan chains in the bridging network $N_i \approx N_{\text{chi}}$, since its size is presumably larger than that of hydrogel network and the spacing between dangling chains[14]. If true, Eqn. 4.12 suggests that in the absence of stitch linkage, $(G/N_{chi})^{1/2}$ should only depend on V_{crack}. Since we cannot obtain a direct measurement of N_{chi}, we adopt an approximation using the areal density of chitosan chains homogeneously dispersed in the solution using the chitosan polymer concentration c_{chi} (w/v%) through:

$$N_{chi} \sim \left(\frac{c_{chi}}{M_w} N_a\right)^{2/3} \tag{4.13}$$

Where $M_w \approx 300$kDa, estimated from our GPC test (Fig 4.S9) $N_a = 6 \times 10^{23}$ is the Avogadro number. Although Eqn. 4.13 provides a rough estimation of N_{chi}, they lead to a reasonable collapse of our data following the reformulation $(G/N_{chi})^{1/2}$ using different values of $c_{chi} =$ 2%, 1%, and 0.5% g/mL (Fig 4.S5b and c), confirming the validity to approximate N_i by N_{chi}.

Finally, the bridging network may form slip, stitch, or the combination of the two linkages when engaging with the TEA gel, yielding the expression for the total adhesion energy[17]:

$$G = \sum_i G_i \tag{4.14}$$

with

$$G_i = \left(\frac{N_i}{2k_i}\right)\left(\frac{k_B T}{l_a}\right)^2 \left[\ln\left(\frac{V_{\text{crack}} k_i l_a h}{(k_B T)^2}\right) + \frac{E_i}{k_B T}\right]^2$$

Given that an inextensible backing film was attached to the gel, V_{crack} is determined as the half of the peeling rate in the T-peel test. We then fit the model to the experimental data to estimate E_i and k_i.

Note 3: Estimation of D_{eff}

The molecular weight of a repeating unit of chitosan is approximately 160 g/mol. The averaged molecular weight of the chitosan polymer is taken to be 300 kDa (Fig. 4.S9). The number of repeating units is thus $N \approx 1800$. We approximate that the diffusion coefficient of bridging polymers in the dangling chain layer is similar to that of bridging polymers in water, due to the extremely low polymer content in the dangling chain layer [3]. According

to the Rouse model, the diffusion coefficient of the polymer in water is given by

$$D_{\text{eff}} = \frac{k_B T}{N \eta b} \tag{4.15}$$

taking $k_B T = 4.11 \times 10^{-21}$J, $N = 1800$, $\eta = 10^{-3}$ Pa×S, $b = 1$ nm the length of a repeating unit of chitosan, it gives $D_{\text{eff}} \approx 2 \times 10^{-12}$ m^{2}s^{-1}.

Note 4: Summary of topological linkages

Slip or stitch linkages

Bridging polymer chitosan or gelatin was directly applied to gel surfaces as polymer solution. Bridging polymer chains diffuse into, and simultaneously crosslink into a network in-situ with gels with or without dangling chain layer to form slip or stitch linkages, respectively.

Bond linkage

To form bond linkage between bridging chitosan network and tissue surfaces, we utilize the amine groups on chitosan, which can be covalently bonded to the carboxylic acid groups on tissue surfaces with EDC and NHS as coupling reagents[21]: 30 mg of EDC and 30 mg of NHS were added into 1 mL of the chitosan solution for forming covalent bonds with tissue surfaces. To form the bond linkage between bridging polymers and VHB elastomer surfaces, we utilize the Carbonyl bonds on the VHB, which can form imide bonds with the amine group on the chitosan polymer at pH = 4. Besides, the ionic bond formed between NH^{3+} of chitosan of pH < 6.5 and COO^- of the VHB of pH > 4.5 can also contribute to the bond linkage. We prepared chitosan of pH 4.5 and hydrogel of pH 7, thus the chitosan can form an interfacial bridging network and can form both type of bonds with VHB surfaces[22].

Materials

Synthesis of double network TEA

The TEA based on double-network gels was prepared with the following protocol. To prepare alginate/PAAm TEA, 1.5g alginate (I-1g) power and 6.76 g AAM were dissolved in 50 mL of deionized water. The first syringe was prepared following the aforementioned protocol, while the second syringe was added with 565 μL of APS solution and 478 μL calcium sulfate solution (15% w/v). The precursor solutions were quickly syringe-mixed and immediately

Linkage types	Adhesive network	Targeted substrate	Bridging polymer	Data
Slip-slip	TEA PAAm	TEA PAAm	Chitosan	Fig. 2d, f, Fig. S5b, c, Fig 4b,c
	∼	∼	Gelatin	Fig. 4b
Stitch-stitch	PAAm	PAAm	Chitosan	Fig. 2d,f
Slip-stitch	TEA PAAm	PAAm	Chitosan	Fig. 4c, Fig. S5d
Slip-bond	TEA PAAm	VHB elastomer	Chitosan	Fig. 4c
	TEA Alginate/PAAm	Porcine skin	Chitosan+EDC/NHS	Fig. 4c
	TEA Chitosan/PAAm	Porcine skin	Chitosan+EDC/NHS	Fig. 4c
Stitch-bond	PAAm	VHB elastomer	Chitosan	Fig. 4c
	Alginate/PAAm	Porcine skin	Chitosan+EDC/NHS	Fig. 4c
	Chitosan/PAAm	Porcine skin	Chitosan+EDC/NHS	Fig. 4c

Table 4.1: Types of topological linkages, their constituents (adhesive network, targeted substrate, and bridging polymer), and the associated data.

poured into 80 × 20 × 3 mm^3 rectangular acrylic molds covered with PMMA on the two sides, and then kept at room temperature for 24 hours to complete the reaction. To prepare the chitosan/PAAm TEA, acrylamide and chitosan powders were first dissolved in 0.2 M acetic acid at 3.3 mol/L and 2.5%, respectively. MBAA was then added to the AAm-chitosan solution at 0.0006:1 the weight of acrylamide to complete the polymer precursor solution. To prepare a gelling solution to crosslink the chitosan, 0.1 M Na_2HPO_4 and 0.1 M NaH_2PO_4 were first mixed with a volume ratio of 50:3. Sodium bicarbonate was then added to the solution at a concentration of 0.306 M. A mass fraction of 6.6% APS was later added to the solution as an initiator. Both solutions were degassed, quickly mixed at 3:2 volume ratio (polymer precursor to gelling solution) using syringes and injected into a mold with substrates of choice for overnight gelation. To prepare the regular alginate/PAAm and PAAm chitosan gels, we follow the same procedure except for injecting the mixed solution into the acrylic molds covered by glass sheets on the two sides followed by the gelation process.

Methods

Adhesion test

The TEA gels were prepared with a length of 80 mm (or 40 mm), width of 20 mm, and thickness of 3 mm, or otherwise specified. To test their adhesion on gels and VHB elastomers, the surface of TEA was treated with the bridging polymer solution of 0.25 $\mu L/mm^2$, and then immediately covered with the adherend. An instant compression of 15% strain was applied to remove the excessive solution on the interface. No prolonged compression was applied. For testing TEA adhesion on tissue samples, bridging polymer solution with chemical reagents added was applied to the tissue surface, followed by covering with the TEA gel. A continuous compression of 15% strain, or otherwise specified, over the whole course of

adhesion establishment was applied to the TEA-tissue sample. To measure the adhesion energy, standard T-peeling(180-degree peeling) was performed. The tests were conducted using a universal testing machine (Instron Model 5365) with 10N and 1kN load cells. Before test, PET backing is attached to the samples using Krazy glue. In a typical test, the peeling force reaches a plateau F_{plateau} once reaching the steady state process (Fig 4.S5a). The adhesion energy is calculated as twice the plateau force divided by the sample width, $G = 2F_{\text{plateau}}/w$. The loading rate was varied from 0.2 mm/s to 40 mm/s. Given the rigid backing, the crack speed for 180-degree peeling is half the loading rate.

Adhesion kinetics test

To characterize adhesion kinetics, nylon mesh of different thicknesses (50 and 120 μm) were used to define the thickness of the bridging polymer solution h_{sol} following a previously reported protocol[23]. We first immersed the nylon mesh in the bridging polymer solution, and then removed the excessive solution on the surface before applying it to the interface between two pieces of hydrogels. We waited for different time t before measuring adhesion energy using T-peeling test at a relative low crack speed $V_{\text{crack}} = 0.5$ mm/s. The adhesion energy increases with t and reaches the equilibrium value G_{eq}. The adhesion energy versus waiting time was fitted by the function $G = G_{eq}(1 - e^{t/t_{1/2}})$, where the half time $t_{1/2}$ can be extracted as the fitting parameter.

Uniaxial tensile test

Samples with length of 40mm, width of 20mm, thickness of 3mm were prepared and tested using the Instron machine with 1N and 1kN load cells. The nominal stress is calculated using $\sigma = F/A$ where F and A are the measured force and cross-sectional area of the sample. The stretch is calculated as $\lambda = \lambda_1/\lambda_0$ where λ_1 is the current length and λ_0 is the initial length.

Micro-indentation test

The set-up utilizes an XYZ linear stage (Optosigma, Santa Ana, CA) with a range of ± 6.5 mm for the X and Y directions and ± 5 mm for the Z direction. The resolution for all three directions is 10μm (Fig 4.S2a). An aluminum beam was mounted to the XYZ stage, with its other end connected to a load cell (Interface Inc., Scottsdale, AZ) with a capacity of 1 N and a resolution of 100 μN. We use a rigid spherical indenter (i.e., a steel ball) with a radius of $\approx$ 1.25mm.

Finite element (FE) modelling

We performed FE modelling to estimate the modulus of the dangling chain layer when it is under compression using a commercially available package ABAQUS 2019. In the model, the spherical indenter is modelled as a rigid body, and is subjected to a prescribed displacement loading condition. The "dangling chain region" and the "bulk network" are modelled using linear elastic model with elastic moduli E_{dc} and E_{bulk}, and with axisymmetric solid elements (CAX). Standard/static solver was used to simulate the indentation process.

Atomic force microscopy (AFM)

An atomic force microscope (JPK NanoWizard@3, Berlin, Germany) was used to conduct nano-indentation tests. Rectangular silicon cantilevers with 0.6 μm-in-diameter spherical beads attached as probes were used (Novascan, IA, USA). Cantilevers with a nominal spring constant of 0.6 N/m were used for experiment. The cantilever spring constants were determined using thermal noise method before the experiment. Hydrogel samples were immersed in PBS for 3 hours before indentation to avoid fast swelling during test. Then swollen hydrogels were glued to 35-mm Petri dishes and immersed in PBS during the measurement. Hertzian contact model was used to fit the indentation data and to calculate the Young's modulus.

Scanning electron microscope (SEM)

The structures of hydrogels were imaged using a field emission scanning electron microscope (FE450, FEI) under various magnifications. Before SEM imaging, all the samples were immersed in sucrose solution (20% w/v) over night, cryo-sectioned, and dehydrated in open air. The dehydrated samples were coated 4 nm Pt using a high-resolution sputter coater (ACE600, Leica) to increase surface conductivity. A conductive tape was used to mount the sample to the imaging platform.

GPC test

Chitosan samples with a concentration of 1 mg/mL were dissolved in an aqueous acetate buffer (0.25 M acetic acid, 0.25 M Na acetate) overnight, with stirring. They were filtrated (0.45 μ m) prior to be transferred to the autosampler vials. 100 μL injection was analyzed using a SEC column OHpak SB-805 HQ (8 mm ID x 300 mm L) at a flow rate of 0.3 mL /min of the eluting phase (same as the one in which samples were dissolved). The signal of the

RI detector was used for calculation of the molecular weights and PDI against a calibration curved constructed with pullulan standards of narrow polydispersity and molecular weight in the 5.9 to 788 kDa range.

Confocal microscopy

Hydrogel samples with diffused bridging polymers were imaged with a confocal microscope (LSM 710, Zeiss). Hydrogel samples with diffused FITC-chitosan were cut into thin slices by a blade and transferred to a 35 mm Petri dish with coverslip bottom (MatTek, P35G-0-10-C). The polymer network was imaged with 10X and 20X objective lenses. Axiovert A1 inverted microscope (Zeiss) equipped with a motorized stage was used to obtain fluorescent signals at multiple locations. Light intensity was maintained the same for all the samples.

Patterned TEA

A PTFE tape of thickness 0.1mm was designed into different shapes and then adhered to a glass plate (Fig 4.S7e left). Alternatively, four glass slides of thickness 1mm and a PTFE sheet of thickness 0.9 mm was assembled in the plane (*SI Appendix* Fig 4.S7e right). A rectangular acrylic mold was placed on top of patterned substrate. After injecting pre-gel solution, the mold was covered with another glass plate. The two approaches result in different flatnesses of the gel surface but both yielding high-fidelity adhesion selectivity.

TEA-based wound patch

A PTFE tape of thickness 0.1mm was designed into a circle of diameter 1.5 cm, and then adhered to a glass plate. A rectangular acrylic mold was placed on top of patterned substrate. After injecting pre-gel solution, the mold was covered with another glass plate. Biopsy punch was used to generate circular wounds on rat skin (diameter of 6mm) and porcine stomach (diameter of 1cm). When de-molded, the TEA gel was applied to wounds on rat skin and porcine stomach with 2% chitosan and EDC/NHS reagents. A prolonged compression for 3 mins was then applied by hand. The size of the circular danlging chain region of the TEA adhesive can be tailored to suit different sizes of the wounds.

TEA-based fluidic channels

A PTFE tape of rectangular (or 'S'-shape) was attached to a glass plate. Pre-gel solution is injected into the mold for reaction to complete. Once de-molded, we use hole punch of

diameter 2 mm to create an inlet hole and an outlet hole, and then attach it to a targeted surface using chitosan as bridging polymer. If the targeted surface is tissue, we also added chemical reagents to form covalent bonds between chitosan and tissue surfaces. After the adhesion is established, we further insert two soft tubes into the inlet and outlet, sealed using Crazy glue, and slowly inject liquid to cleave the weak adhesion by slip linkages. The fluidic channel is formed once the whole weak interface is separated.

TEA-based Drug eluting devices

A SN PAAm TEA gel was first prepared on a glass mold substrate patterned with a circular PTFE film of diameter 2 cm. It was then adhered to a regular gel which was glued onto an acrylic sheet. The circular low-adhesion region served as local depot to which drugs will be injected. The albumin-FITC (A9771, Sigma-Aldrich) was used as a model drug and was dissolved in PBS at 10 mg/mL to get the drug solution. At equilibrium of hydrogels, different volume of drug solution (0.2 mL and 0.5 mL) was slowly injected into the weak interface, resulting in local drug punches inside the hydrogel. After the injection, the whole device was immersed in 200 mL PBS. At determined time points, the fluorescence intensity of the solutions was measured using a BioTek Synergy HTX multi-mode microplate reader (λex = 485/20 nm, λem = 528/20 nm). A standard calibration curve was made in order to calculate the concentration of released drug.

TEA-based reconfigurable soft actuators

Individual actuator module was prepared using a molding process. SN PAAm pregel solution was injected to a 3D printed mold made of PLA (Fig 4.S8). The mold was then covered by a PMMA sheet. Once the reaction is completed and demolded, the actuator module readily carries dangling chains on its surface. Different modules were connected by applying bridging polymer chitosan to the interface. To separate the connected modules, a small force with a low separate rate can be applied. The separated modules can be reconnected following reapplying bridging polymers to the interface.

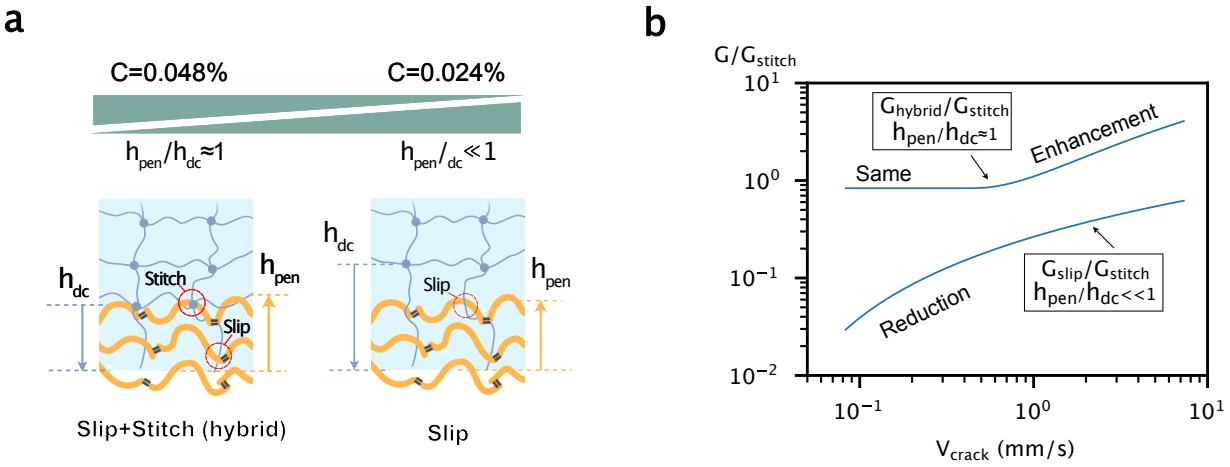

Fig. 4.S4: (a) Illustrations showing the effects of entanglement length on the formation of slip and stitch linkages. (b) Adhesion contrast between the slip and stitch regions in a patterned TEA for given C and $h_{\mathrm{pen}}/h_{\mathrm{dc}}$ values. The slip linkage becomes the hybrid linkage as $h_{\mathrm{pen}}/h_{\mathrm{dc}}$ becomes closer to 1.

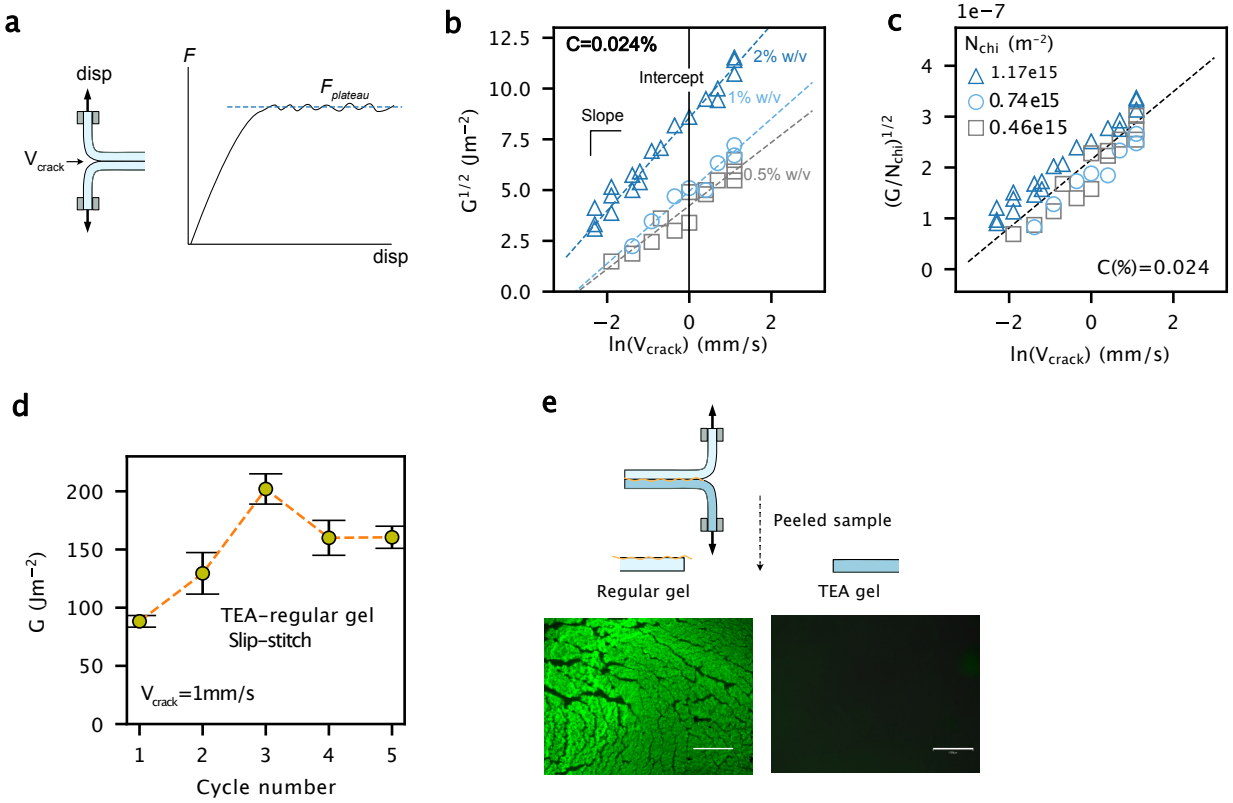

Fig. 4.S5: Schematic showing the T-peeling test and the resulting force-displacement curves. The adhesion energy is interpret as $G = 2F_{plateau}/w$, with w the out-of-plane thickness of the sample. (b) $G^{1/2}$ by the slip-slip linkage plotted as a function of $\ln V_{\text{crack}}$ for $C = 0.024\%$ and varying c_{chi} ($0.5\%, 1\%$, and 2% g/mL) (c) reformulated $(G/N_{chi})^{1/2}$) for $C = 0.024\%$, where N_{chi} is estimated using Eqn 4.13. (d) Cyclic peeling test on a TEA-regular interface at V_{crack}=1mm/s. After every peeling, a new regular gel adheres to the same TEA gel with newly applied chitosan solution. The adhesion increases and stabilizes after 5 cycles. (e) Peeled regular gel and TEA gel after a peeling test. The interface was bonded with a slip-stitch linkage using fluorescently labeled chitosan. After peeling, the chitosan network remains on the regular gel, but remains minimally in the TEA gel. Scale bars: 1mm.

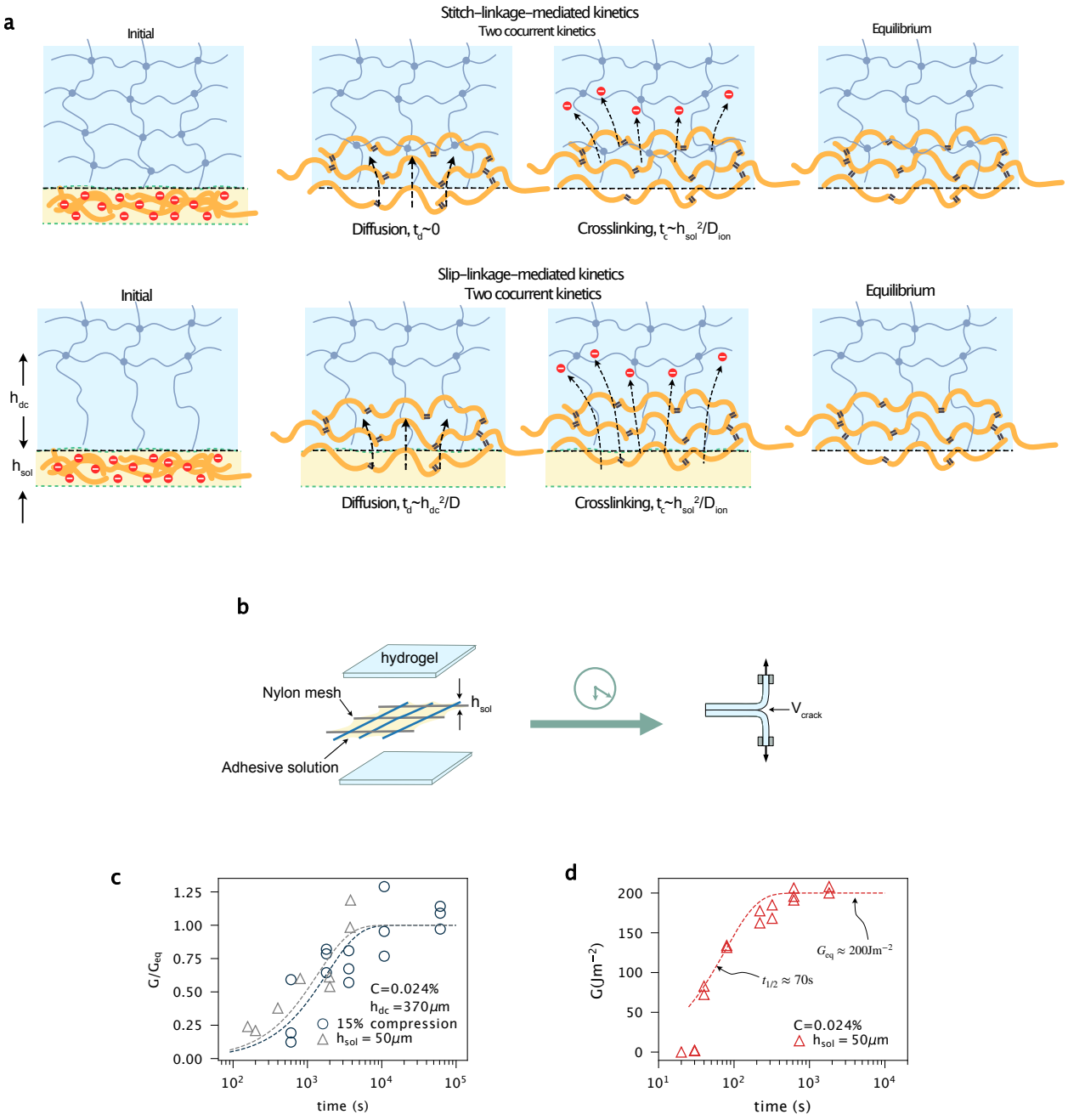

Fig. 4.S6: (a) Illustrations showing the total kinetics of stitch-mediated (top) and slip-mediated interface (bottom) as two sub kinetic physical processes. (b) Illustration showing the experimental procedure to characterize the adhesion kinetics of TA and TEA. (c) Dimensionless adhesion G/G_{eq} as functions of waiting time for TEA with $h_{\mathrm{dc}} = 370\mu m$. In one case $h_{\mathrm{sol}} = 50\mu m$ was controlled by using nylon mesh of the same thickness at the interface. In the other case, an initial compression strain of 15% was applied to the sample after applying adhesive solution without using the thickness-defining mesh, such that h_{sol} was not well-controlled. No prolonged compression was applied. (d) Adhesion energy G between two regular hydrogels with $C = 0.024\%$ as a function of waiting time for cast solution thicknesses $h_{\mathrm{sol}} = 50\mu m$. $G_{\mathrm{eq}} \approx 200\mathrm{Jm}^{-2}$ and $t_{1/2} \approx 70\mathrm{s}$.

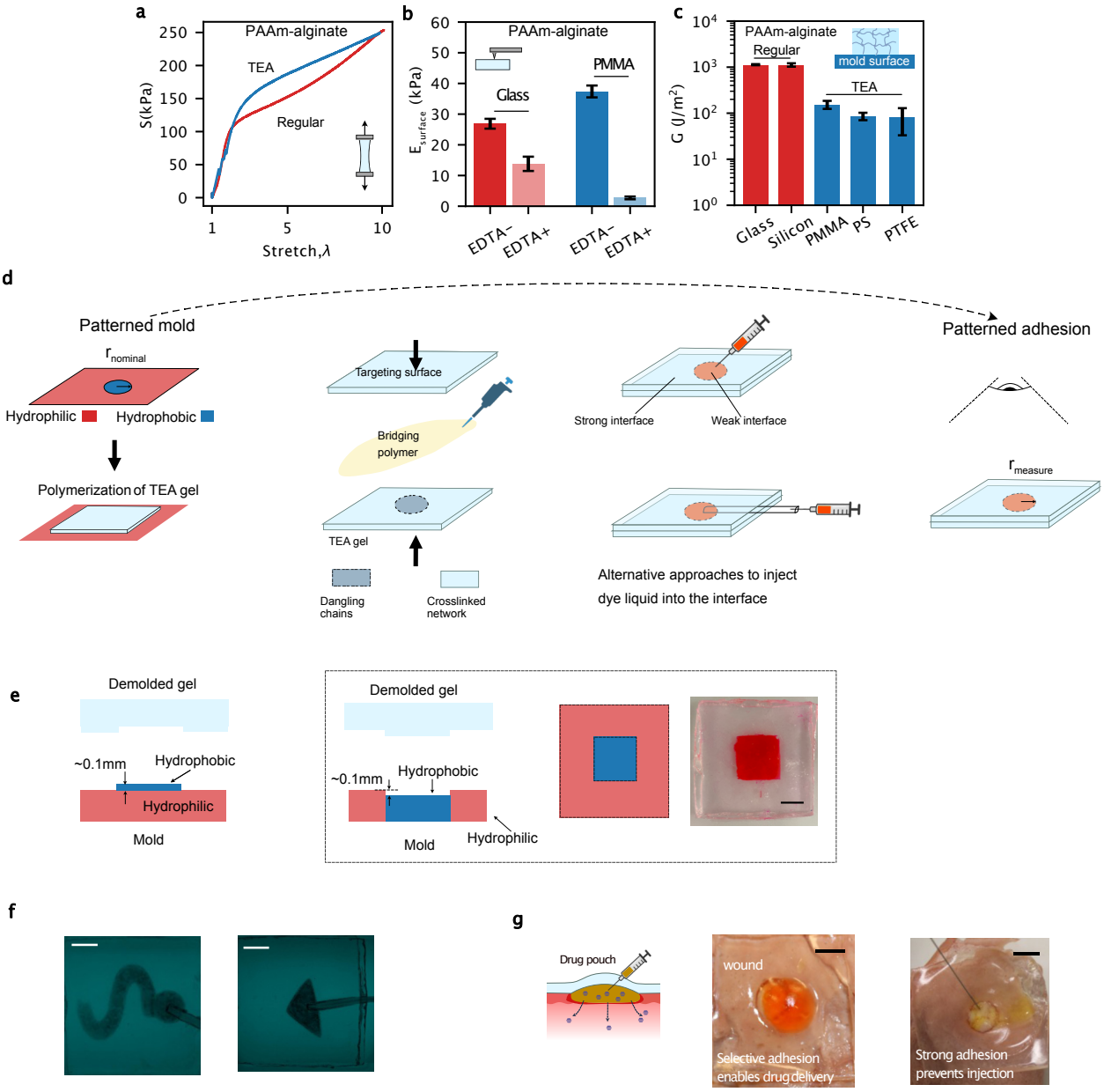
a
PAAm-alginate
TEA
Regular
S(kPa)
Stretch,λ
b
PAAm-alginate
Glass
PMMA
E surface (kPa)
EDTA−
EDTA+
c
PAAm-alginate
Regular
mold surface
TEA
G (J/m²)
Glass
Silicon
PMMA
PS
PTFE
d
Patterned mold
r nominal
Hydrophilic
Hydrophobic
Polymerization of TEA gel
Targeting surface
Bridging polymer
TEA gel
Dangling chains
Crosslinked network
Strong interface
Weak interface
Alternative approaches to inject dye liquid into the interface
Patterned adhesion
r measure
e
Demolded gel
~0.1mm
Hydrophobic
Hydrophilic
Mold
f
g
Drug pouch
wound
Selective adhesion enables drug delivery
Strong adhesion prevents injection

Fig. 4.S7: (a) Uniaxial tensile test results show similar engineering stress-stretch curves for a DN TEA and a DN regular alginate/PAAm gels. (b) AFM test on the surface of the DN gels polymerized on PMMa and glass molds with and without EDTA treatment, which can disassociate the ionic crosslinker in the alginate network. For DN gels made on PMMa mold, the difference in the surface moduli with and without EDTA treatment is more pronounced than those made on glass mold, suggesting the presence of surface dangling chains in the DN gels made on PMMa molds. (c) Adhesion of alginate/PAAm gels made on different mold surfaces on porcine skin. In this study, the continuous compression strain applied to these samples during the course of adhesion establishment is $\sim 30\%$, and the dimension of the samples is 80mm(length)×15mm(width)×1.5mm(thickness). The applied crack speed is 0.25mm/s. (d) Schematic illustrating the procedure for creating spatially programmable adhesion of TEA: a needle is used to penetrate the hydrogel into the interface, or a tube was sandwiched between the two gels. Next, liquid dye was injected through the needle or the tube. Finally, a digital camera was used to capture the weak interface through the liquid dye. (e) Illustration of the two strategies to pattern the surface of the gels. Left and right strategies result in a dent and a bump on the demolded gel surface where dangling chain forms, respectively. The strategy shown in left produces high fidelity selective adhesion in Fig S5(f) and Fig 5, while the strategy shown in right also results in high fidelity selective adhesion, shown in the box. Scale bar: 1cm. The results prove that the flatness of the gels does not affect the designed adhesion selectivity. (f) Patterned interface formed between a TEA alginate/PAAm gel and a regular alginate/PAAm gel. The TEA gel is designed with designed dangling chain regions of different shapes, resulting in weak interfaces of the identical shape. Scale bar: 10 mm. (g) Mock drug is injected to the weak interface of a TEA patch (DN alginate/PAAm) adhered to the wound of a porcine stomach. If a regular patch without programmed selective adhesion was adhered to the wounded porcine stomach, strong adhesion to the wound prevents injection of drug. Scale bars: 12mm

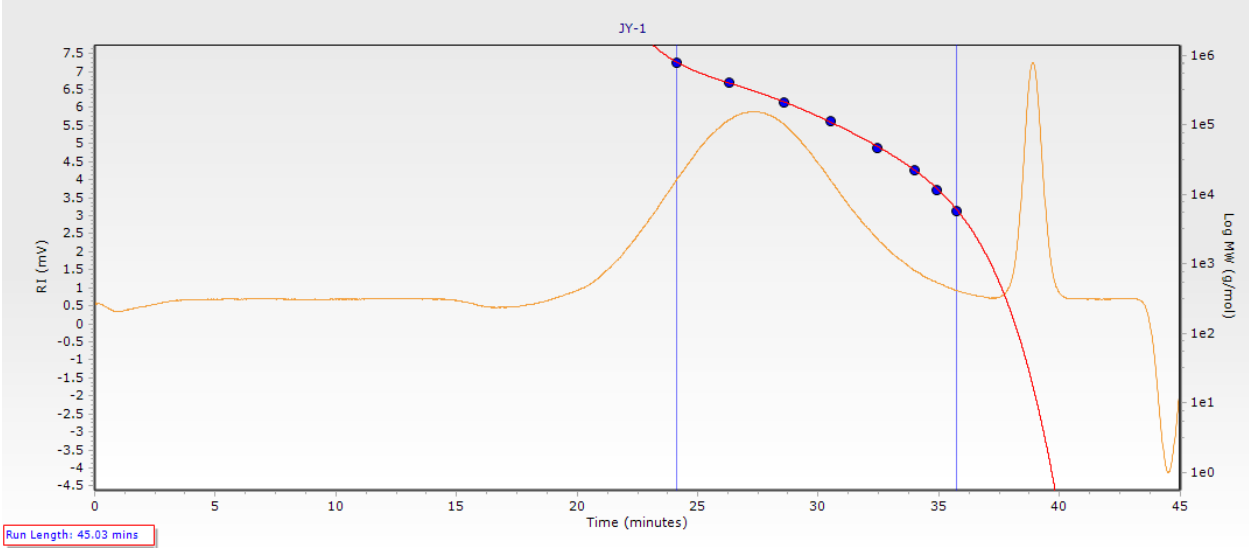

Fig. 4.S9: GPC test results. An approximated value of molecular weight may be calculate using the equation of the calibration curve: $y = -3.306E-05x^5 + 0.004911x^4 - 0.2913x^3 + 8.624x^2 - 127.4x + 757.8$ Where x is equal to the elution time (27.42 min). (MW is between 212 and 404 kDa. An approximated value $MW \approx 300$ kDa is used in calibration the area density of slip and stitch linkage in *SI Appendix* Note 2.)

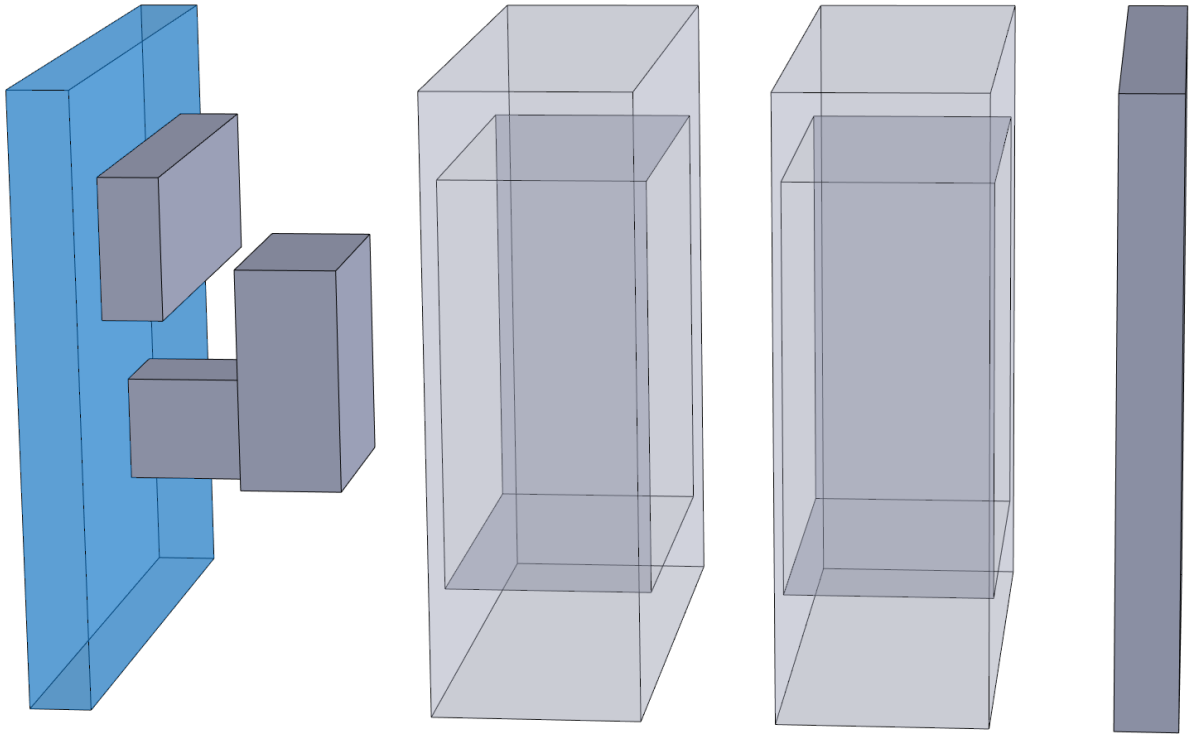

Fig. 4.S8: 3D printed mold for creating soft actuator modules. The mold parts are 3D-printed using PLA. The cover, indicated in blue, is made of PMMA.

Bibliography

[1] Jian Ping Gong, Akishige Kii, Jan Xu, Yoshihiko Hattori, and Yoshihito Osada. A possible mechanism for the substrate effect on hydrogel formation. *The Journal of Physical Chemistry B*, 105(20):4572–4576, 2001.

[2] Akishige Kii, Jian Xu, Jian Ping Gong, Yoshihito Osada, and Xianmin Zhang. Heterogeneous polymerization of hydrogels on hydrophobic substrate. *The Journal of Physical Chemistry B*, 105(20):4565–4571, 2001.

[3] Jian Ping Gong, Takayuki Kurokawa, Tetsuharu Narita, Go Kagata, Yoshihito Osada, Goro Nishimura, and Masataka Kinjo. Synthesis of hydrogels with extremely low surface friction. *Journal of the American Chemical Society*, 123(23):5582–5583, 2001.

[4] Joydeb Mandal, Kaihuan Zhang, Nicholas D Spencer, et al. Oxygen inhibition of free-radical polymerization is the dominant mechanism behind the "mold effect" on hydrogels. *Soft Matter*, 17(26):6394–6403, 2021.

[5] Kaihuan Zhang, Rok Simic, Wenqing Yan, and Nicholas D Spencer. Creating an interface: rendering a double-network hydrogel lubricious via spontaneous delamination. *ACS Applied Materials & Interfaces*, 11(28):25427–25435, 2019.

[6] Wei Hong, Zishun Liu, and Zhigang Suo. Inhomogeneous swelling of a gel in equilibrium with a solvent and mechanical load. *International Journal of Solids and Structures*, 46(17):3282–3289, 2009.

[7] Allison L Chau, megan K Cavanaugh, Yen-Tsung Chen, and Angela A Pitenis. A simple contact mechanics model for highly strained aqueous surface gels. *Experimental Mechanics*, 61:699–703, 2021.

[8] Tetsuharu Narita, Alexandra Knaebel, Jean-Pierre Munch, Sanveur Jean Candau, Jian Ping Gong, and Yoshihito Osada. Microrheological investigation of substrate-induced gradient structure in hydrogels. *Macromolecules*, 34(16):5725–5726, 2001.

[9] Yalin Yu, Daniel Sanchez, and Nanshu Lu. Work of adhesion/separation between soft elastomers of different mixing ratios. *Journal of Materials Research*, 30(18):2702–2712, 2015.

[10] Robert W Style, Anand Jagota, Chung-Yuen Hui, and Eric R Dufresne. Elastocapillarity: Surface tension and the mechanics of soft solids. *Annual Review of Condensed Matter Physics*, 8:99–118, 2017.

[11] M Manav, Mauricio Ponga, and A Srikantha Phani. Stress in a polymer brush. *Journal of the Mechanics and Physics of Solids*, 127:125–150, 2019.

[12] Ivan Argatov, Feodor M Borodich, and Xiaoqing Jin. Atomic force microscopy of polymer brushes: insights into controversies. *Frontiers in Mechanical Engineering*, 8:931271, 2022.

[13] Christian H Mathis, Chengjun Kang, Shivaprakash N Ramakrishna, Lucio Isa, Nicholas D Spencer, et al. Indenting polymer brushes of varying grafting density in a viscous fluid: A gradient approach to understanding fluid confinement. *Polymer*, 169:115–123, 2019.

[14] Jiawei Yang, Ruobing Bai, and Zhigang Suo. Topological adhesion of wet materials. *Advanced Materials*, 30(25):1800671, 2018.

[15] Hugh R Brown. Effects of chain pull-out on adhesion of elastomers. *Macromolecules*, 26(7):1666–1670, 1993.

[16] George I Bell. Models for the specific adhesion of cells to cells: a theoretical framework for adhesion mediated by reversible bonds between cell surface molecules. *Science*, 200(4342):618–627, 1978.

[17] Manoj K Chaudhury. Rate-dependent fracture at adhesive interface. *The Journal of Physical Chemistry B*, 103(31):6562–6566, 1999.

[18] Ilya V Pobelov, Kasper Primdal Lauritzen, Koji Yoshida, Anders Jensen, Gábor Mészáros, Karsten W Jacobsen, Mikkel Strange, Thomas Wandlowski, and Gemma C Solomon. Dynamic breaking of a single gold bond. *Nature communications*, 8(1):15931, 2017.

[19] Chung-Yuen Hui, Tian Tang, Yu-Yun Lin, and Manoj K Chaudhury. Failure of elastomeric polymers due to rate dependent bond rupture. *Langmuir*, 20(14):6052–6064, 2004.

[20] Evan Evans and Ken Ritchie. Dynamic strength of molecular adhesion bonds. *Biophysical Journal*, 72(4):1541–1555, 1997.

[21] Jianyu Li, Adam D Celiz, Jiawei Yang, Quansan Yang, Isaac Wamala, William Whyte, Bo Ri Seo, Nikolay Vasilyev, Joost J Vlassak, and Mooney David J Suo, Zhigang. Tough adhesives for diverse wet surfaces. *Science*, 357(6349):378–381, 2017.

[22] Jiawei Yang, Ruobing Bai, Jianyu Li, Canhui Yang, Xi Yao, Qihan Liu, Joost J Vlassak, David J Mooney, and Zhigang Suo. Design molecular topology for wet–dry adhesion. *ACS Applied Materials & Interfaces*, 11(27):24802–24811, 2019.

[23] Jason Steck, Junsoo Kim, Jiawei Yang, Sammy Hassan, and Zhigang Suo. Topological adhesion. i. rapid and strong topohesives. *Extreme Mechanics Letters*, 39:100803, 2020.

Chapter 5

Discussion and future work

5.1 Applicability of the strategies

In the first part of the thesis, we focus on a specific stimulus, temperature, to trigger the bulk contraction of a PNIPAm-based hydrogel adhesives. We discovered that in the presence of a sufficiently high initial adhesion energy, the post-stimulation adhesion energy is enhanced by almost two fold with no interface delamination. The results are rationalized by the enhanced bulk fracture energy and the insignificant intrinsic energy release rate induced by the contraction.

The data reported in chapter 3 was constrained to the regime where the initial adhesion energy G_c is higher than the energy release rate induced by contraction G, primarily due to the peeling testing specimen which often yield less accurate measurements in cases of sufficiently low adhesion energy. To examine the cases when $G_c < G$, extra effort has been made to measure the initial and post-stimulation adhesion energy using a modified lap-shear specimen as detailed in section 2.4.2. The modified lap-shear test offers a distinct advantage in accurately measuring low adhesion energy. Moreover, this test enables rapid loading of the sample onto the tensile machine after it is being heated under 37°C, facilitating adhesion energy measurement while the sample remains at a relatively elevated temperature (close to 37°C). The details of the modified lap-shear test can be found in Appendix.

We prepared topohesive solution (see list of Acronym and chapter 3 for the definition of topohesive) with varying the chitosan concentration without the addition of any chemical reagents. This ensured that only physical interactions were operative at the interface, resulting in relatively modest adhesion energies. Intriguingly, we observed a significant reduction in the post-stimulation (PS) adhesion energies when the initial adhesion energy $G_c < 10$ Jm^{-2}, yielding average switch ratios (SR, see Eqn 1.2 for definition) within the range of $10 \sim 100$ due to the adhesion switch-off (Fig 5.1). These observations strongly suggest that the interface debonds at the recorded initial G_c values leading to adhesion switch, most likely attributed to the intrinsic energy release rate induced by contraction surpassing the threshold of G_c. Consequently, by employing a single stimulus source, namely temperature variation, in conjunction with varying prescribed initial adhesion energy G_c, the stimuli-responsiveness can serve as either adhesion switch or toughener, and the bonding condition of the stimuli-responsive hydrogel adhesive can be manipulated extensively. This variability spans a wide range, yielding SR that fluctuate between 1 and 100 accounting for both adhesion switch-on and -off (Fig 5.1).

The experimental data can be well captured by our analytical and numerical methods introduced in chapter 3. We note that the analytical modeling is based on the assumptions of small deformation and linear elasticity, thus only serving as a first order approximation.

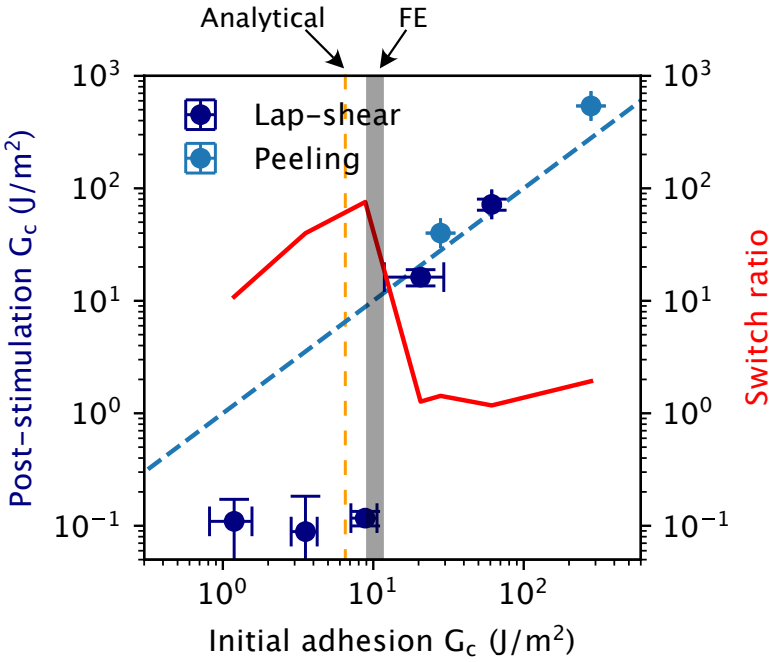

Fig. 5.1: Post-stimulation adhesion energy versus initial adhesion energy, measured from modified lap-shear test and peeling test from chapter 3. The initial adhesion energy is tuned using topohesives with varying chitosan concentrations and coupling reagents. Together plotted is the switch ratio, defined as the post-stimulation adhesion energy to the initial adhesion energy. The estimations of G in chapter 3 by analytical and FE models are indicated by the vertical dashed and solid lines, respectively. The G estimations are consistent with the experimental data where the switch ratio experiences a drastic decrease, indicating the transition from $G < G_c$ to $G > G_c$.

To consider the nonlinear elasticity of the stmuli-responsive hydrogel adhesive, we further developed the FE model to estimate G due to contraction. Nevertheless, the two estimations of G are close.

One limitation of using stimuli-responsive hydrogel adhesives, is that, the high values of SR is achieved only when $G_c < G$ (Fig 5.2). In this context of adhesion switch, the contraction-induced intrinsic energy release rate G becomes paramount. However, as Eqn 2.23 illustrates, G is constrained by factors such as the moduli, sizes, and volume shrinkage of the stimuli-responsive hydrogel adhesives. Considering that the majority of hydrogel adhesives exhibit elastic moduli within the range of $\sim$ 1 Pa to $\sim$ 100 kPa, thicknesses around 1 mm, and volume shrinkage of approximately 50%, G_{in} is confined to values between $\sim$0.0001 and $\sim$10 Jm^{-2}. Thus, the use of stimuli-responsiveness as adhesion switch becomes insignificant in scenarios where G_c far exceeds 10 Jm^{-2}.

To overcome the limitation for tuning hydrogel adhesion energy in a greater range, Chapter 4 presents a method that directly manipulates the adhesion energy through the engineered

design of the polymer network topology. The term "topology" originates from a branch of mathematics, which studies the intrinsic properties of geometrical properties that remains unchanged when the object is under various deformation [1]. In polymer science, the term "topology" is often used to represent varying polymer structures [2], including dangling chains, loops, trapped polymer entanglements, etc., and these different network topologies emerge due to the varying synthesis conditions [3]. It has been studied that the polymer network structure and topology greatly affects the mechanical properties of hydrogels. However, the effects of different network topologies on hydrogel adhesion has been less explored. In particular, in the second part of the thesis, we explored using surface dangling chains to create interfacial polymer entanglement termed "slip linkage". This approach based on the concept of slip linkages allows for precise tuning of the adhesion energy across a wide range, spanning from approximately 10 Jm^{-2} to 1000 Jm^{-2} by varying loading rates (Fig 4.4). It is plausible that the slip linkage mechanism can lead to extremely low adhesion energy at ultra-low loading rates, where chains can easily slip out due to thermal energy, potentially resulting in remarkably high values of SR. Therefore, the two approaches together allow for the achievement of high SR that spans a diverse range of initial adhesion energy values (G_c) (Fig 5.2), offering the potential to finely tune and control hydrogel adhesion properties in a versatile manner without the need for chemical reactions, thereby mitigating the associated complications such as poor biocompatibility.

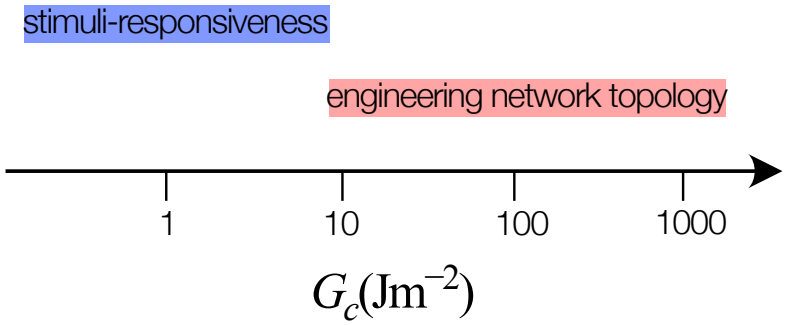

Fig. 5.2: The effective range of G_c to achieve high adhesion switch ratio for strategies of the stimuli-responsiveness and engineering polymer network topology

5.2 Biodegradability and repeatability of hydrogel adhesion

For applications such as bioadhesives, biodegradability is an important aspect to consider. In both works presented in chapters 3 and 4, the polymer networks can be biodegraded by

using degradable crosslinkers. The available degradable crosslinkers include PEGDA and PoloxDA, which can be degraded by hydrolysis, as well as those which can be degraded by enzymes, such as GelMa [4]. These degradable crosslinkers can be integrated into the PAAm and PNIPAm networks to enable biodegradability.

In terms of the repeatability of hydrogel adhesion, both works discussed in this thesis have the potential to demonstrate repeatable adhesion enabled by re-applying bridging polymers to interfaces. The newly applied bridging polymer can diffuse into the hydrogel adhesive and the adherend to form polymer entanglement once again. As a proof of concept, in the second work discussed in Chapter 4, we repeatedly peel off and re-attach a TEA gel on a regular gel, and the adhesion reaches a plateau after 5 cycles (Fig. 4.S5d).

5.3 Loading rate to release hydrogel adhesives

In chapter 4, loading rate is used as an important parameter to tune adhesion energy. For bioadhesive applications, commonly used loading rates may vary from case to case, although some studies adopted crack speed around 1 mm/s [5], and the ASTM F2256 suggests a crack speed around 2 mm/s. Nevertheless, our TEA adhesive presented in chapter 4 provides an effective approach to minimize the potential damage to tissue wounds upon removal of adhesive, due to the weak adhesion provided by the slip-linkage at relatively low loading rates (around 0.1 mm/s).

5.4 future work

Several suggestions are proposed to provide direction for future research endeavors.

1. There is significant potential for exploring various stimuli-responsive hydrogels and other actuating materials to achieve controlled adhesion behaviors. For instance, incorporating light-sensitive hydrogels or utilizing materials like liquid crystal elastomers could provide new dimensions for achieving desired adhesion properties. Moreover, the current analytical model could be extended to encompass the study of intrinsic energy release rates generated by other actuating materials, particularly those with anisotropic volume shrinkage such as liquid crystal elastomers. By expanding the model, we would be able to predict and analyze the adhesion dynamics of a wider range of materials, potentially enabling the development of more versatile and tailored adhesion strategies for different applications.

2. Secondly, there is an avenue to explore various manufacturing methods to develop hydrogel adhesives with meticulously controlled dangling chain layer sizes. One promising strategy involves employing gelling molds with varying surface energies to facilitate the polymerization of TEA gels. This approach allows for the independent variation of the dangling chain layer's size, decoupling it from the bulk properties of the hydrogel. This separation enables the orthogonal programming of adhesion energy and kinetics.

3. Finally, the concept of topology-engineered hydrogel adhesive can be integrated with a stimuli-responsive hydrogel matrix. Through the contraction of the hydrogel matrix, an intrinsic energy release rate (G) would counteract the adhesion energy driven by slip linkages, which exhibit rate-dependence. Consequently, the rate at which the matrix contracts would likely influence the adhesion energy and, by extension, the bonding state of the hydrogel adhesive. This rate of hydrogel contraction is anticipated to be influenced by factors such as hydrogel dimensions, polymer mesh size, and the interplay between the solvent and polymer network. This wide-ranging design space opens up numerous possibilities for manipulating the bonding state of hydrogel adhesives.

Bibliography

[1] John L Kelley. *General topology*. Courier Dover Publications, 2017.

[2] Yuwei Gu, Julia Zhao, and Jeremiah A Johnson. A (macro) molecular-level understanding of polymer network topology. *Trends in Chemistry*, 1(3):318–334, 2019.

[3] Chenghai Li, Zhijian Wang, Yang Wang, Qiguang He, Rong Long, and Shengqiang Cai. Effects of network structures on the fracture of hydrogel. *Extreme Mechanics Letters*, 49:101495, 2021.

[4] Benjamin R Freedman, Oktay Uzun, Nadja M Maldonado Luna, Anna Rock, Charles Clifford, Emily Stoler, Gabrielle Östlund-Sholars, Christopher Johnson, and David J Mooney. Degradable and removable tough adhesive hydrogels. *Advanced Materials*, 33(17):2008553, 2021.

[5] Joana Caldeira, Adam Celiz, and Nicolas Newell. A biomechanical testing method to assess tissue adhesives for annulus closure. *Journal of the Mechanical Behavior of Biomedical Materials*, 129:105150, 2022.

Chapter 6

Concluding remarks

Controlling hydrogel adhesion across multiple facets presents challenges stemming from factors like extreme softness, a wet environment, and the need to interface with irregular, curved, and unpredictable substrates, as elaborated in section 2.1. Contemporary methods to modulate hydrogel adhesion energy frequently rely on the diffusion and reaction of chemicals, which can give rise to issues surrounding precision and biocompatibility. Recent efforts to regulate hydrogel adhesion have employed solutions involving mesh structures that define solution thickness at the interface. However, this approach may not be practically viable in various applications. The creation of spatially controlled, heterogeneous adhesion often necessitates the use of masking materials at the interface. Yet, selective masking is constrained to generating flat patterns, and its execution might involve the placement of rigid polymer film-based masking materials. This could complicate matters due to mechanical mismatch, undesired adhesion at the adhesive-substrate interface, and the potential for residual stress/strain or strain when substrates undergo extensive deformation, such as stretching.

To address the aforementioned problems, this thesis delves into methodologies aimed at governing hydrogel adhesion, with a distinct focus on the utilization of the mechanics of bulk contraction and the physics of interfacial polymer entanglement of hydrogel adhesives, and obviating the reliance on chemical interventions and the ensuing complexities they involve.

In the first approach, we harness the potential of a stimuli-responsive hydrogel adhesive to manipulate the adhesive bond. This is achieved through the active contraction of the hydrogel upon stimulation, which generates an intrinsic energy release rate to promote interfacial delamination. Concurrently, the augmented bulk mechanics during shrinkage serve to elevate adhesion energy. These two factors engage in a intriguing interplay to determine the adhesive bond status. Notably, by employing a single stimulus source, namely temperature, and

varying initial adhesion energies, we demonstrate the capacity to induce a broad spectrum of post-stimulation adhesion energies. This spans from a significant reduction in adhesion (with a switch ratio of 100) to an enhancement of adhesion (with a switch ratio of 2). (In responding to objective 1 in section 1.4.)

In the second approach, we focus on engineering the surface polymer network topology of a hydrogel by creating a dangling chain layer with controlled thicknesses. The dangling chain layer with varying thickness lead to different interfacial polymer entanglements known as stitch and slip linkages. These linkages exhibit distinct adhesion behaviors. Specifically, adhesion energy in the case of the slip linkage is significantly rate-dependent, while the adhesion kinetics are influenced by the governing length of the linkage. We rationalize the rate-dependent adhesion as a consequence of thermally-activated bond slippage, and attribute the control over adhesion kinetics to polymer chain diffusion. The understanding enables the development of hydrogel adhesives with predictive adhesion energy, kinetics, and high-fidelity spatial distribution. (In responding to objective 2 in section 1.4.)

With the knowledge gained in the second approach, we fabricate soft devices of novel functionalities, including selective wound patches, reconfigurable soft robotics, and fluidic channels on diverse surfaces. For example, the selective would can form heterogeneous adhesion to substrates such as tissues without the need for interfacial masking materials; the re-configurable robotics can actuate under modest frequency, while being effortlessly disassembled with little force at low frequency, followed by reconfiguration. (In responding to objective 3 in section 1.4.)

In summary, this thesis introduces innovative methods to manipulate hydrogel adhesion without relying on chemical reactions or external apparatus such as light or ultrasound. These approaches offer promising prospects for diverse fields, including biomedical engineering and human-machine interfaces, among others.

Chapter 7

Original contribution to knowledge

This thesis has the following original contribution to knowledge.

1. Established understanding on how the bulk contraction of hydrogels affects their adhesion energy, through combined experimental, analytical, and computational approaches.

2. Established experimental methods to characterize the stimuli-responsive behavior of alginate/PNIPAm hydrogel, and implemented it in the finite element model to study the bulk contraction-interface delamination coupling.

3. Discovered for the first time that the stimuli-responsiveness can serve as either adhesion switch or adhesion toughener, depending on the value of the initial adhesion energy.

4. Gained understanding between hydrogel adhesion and topology of interfacial polymer entanglement. Specifically, the hydrogels with surface dangling chains form slip linkages at the interface, which results in highly rate-dependent adhesion based on the thermally-activated bond breaking.

5. Discovered that the adhesion kinetics of hydrogel with surface dangling chains depends on the size of the dangling chain layer. The understanding can be exploited to fabricate hydrogel adhesives with programmable adhesion kinetics.

6. Fabricated hydrogel adhesives with spatially-distributed heterogeneous adhesion energy. Such heterogeneous adhesion is directly encoded in the hydrogel adhesives, eliminating the need for applying masking materials to the interface.

Appendix

Additional information regarding the derivation of the intrinsic energy release rate induced by contraction.

Here we provide the definition of numerous variables used in deriving the energy release rate in the interface crack subject to general loadings (Eqn. 2.14), adapted from Suo et al. [1]. The following parameters are expressed in terms of the geometrical parameters shown in Fig 2.7.

$$\begin{aligned}
\eta &= \frac{h_1}{h_2} \\
\Delta &= \frac{\delta}{h_1} \\
\Sigma &= \frac{1+\alpha}{1-\alpha} \\
A_0 &= \frac{1}{\eta} + \Sigma \\
I_0 &= \frac{1}{3}\left[\Sigma\left[3\left(\Delta - \frac{1}{\eta}\right)^2 - 3\left(\Delta - \frac{1}{\eta}\right) + 1\right] + 3\frac{\Delta}{\eta}\left(\Delta - \frac{1}{\eta}\right) + \frac{1}{\eta^3}\right]
\end{aligned} \tag{1}$$

The C variables in Eqn. 2.13 are expressed as follows:

$$\begin{aligned}
C_1 &= \frac{\Sigma}{A_0} \\
C_2 &= \frac{\Sigma}{I_0}\left[\frac{1}{\eta} - \Delta + \frac{1}{2}\right] \\
C_3 &= \frac{\Sigma}{12 I_0}
\end{aligned} \tag{2}$$

Additional information regarding the modified lap-shear test to measure post-stimulation adhesion energy of alginate/PNIPAm hydrogels.

For the modified lap-shear test, the sample was directly clamped onto a universal testing machine (model 5965; Instron, Norwood, MA, USA). The cross-head of the Instron apparatus was set to move at a controlled displacement rate. Throughout the test, both force and displacement data were recorded, with the resulting adhesion energy computed using Equation

2.9. Before the adhesion measurements, a polyethylene terephthalate (PET) film was affixed to the rear side of the hydrogel to confine its deformation. The testing time frame was short to ensure that the samples retained relatively elevated temperatures during adhesion energy measurement.

Utilizing the lap-shear test, we measured the initial adhesion energies before stimulation for these topohesive formulations to be G_c = 1.18, 3.54, 8.84, 20.63 Jm^{-2} at chitosan concentrations of 0%, 0.5%, 1%, and 2% w/v, respectively. Subsequently, following a storage period of 3 hours at 37°C, the samples prepared using the same topohesive compositions also underwent lap-shear tests. The data are recorded in Fig 5.1.

Bibliography

[1] Zhigang Suo and John W Hutchinson. Interface crack between two elastic layers. *International Journal of Fracture*, 43(1):1–18, 1990.